UNIVERSITÀ DEGLI STUDI DI MILANO

Facoltà di Scienze e Tecnologie

Corso di dottorato in CHIMICA

XXXI ciclo

On the investigation of nucleation, growth, structure and morphology of functional materials through advanced crystallographic techniques

Tutor: Prof. Silvia Rizzato

Co-tutor: Prof. Massimo Moret

Co-tutor: Dr. Leonardo Lo Presti

Tesi di dottorato di:
Fabio BEGHI
Matr. R11411

Anno Accademico 2017 – 2018

Table of contents

I-Use of gel technique for the crystallization of coordination polymers

Coordination polymers

Coordination polymers can be considered as crystalline hybrid organic-inorganic systems with potential applications in many fields of nanotechnology and material chemistry. Their potential application range from gas storage and separation to catalysis, molecular sensing, ion-exchange and drug delivery [1,2]. They are usually built by self-assembly of metal centres and organic bridging connectors to give networks with different dimensionality and topology (Fig1.1). X-ray diffraction is the principal tool for the investigation of these systems.

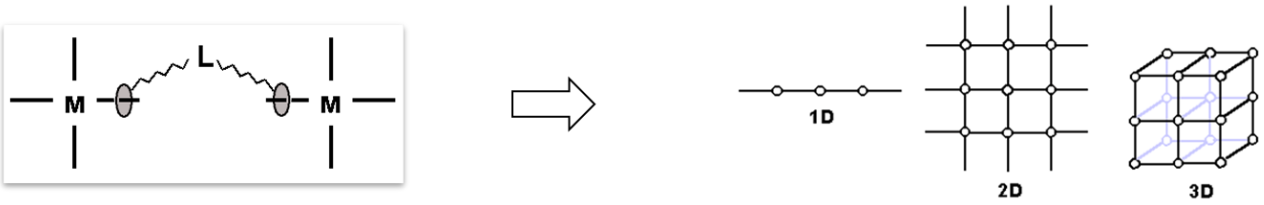

Fig1.1 Formation of n-dimensional network lining metal centres with organic ligands

The processes of self- assembly of coordination polymers are complex and they determine the topology and dimensionality of the obtained material.

Actually, full and efficient control over the total design of a network structure cannot be achieved yet. An effective synthetic strategy based on a rational choice of the nature of metal centres and donor atoms, the length and geometry of bridging groups, the size and shape of counterions, etc. has been shown to work well [3]. Nevertheless, significant challenges remain in order to obtain a complete understanding of the subtle driving factors operative during the self-assembly of these polymeric materials. As a consequence, in many cases, several polymeric species with different L/M (ligand to metal) stoichiometries, dimensionalities, topologies and porosities can be obtained under slightly different reaction conditions starting from the same ligand–metal salt pair [4].

In what concerns coordination polymers, the solution behaviour of ligand molecules and metallic centres play a crucial role during the growing process.

Apart from the problematic connected with the self-assembly process; coordination polymers often have high structural complexity and are often porous. Both these aspects result in several issues regarding their crystallization. They can be not tough enough for a complete physical characterization, including the determination of the crystal structure. This is especially true for network systems characterized by a high flexibility.

Beyond the stabilization problems of the samples, an increasing attention has been devoted to the control of the size and the morphology of the crystals at both nano and macro scales, this is because the habit of the crystals, but also their microscopic structure, can have a strong influence on many properties and functions of the crystalline materials.

Crystallization adopting counterdiffusion inside gel media

A gel is a system where a liquid phase is dispersed within a solid phase. A network of micrometric channels and pores filled by solution characterizes the obtained material. Any mass transport mechanism but gradient-driven diffusion is avoided. This creates an interesting media to perform crystal nucleation and growth under purely diffusive conditions.

Recently gel technique for crystallization has been extensively adopted, leading to intriguing results about crystals quality, dimension, mechanical and chemical stability [10,11].

An important aspect related with the use of hydrogels is the incorporation of gel matrix fibres in the structure of the crystals, as was shown for calcite [10]. Organic matrix incorporated inside the crystal create a network of nanofibers, while the crystal itself is better described as an ensemble of same-oriented crystallites [12,13]. These phenomena are well known and investigated in biogenic crystals, where lipids, membrane and proteins can move the crystallization towards highly specific morphologies.
Gel media has also revealed the ability for certain organic molecule to induce the formation of new phases and polymorphs [14–16].
Gel technique application is based on the classical counterdiffusion crystallization experiment (Fig1.2). Gelled solution inside test tubes can be layered using anti-solvents, precipitating agents or reagents solutions, depending on the crystallization process of interest. This kind of experiment let the layered and gelled solution to have a common interphase where precipitation can immediately occur, and is called free intherphase diffusion (FID). A little modification can be introduced by layering over the gelled solution a gelled solvent, avoiding the direct contact between the involved solutions (three layer method, TLD). Gel media can be used also to fill the horizontal branch of an U-shaped tube, then layered on the two branches with the desired couple of solution (target molecule-precipitating agents or solutions of different reagents).

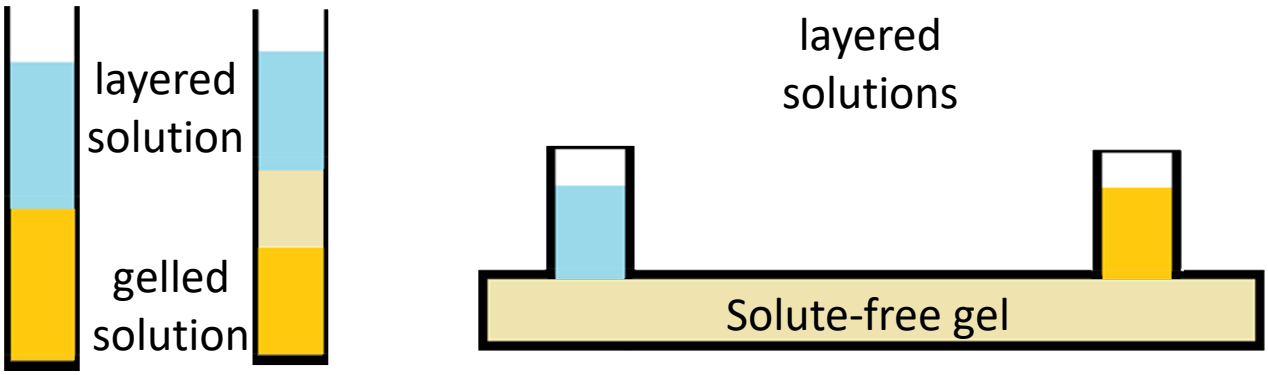

Fig1.2 Experimental set-ups to perform counterdiffusion experiments adopting gelled solutions

Aim of the work

Let's consider a U-shaped tube filled by gelled solvent, layered by the solutions of a ligand molecule L and a metal salt MX on the opposite side. As said before, the two reagents slowly diffuse in the horizontal branch of the tube. Due to the slow diffusion the concentration of the reagents varies constantly along the horizontal branch (Fig1.3).
The effect of this diffusion is that, inside gel media, slightly different crystallization conditions can be simultaneously created. Ligand-metal reaction can produce coordination compound networks. As previously introduced, little difference in the crystallization environment can lead the synthesis towards the formation of network completely different from the point of view of dimensionality, topology, coordination geometry of metal centers and ligand behaviors.

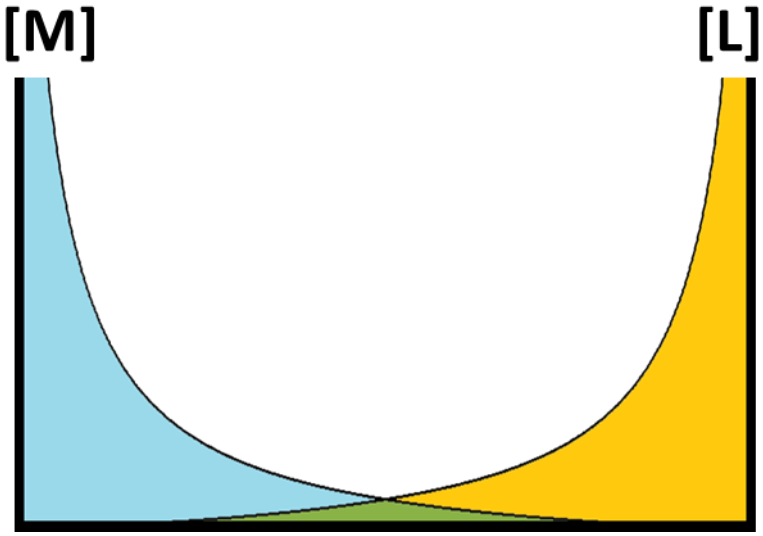

Fig 1.3. Effects in terms of concentration of slow reagents diffusion along a U-shaped tube

We developed and used the gel technique as a general method to crystallize coordination polymer systems, but also to study and achieve a better control on their crystallogenesis process as well as to induce morphological and structural modifications.

Once, (Chapter 2) we extensively mapped the phase diagram of a well know M/L couple (Cd(II) and *bpp*) in solution and in gel media, focusing on the differences in phase diagram caused by gel presence. We also studied the kinetics of the crystal growth inside gel in order to verify the diffusive propertied of the gel media. We tested the ability of gel media to shed light on the crystallization process. Secondly, (chapter 3) we moved towards the study of a common M/L couple (Cu(II)/Hiso). The purpose is to verify the availability of gel media with other classical crystallization method for the identification of new networks. Finally, we studied the effect of gel media on crystalline habit (Chapter 4). At last (Chapter 5) the importance of the crystallization process is studied in a pathologic case: the formation of cholesterol phase inside 2D lipid bilayers.

Bibliography

1. Dey, C., Kundu, T., Biswal, B. P., Mallick, A. & Banerjee, R. Crystalline metal-Organic frameworks (MOFs): Synthesis, structure and function. *Acta Crystallogr. Sect. B Struct. Sci. Cryst. Eng. Mater.* **70,** 3–10 (2014).
2. Stock, N. & Biswas, S. Synthesis of metal-organic frameworks (MOFs): Routes to various MOF topologies, morphologies, and composites. *Chem. Rev.* **112,** 933–969 (2012).
3. Cai, Y., Kulkarni, A. R., Huang, Y. G., Sholl, D. S. & Walton, K. S. Control of metal-organic framework crystal topology by ligand functionalization: Functionalized HKUST-1 derivatives. *Cryst. Growth Des.* **14,** 6122–6128 (2014).
4. James, S. L. Metal-organic frameworks. *Chem. Soc. Rev.* **32,** 276 (2003).
5. Chun, H. & Bernal, I. Polymorphism in the Crystallization Behavior of Trinitrocobalt(III) Complexes with Tridentate Amine Ligands: Hydrogen-Bonding Analysis and Syntheses of Racemic and Conglomerate mer-Co(dpt)(NO2)3. *Cryst. Growth Des.* **1,** 67–72 (2001).
6. Szelagowska-Kunstman, K. *et al.* Surface structure of metal-organic framework grown on self-assembled monolayers revealed by high-resolution atomic force microscopy. *J. Am. Chem. Soc.* **130,** 14446–14447 (2008).
7. Moret, M. & Rizzato, S. Crystallization Behavior of Coordination Polymers. 2. Surface Micro-Morphology and Growth Mechanisms of {[}Cu(bpp)(3)Cl-2]center dot 2H(2)O by in Situ Atomic Force Microscopy. *Cryst. Growth Des.* **9,** 5035–5042 (2009).
8. Carlucci, L., Ciani, G., Moret, M., Proserpio, D. M. & Rizzato, S. Monitoring the Crystal Growth and Interconversion of New Coordination Networks in the Self-assembly of MCl 2 Salts (M = Co, Ni, Cu, Cd) and 1,3-Bis(4-pyridyl)propane. *Chem. Mater.* **14,** 12–16 (2002).
9. Carlucci, L. *et al.* Crystallization behavior of coordination polymers. 1. kinetic and thermodynamic features of 1,3-Bis(4-pyridyl)propane/MCl2 Systems. *Cryst. Growth Des.* **9,** 5024–5034 (2009).
10. Li, H. & Estroff, L. A. Calcite growth in hydrogels: Assessing the mechanism of polymer-network incorporation into single crystals. *Adv. Mater.* **21,** 470–473 (2009).
11. Estroff, L. A. & Hamilton, A. D. At the interface of organic and inorganic chemistry: Bioinspired synthesis of composite materials. *Chem. Mater.* **13,** 3227–3235 (2001).
12. Otálora, F., Novella, M. L., Gavira, J. A., Thomas, B. R. & Ruiz, J. M. G. Experimental evidence for the stability of the depletion zone around a growing protein crystal under microgravity. *Acta Crystallogr. Sect. D Biol. Crystallogr.* **57,** 412–417 (2001).
13. Grassmann, O., Neder, R. B., Putnis, A. & Löbmann, P. Biomimetic control of crystal assembly by growth in an organic hydrogel network. *Am. Mineral.* **88,** 647–652 (2003).
14. Petrova, R. I. & Swift, J. A. Habit Changes of Sodium Bromate Crystals Grown from Gel Media. *Cryst. Growth Des.* **2,** 573–578 (2002).
15. Diao, Y. *et al.* Gel-induced selective crystallization of polymorphs. *J. Am. Chem. Soc.* **134,** 673–684 (2012).
16. Mahieux, J., Sanselme, M. & Coquerel, G. Access to single crystals of (±)-form IV of modafinil by crystallization in gels. Comparisons between (±)-forms I, III, and IV and (-)-form i. *Cryst. Growth Des.* **13,** 908–917 (2013).

II-System Cd(II)/ bis-pyridil-propane

Bis-pyridil-propane (*bpp*) is a common and widely used ligand for the formation of coordination polymers networks. *Bpp* is a flexible ligand that can bind metal cations through two pyridil nitrogen. The ligand in flexible and bidentate. It can bind a single cation using one or both the nitrogen or act as a flexible connector joining two metal centres.

Cd (II) is a large cation able to connect the *bpp* ligand through Cd-N bonds. The phases that can be obtained from the combination of Cd(II) and *bpp* using water or a 1:1 mixture of water and ethanol as solvents were identified in previous works [1,2]. Such phases are summarized in the following table (Tab.2.1). In all the phases the Cd(II) cation assumes an octahedral coordination geometry, with two position occupied by chlorine atoms. This is interesting because let the networks to have no net charge so, during its formation, the presence of an appropriate counter anion doesn't play a crucial role. All the phases are characterized by a different dimensionality or topology of the metal-ligand network, and this is partially reflected in their composition. In particular, we report for any phase the ratio of ligand molecules per metal cations in the formula unit (L/M).

Phase $[Cd(bpp)_3Cl_2]\cdot H_2O$ (1D-Cd) is an 1D polymer and was obtained by direct mixing of the reagents in water solution. Phase $[Cd(bpp)_2Cl_2]\cdot H_2O$ (3D-*dia*) is an 3D polymer formed by interpenetrated diamantoid networks. It was obtained in a similar way, using a 1:1 water/ethanol solution. Phase $[Cd_2(bpp)_3Cl_2]\cdot H_2O$ (3D-*sra*) Is a 3D polymer formed by the interpenetration of two network showing an unusual *sra* topology. This phase was firstly obtained with a hydrothermal reaction catalysed by ammonium formate [2], but was later precipitated from water/ethanolic solutions at room temperature, using an excess of metal salts ([L]/[M] < 1) [3].

phase	**1D-Cd**[1] (A)	**3D-*dia***[1] (B)	**3D-*sra***[2] (C)
Formula unit	$[Cd(bpp)_3Cl_2]\cdot H_2O$	$[Cd(bpp)_2Cl_2]\cdot H_2O$	$[Cd_2(bpp)_3Cl_2]\cdot H_2O$
L/M	3	2	1.5
a (Å)	16.516	17.536	9.3593
b (Å)	26.779	17.536	11.904
c (Å)	17.705	42.966	18.237
V ($Å^3$)	7830	13212	2004
α	90°	90°	93,18
β	90°	90°	98,53
γ	90°	90°	91,98
Z'	0.5	1	1
Z	8	16	2
space group	Ibca	$I4_1/a$	$P\bar{1}$
habit	hexagonal platelet	bypiramid	needle/elongated platelet

Table 2.1. Phases precipitated from water or 1:1 water/ethanol solutions of $CdCl_2$ and bpp.

The crystalline habits of the phases are markedly different (Fig.2.1). This aspect is useful because simplifies the recognition of the different phases, that can be recognized by optical microscopy inspection of their crystals habits.

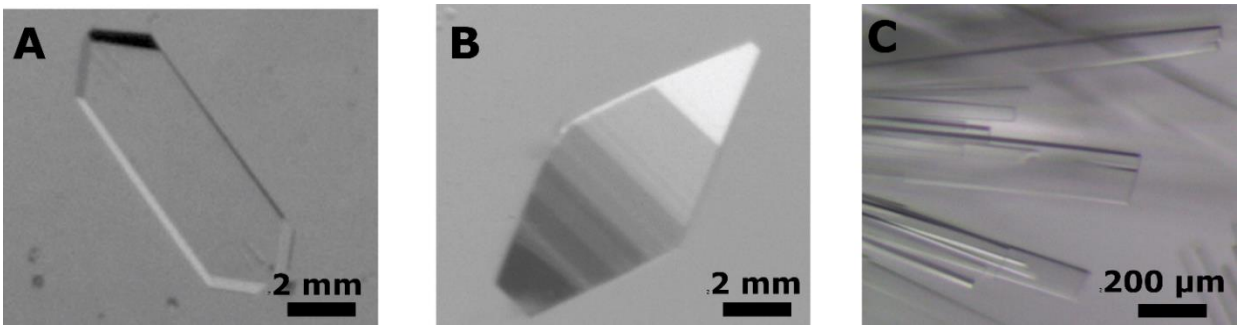

Figure 2.1. Crystal habits of the phases precipitated from water or 1:1 water/ethanol solutions of $CdCl_2$ and bpp. 1D-Cd (A); 3D-dia) (B);3D-sra (C).

The aforementioned synthesis of phase 3D-sra by direct mixing of the reagents at room temperature is interesting. This evidence suggests us that all the phases can be isolated by careful design of the precipitating conditions, as we previously proposed (chapter 1). For this reason, we deeply study the phase diagram of the system and the crystallization process that can be induced.

We considered water solutions and water/EtOH solutions (using different amounts of EtOH in the composition) of $CdCl_2 \cdot 5/2H_2O$ (M) and *bpp* (L). We focused on three main parameters: the solvent composition (in terms of %EtOH), the reagent ratio ([L]/[M]) and the overall concentration of the solution ([L]+[M]).

At first we studied the system behaviour in solution using batch technique. This technique let us to observe the system behaviour at numerous slightly different precipitation conditions. Then we also consider the application of counterdiffusion techniques using solutions gelled with agarose. These methods introduce two other parameters: the geometrical configuration of the experiments and the density of the gel. We considered two experimental set-ups: counterdiffusion inside test tube and counterdiffusion inside U-shaped tube. We considered as agarose densities 0.1% w/v; 0.5% w/v; 1% w/v and 3% w/v. The obtained phases, their amounts, their positions inside the tubes and the morphologies of their crystals are all crucial experimental outputs considered.

In order to shed more light on the crystallization process we also studied its kinetics, considering exclusively phase 1D-Cd.

Experimental methods

Batch technique

Precipitation experiment from solution were performed inside 24-well PPE plates. Every well was filled with the same volume of solution (2mL). Two experiments were performed. At first, we studied the importance of reagent ratio (L/M) and total concentration at a fixed solvent composition (50% EtOH). Then we studied the importance of solvent composition at a fixed total concentration (20mM) varying exclusively the reagents ratio.

For the first experiment, we prepared 25 mL of a water solution 60 mM of $CdCl_2 \cdot 7/2H_2O$ (342.9mg, 1.50 mmol) and 25 mL of a ethanolic solution 101 mM of *bpp* (501.2 mg, 2.53 mmol). Wells were filled with the following order: metal salt solution, ethanol (if needed), water (if needed) and ligand solution. Pure solvents were added in order to dilute the reagents and to keep solvent composition constant (50% v/v EtOH). We consider overall concentration of the reagents from 10 mM to 60 mM (10, 20, 30, 40, 50, 60 mM) and reagent ratio ([L]/[M]) from 1 to 4 (1, 1.5, 2, 2.5, 3, 3.5, 4) (Supporting information, Tab.S.2.1 and 3).

Wells were sealed and closed, temperature was kept at 25°C using a water bath, the wells were left undisturbed for three months. The same day they were opened and photographed to recognized the precipitated phases.
For the second experiment, we prepared 20 mL of a water solution 41 mM of $CdCl_2 \cdot 7/2H_2O$ (186.9mg, 0.82 mmol) and 20 mL of a EtOH solution 40 mM of *bpp* (158.3 mg, 0.80 mmol). Wells were filled following the order: metal salt solution, ethanol (if necessary), water (if necessary) and ligand solution. Solvents were added in order to dilute the reagents and constantly vary the solvent composition (0%, 10%, 20%, 30%, 40%, 50% v/v EtOH). Reagent ratio was varied from 1 to 4 (1, 2, 3, 4). (Supporting information, Tab.S.2.2 and 4)
Wells were sealed and closed. They were kept at constant temperature (25°C) and left undisturbed for three months. The same day they were opened and photographed to recognized the precipitated phases. Inside some wells was observed precipitation of powder, that were analysed using X-Ray Powder Diffraction (XRPD) (Supporting information Fig.S.2.1,2,3).

Counterdiffusion experiments adopting gelled solution

Agarose gel

We used Agarose to obtain gelled solutions. Agarose is a polysaccharide extracted from sea wed, formed by long chains of agarobiose. Its melting point is about 96°C. It is insoluble in water solutions, but the molten phase can mix with water. The gel is prepared heating a water solution of the polysaccharide above agarose melting point. After cooling, the long chains entangle and create a microscopic structure of channels and pores filled with the water solution. The resulting material is a soft gel. Through the pores, solutes can move by concentration – driven diffusion. The network of channels is responsible for the motion of the solvent and the solutes.
The “strength” of the gel, that macroscopically is its stiffness, is determined by the dimension and the density of the pores and channels. High concentration of agarose in terms of weight of agarose respect to the volume of the solution is related with narrower pores and a stiffer material. This has strong effect on the diffusive properties of the material.
We used two common concentrations of agarose, extensively used for electrophoresis (1% w/v and 0.5% w/v) and two ‘’extreme’’ concentrations: very soft (0.1% w/v) and very hard (3% w/v).

Counterdiffusion inside test tube

Counterdiffusion inside test tube is based on the layering of a solution over a previously placed different solution. Different solvents, solvents compositions or solute can differentiate the two solutions. In classical counterdiffusion experiments, adopting exclusively solutions, their density determines their position.
Using gelled solutions, the gelled solution always is at the bottom of the tube. After gel setting, in our case after agarose cooling, the second solution is poured over the gel. This kind of experiment is called a Free Interphase Deposition (FID), meaning that the two solutions are directly exposed one to each other, without the presence of a solute-free spacer of any kind. In this way reaction or precipitation can occur at the sol/gel interphase.
Detailed parameter for the preparation of all the tubes are reported in the supporting information, Tab.S.2.5,6,7,8,9. We consider all the aforementioned gel concentrations. Inside test tube we firstly used gelled water solution of the metal salt or of the ligand, layered with the ethanolic solution of the complementary reagent. Setting time can last some seconds (3% w/v agarose) or a couple of hours (0,1% w/v), depending on agarose concentration.

We also inverted the position of the reagents, layering ethanolic solutions of the metal salt over water gelled solutions of the ligand (supporting information, Tab.S.2.10,11)
Layered tubes were closed and sealed, then left undisturbed for three-four months. Temperature was kept constant (25° C) using a water bath. Tubes were photographed without opening.

Counterdiffusion inside test tube

Using a U-shaped tube, the counterdiffusion experiment is performed in completely different conditions. The horizontal branch is filled with gelled solvent, creating a purely diffusive solute-free environment. After gel setting concentrated solutions of the reagents are poured to fill the vertical branches. These experiments lasted for several months until no evolution in terms of quantity, position and nature of the crystals was observed.
Detailed parameter for the preparation of all the tubes are reported in the supporting information, Tab.S.2.12,13. Also in this case we consider different gel concentrations. In this case we gelled water/ethanol solutions. 40%EtOH v/v is the highest ethanol amount that we can reach in order to avoid phase separation during the setting of the gel. At first we layered increasing concentrations of the reagents in order to find a threshold over which observable crystals can form. then we reduced the amount of ethanol (c.a. 40%, 30%, 22% and 15%EtOH) to study the importance of ethanol in the solvent mixture.
Position of the phases, amount of materials precipitated and their morphologies are the most important considered parameters.

Study of the crystallization kinetics using counterdiffusion method

The experiments were performed inside a home-made optical cell consisting of two glass plates separated by a thin U-shaped rubber film. The cell was half-filled with a water ligand solution (20 mM) gelled with agarose. The upper half of the cell was filled with an aqueous solution of $CdCl_2$ 10mM. In this way we performed a FID counterdiffusion experiment.
For this study we used the agarose concentrations previously considered (0,1%, 0,5%, 1%, 3% w/v). The upper edge was closed with adhesive tape; the cell was placed under a stereoscopic microscope equipped with a time-lapse video recorder.

XRPD analysis

Powder X-ray diffraction experiment were performed on a Philips PW 1830 vertical scan diffractometer using CuKα radiation (λ=1.54 Å). For X-ray generation we used a 40 mA current at 40 kV voltage. Patterns were collected for 2θ values from 5° to 35°, using a 0.5° step collected for 20s. collected data are reported in the Supporting Information section (Fig.S.2.1,2,3).

Results and discussion

Determination of the phase diagram

Phase diagram in solution

We determined the phase diagram for the couple $CdCl_2$/*bpp* using as solvent a mixture of equal volumes of ethanol and water. Using this solvent composition is known that phase 1D-Cd does not precipitate. Every batch is different from the point of view of the reagents concentration ([M]+[L]) or molar ratio ([L]/[M]) (Fig.2.2).

Phase 3D-sra usually precipitates as powder. At low overall concentrations ([L]+[M] < 30 mM) it forms thin needles collected in bunches. Phase 3D-dia instead usually forms bipyramidal crystals, only at the higher concentrations (60 mM) precipitates as powder.
The exclusive precipitation phase 3D-sra is related with low values of reagent ratio ([L]/[M] ≤ 1), for higher value phase 3D-dia precipitation becomes more consistent.
The two phases coexist at any observed overall concentration apart from 10mM. Interestingly coexistence is related with the reagent ratio of the solution. At 30 mM concentration, the phases coexist for the largest range, for [L]/[M] values from 1.5 to 4. The range of coexistence shrinks both increasing and decreasing the overall concentration of the reagents.
There is a correlation between the[L]/[M] value of the initial solutions and the L/M value in the formula unit. In fact, 3D-sra phase unit formula has an L/M parameter equal to 1.5, while the same parameter for 3D-dia phase is 2. In ligand-richer solution phase 3D-dia precipitation is strongly favoured.
The overall amount of precipitated material decreases increasing the value of L/M parameter. This suggests us that the solubility of the phases in the selected solvent composition are very different, and 3D-sra is definitively less soluble.

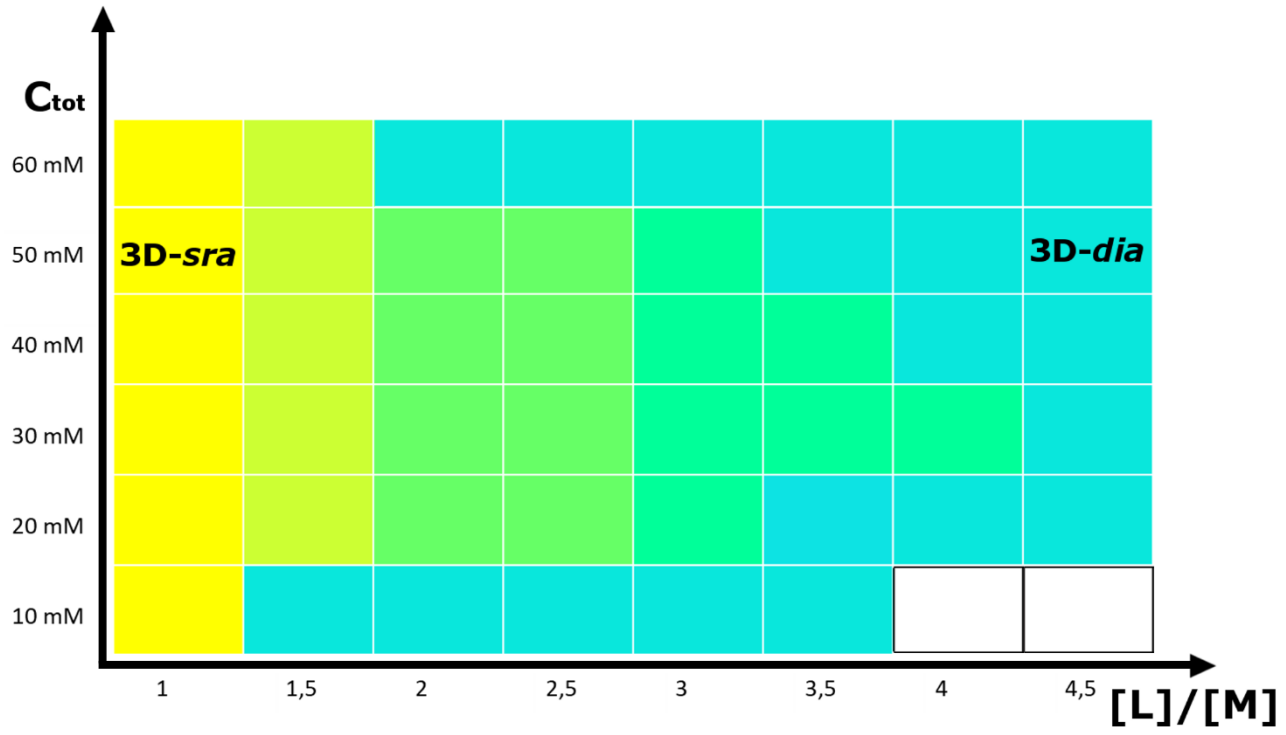

Figure 2.2 Phase diagram for CdCl2/bpp mixture in 1:1 EtOH/water solvent. Every square represent a batch, x-axis reports reagents ratio ([L]/[M]) of the solution, y-axis the overall concentration ([L]+[M]). Colours represent the precipitated phases. Yellow: exclusively 3D-sra phase, light-blue: exclusively 3D-dia phase, green: same amount of the two phases, yellowish green: 3D-sra predominace, blueish green: 3D-dia predomince. Experimental data in supporting information.

Then we studied inside solution the importance of the solvent composition. For this purpose, we choose a single value for the overall concentration ([L]+[M] = 20mM). Inside the batch we varied the

reagent ratio ([L]/[M]) ranging from 1 to 4 and we considered decreasing %EtOH from 50% to 0% (pure water) (Fig2.3).
Phases 1D-Cd and 3D-sra precipitate almost exclusively as powders, revealing to be almost insoluble inside water solvent, and were recognized by XRPD analysis (Fig.S.2.1). Instead phase 3D-dia formed its bipyramidal crystals.
As expected from the previous experiments, high values of ethanol are related with the formation and often the coexistence of phases 3D-sra and 3D-dia. For %EtOH v/v lower than 20%, phase 3D-dia disappears, substituted by phase 1D-Cd. Phase 3D-sra is almost the only observed phase for L/M = 1 at any solvent composition.
Also in this case we observed a correlation between the [L]/[M] value of the solutions and the L/M value in the formula unit. In fact, 1D-Cd phase unit formula has an L/M parameter equal to 3, while the same parameter for 3D-sra phase is 1.5, and in water solution metal-rich solution prepcipitates the metal-rich phase.

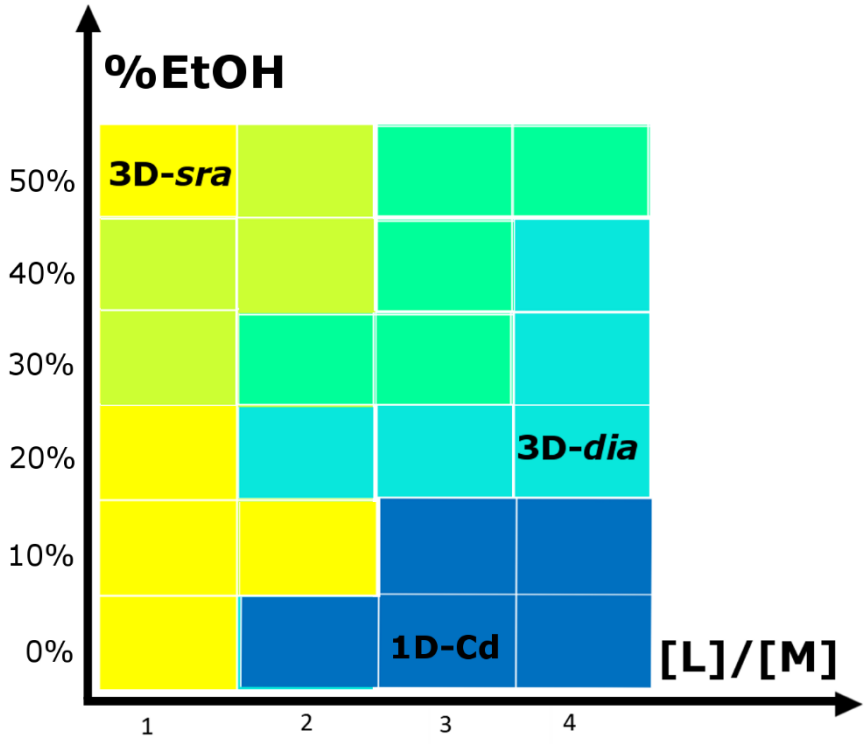

Figure 2.3 Phase diagram for CdCl2/bpp mixture considering different solvent composition. Every square represent a batch, x-axis reports reagents ratio ([L]/[M]) of the solution, y-axis the %EtOH. Colours represent the precipitated phases. Yellow: exclusively 3D-sra phase, light-blue: exclusively 3D-dia phase, yellowish green: 3D-sra predominance, blueish green: 3D-dia predomince. Experimental data in supporting information.

To confirm the results obtained, we also study powders precipitated from solutions at higher concentrations (see Fig.S.2.2). These results confirmed that [L]/[M] value of the solution is crucial to move the precipitation from 3D-dia or 1D-Cd phases to 3D-sra phase, while the amount of ethanol in the solution determines the precipitation of phase 1D-Cd respect to 3D-dia.

Counterdiffusion experiments using test tubes

Counterdiffusion methods using gelled solutions were initially performed inside test tubes. At first, we used test tubes where the gelled solution is a water solution of the metal salt, layered with an equal volume of an ethanol solution of the ligand. Solvents and reagents slowly diffuse inside and outside the gel. However, the reported values for overall concentrations, reagent ratio and solvent composition are referred to a tube where all these quantities are homogenous. In this way, the following obtained phase diagrams can be compared with the diagrams obtained in solution.
We started considering agarose gel 1% w/v, [L]/[M] parameter was varied from 0.5 to 2 (Fig.2.4).

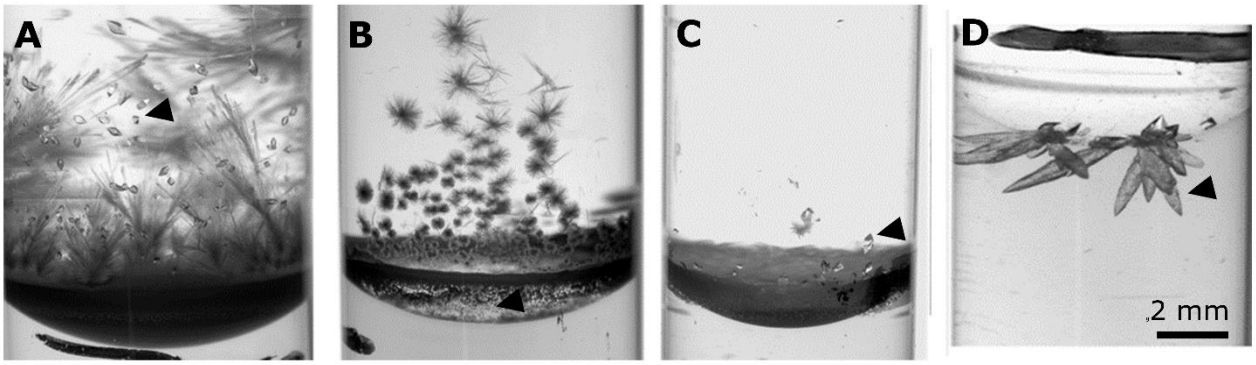

Figure 2.4. test tubes containing ethanolic solution of bpp (L) layered over gelled (1% w/v agarose) water solutions of $CdCl_2$ (M). 2gra82, overall concentration ([L]+[M]) 30.6 mM, reagent ratio ([L]/[M]) 0.5 (A). 2gra85, [L]/[M]=1, [L]+[M]=22,1 (B); 2gra74B [L]/[M]=1,5 [L]+[M]=25,0 (C); 2gra3, [L]/[M]=2,0 [L]+[M]=15,0 (D). Black arrows point 3D-dia phase. For samples compositions see supporting information.

Phase 3D-dia was obtained inside all the tube (black arrows in fig.2.4). At low [L]/[M] value it forms in the solution (Fig.2.4A), but increasing such parameter it forms at the interphase. For high excess of ligand, (Fig.2.4D) 3D-dia phase nucleated at the interphase, then its crystals grew inside the gel assuming an elongated shape. High amounts of phase 3D-sra precipitates at low [L]/[M] value, then this phase disappears from the samples. Adopting this experimental set-up, 3D-dia phase never forms crystals inside the gel media itself.
3D-dia phase was obtained and isolated at lower [L]/[M] values than inside the solutions. This evidence suggests us that the presence of the gel media can affect the phase diagram of the system. For this reason, we mapped the phase diagram of the system respect to the same parameters considered for the solution. In particular, we considered [L]/[M] values ranging from 0.5 to 3, reagents concentrations from 10 to 50 mM and we increased and decreased the gel strength, considering softer (0.1% and 0.5% w/v) and harder (3% w/v) gels. The results are summarized in the following phase diagrams (Fig.2.5)

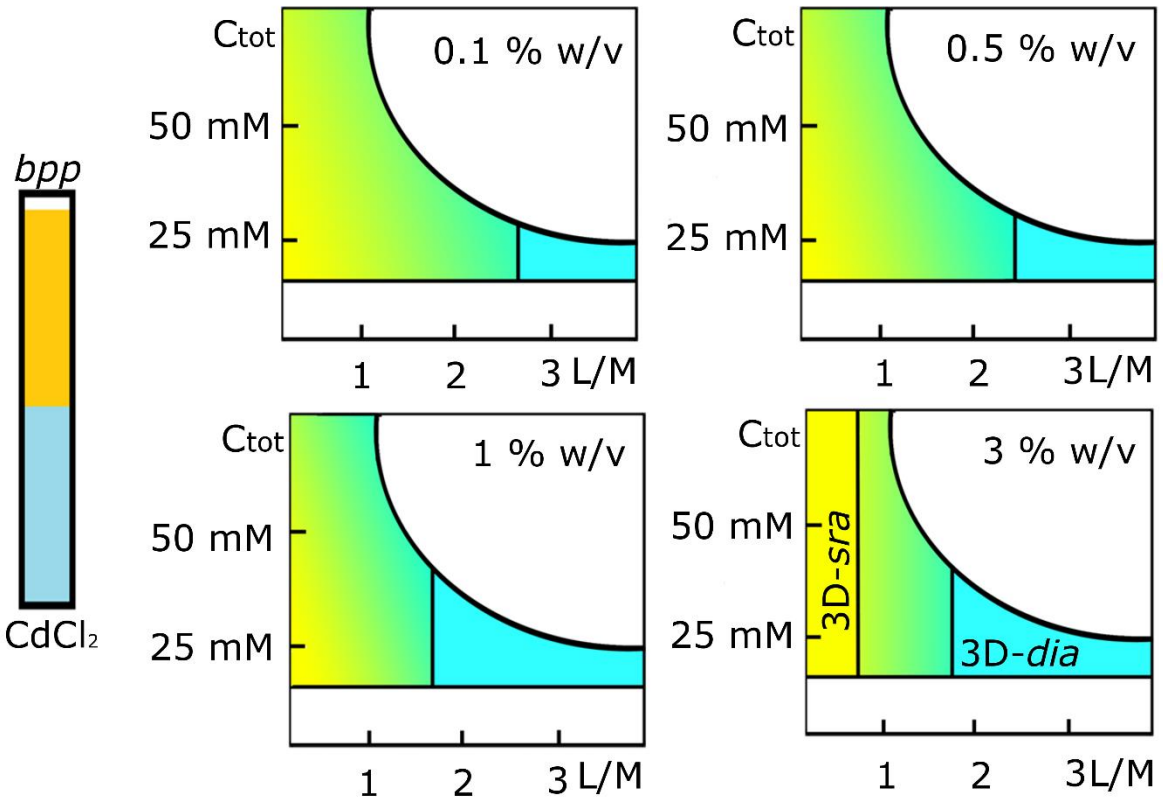

Figure 2.5 Phase diagram for CdCl2/bpp mixture observed in test tubes containing ethanolic solution of bpp (L) layered over gelled water solutions of $CdCl_2$ (M). Different gel concentration are reported over the diagram. On the left is reported a scheme of the sample considered. On x-axis is reported reagents ratio ([L]/[M]), on the y-axis the overall concentration. Colours represent the precipitated phases. Yellow: exclusively 3D-sra phase, light-blue: exclusively 3D-dia phase, yellowish green: 3D-sra predominace, blueish green: 3D-dia predomince. Sample compositions reported in the supporting information.

An overall concentration higher than 10mM is necessary to obtain precipitation of any phase. The formation of phase 3D-dia confirms to be favoured by the presence of agarose gel. For increasing gel concentration, we observed a lowering of the L/M value above which 3D-dia phase is the only precipitated phase. Starting from a 3.5 value in solution it decreases to 3 (0.1% w/v), 2.5 (0.5% w/v) and finally 2 (1% and 3% w/v). The entire phase diagram seems to be shifted along L/M axis, in fact, for the first three considered gel concentration we have not observed a sample were 3D-sra is the only phase precipitated. The only exception is gel 3% w/v where we observed for low L/M values (0.5) the precipitation of exclusively phase 3D-sra.
The range of coexistence, in terms of L/M parameter, does not show any modification respect to the overall concentration of the reagents. This is a strong difference respect to the solution phase diagram. The position of phase 3D-dia crystals moves from the solution to the interphase increasing L/M value, for high value we observed the formation of elongated crystals inside the gel media (Fig.2.6B). In a previous work we observed that these deformed crystals maintained good crystallinity and diffraction properties [4]. 3D-sra instead always forms at the interphase. Its crystals do not grow inside gel media; at least we observed the formation of small spherulites (Fig.2.6D) just below the surface of the gel.

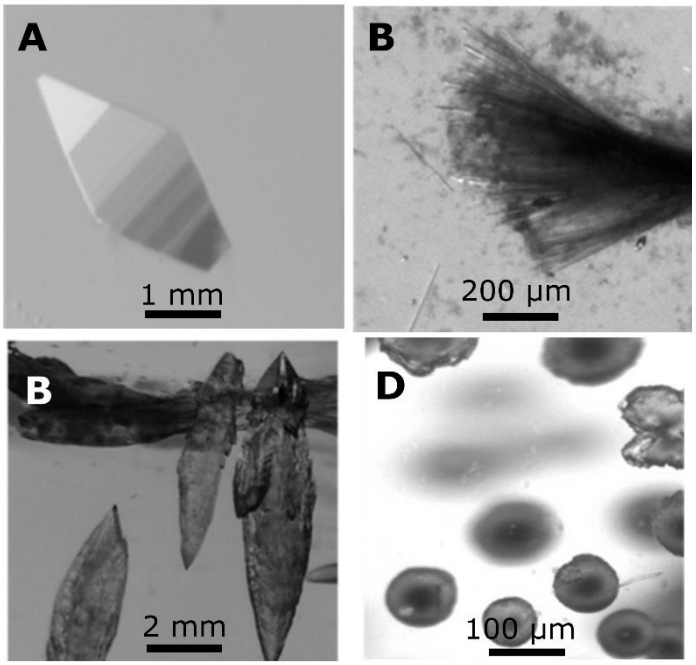

Figure 2.6. 3D-dia crystal grown in solution (A) and inside gel (B). 3D-sra crystals grown in solution (B) 3D-sra spherulites grown inside gel (D).

This experimental output can be justified considering that the diffusion inside gel is much slower than outside gel. In fact, if ligand molecule from the solution cannot diffuse freely inside gel 3D-sra phase cannot form inside metal rich gel media, while the constant diffusion of the metal from the gel can create the conditions for the formation of 3D-dia phase in the ligand-rich ethanol solution.
For this reason, we repeated part of the experiments inverting the positions of the reagents. That is, we gelled a water solution of the ligand ad we poured over it an ethanolic solution of the metal.
We kept constants the overall concentration ([L]+[M] = 20 mM) and gel strength (1% w/v) and we considered reagent ratio from 1 to 4. The experimental output change drammatically (Fig.2.7).
The two phases coexist in all the samples. They are segregated: 3D-sra phase forms in the solution, where it precipitates as powder along the tubes wall; 3D-dia phase forms inside the gel media, from the interphase to the bottom of the tube. The gel strongly affects 3D-dia crystals morphology. crystals formed largely elongated and distorted structures inside the gel.
This result suggests us that the overall picture is more complex. Probably the diffusion rate inside gel is very different for the two reagents. The formation of 3D-dia phase at the bottom of the tube implies that metal ions were able to reach the bottom of the tube, showing a higher mobility respect to ligand molecules. However, the formation of 3D-sra phase powder implies that also ligand molecules can freely diffuse from the gel in the solution.
An important fact has to be considered. Gelled solution and layered solution are based on different solvents (water and ethanol) and this fact surely effects on one side the diffusion process, on the other side also phase stability is different in different solvents. In fact, we observed that in solution 3D-dia and 1D-Cd can form at the same concentration and molar ratio, but 3D-dia request the presence of ethanol in the solvent to form. However, the formation of 3D-dia at the bottom of the tube implies that solvents diffusion is at least as fast as reagents diffusion, limiting the importance of the aforementioned parameter.

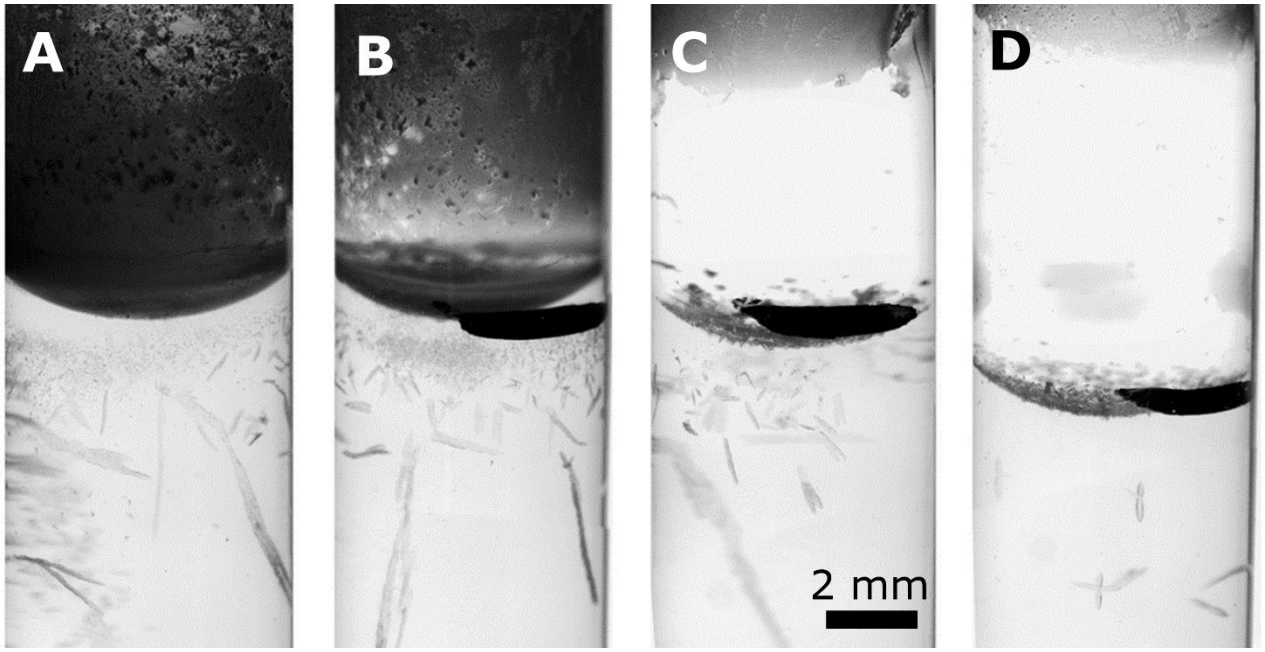

Figure 2.7. test tubes containing ethanolic solution of $CdCl_2$ (M) layered over gelled (1% w/v agarose) water solutions of bpp (L). 2gra139, reagent ratio ([L]/[M]) 0.5, overall concentration ([L]+[M]) 15,2; 2gra140, [L]/[M]=1,0, [L]+[M]=15,1; 2gra141, [L]/[M]=2,0, [L]+[M]=14,7; 2gra142, [L]/[M]=3,1, [L]+[M]=15,3. For sample composition see supporting information.

Counterdiffusion experiments using U-shaped tube

The U-shaped tube is an interesting device for counterdiffusion experiments. It's most intriguing property is that inside it both reagents can diffuse, and all precipitation and crystallization process happen inside gel media. As previously explained, this multiplies the number of experimental conditions that can be simultaneously investigated. Inside a properly settled test tube we could observe the entire phase diagram of the selected systems. Counterdiffusion experiment inside a U-shaped tube where performed to investigate this possibility.

At first place we consider tubes filled whit the same gelled solvent (1% agarose w/v, 40% ethanol v/v), charged with equimolar 1:1 water: ethanol solutions of the reagents. When the charged concentrations reached 80 mM value, precipitation occurs in the horizontal branch. At a higher concentration (120mM for both the reagents), we observed the formation, starting from the ligand charged branch, of crystals of both phase 3D-dia and then phase 3D-sra (Fig.2.8). Their positions along the horizontal branch confirms what previously observed. The phase with higher L/M parameter in its formula (3D-dia) is nearer to the ligand charged branch. The position of the phases strongly suggest that the mobility of the reagents is very different, and that diffusion rate of the cadmium salt is faster respect to ligand molecule diffusion.

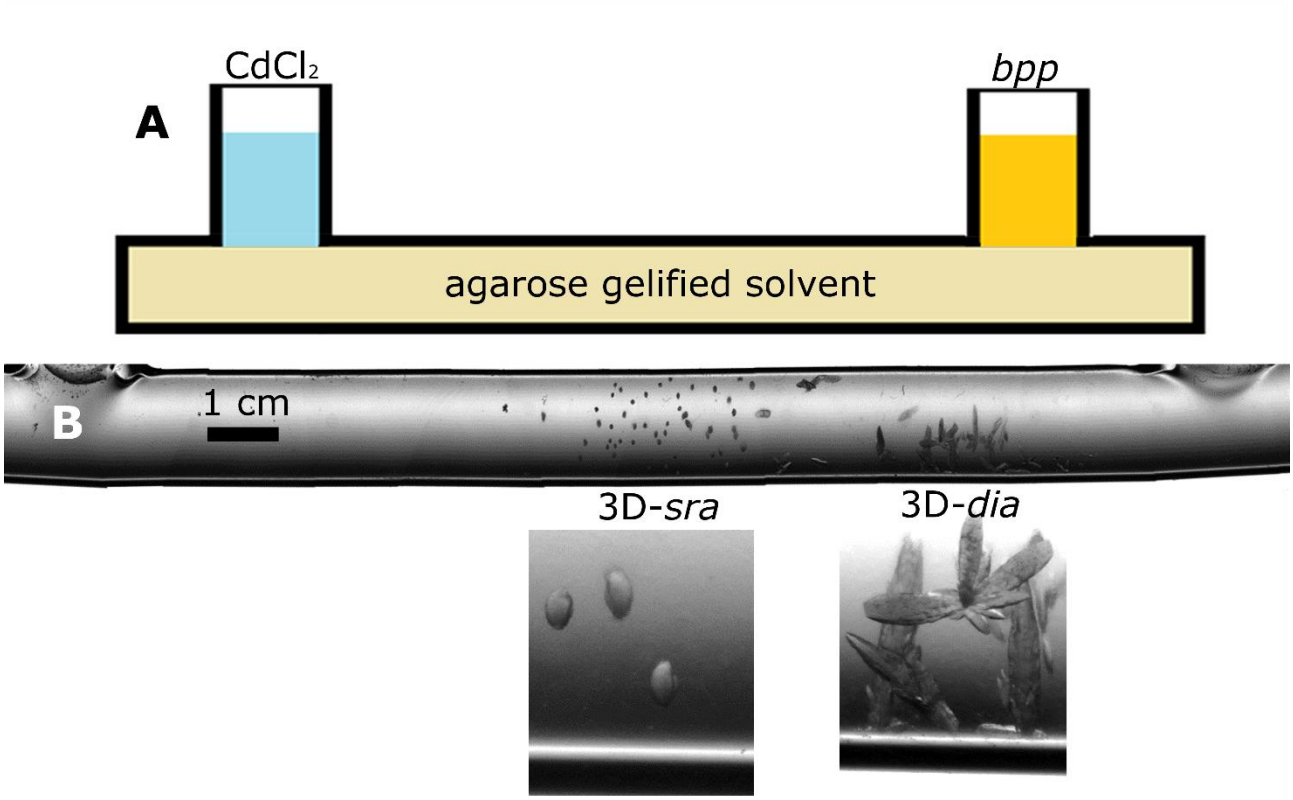

Figure 2.8. U-shaped tube n°7 containing 40:60 water:ethanol gelled (1% w/v agarose) solution. Layered with of $CdCl_2$ (M) 122mM in 1:1 EtOH:water solution (left) and bpp (L) 120,8mM in 1:1 EtOH:water solution (right). Overall concentration [L]+[M]=44,2; reagent ratio [L]/[M]=1; solvent composition 44%EtOH. The upper scheme shows the experimental set-up; the magnified insets shows the two precipitated phases. For sample composition, see supporting information.

Using the same experimental set-up, we were able to confirm the different diffusion rates of the reagents. We prepared two tube using the solvent composition for the gel and the charged solutions previously adopted. One of them was charged with a 40mM solution of the ligand and an 80mM solution of the metal salt, while the other was charged with an 40mM solution of the metal salt and a 80mM solution of the ligand. In the first tube, after two months, we observed the formation of exclusively 3D-sra phase, at the centre of the horizontal branch (Fig.2.9C). Instead, in the second tube occured a transition. At first the tube contained both the phases (Fig.2.9A), then, after other two months, 3D-sra phase disappears and we observed an increase in the number of the 3D-dia phase crystals. 3D-dia crystals reach the half of the horizontal branch (Fig.2.9B). This behaviour confirms that the gel media slows down the diffusion of the ligand solution.

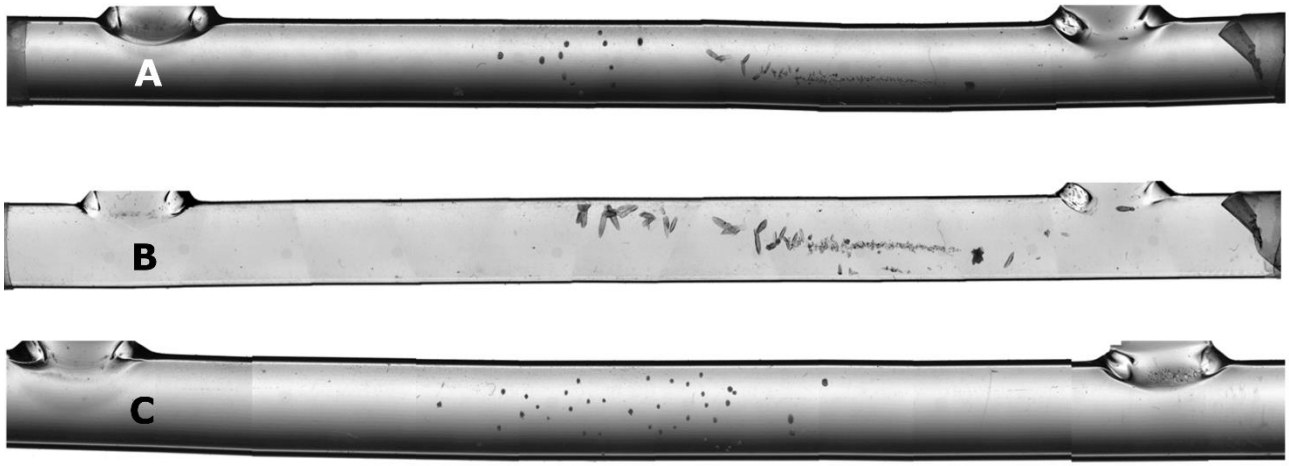

Figure 2.9. U-shaped tube n°3 (C) and n°4(A,B). tubes filled with 40:60 water: ethanolgelled(1% w/v agarose) solution. (A and B) Gel layered with $CdCl_2$ (M) 40 mM in 1:1 EtOH:water solution (left) and bpp (L) 80 mM in 1:1 EtOH:water solution (right). Overall concentration [L]+[M]=22; reagent ratio [L]/[M]=2; solvent composition 44%EtOH. Photographed after 2 months (A) and four months (B). Gel layered with $CdCl_2$ (M) 82 mM in 1:1 EtOH:water solution (left) and bpp (L) 40 mM in 1:1 EtOH:water solution (right). Overall concentration [L]+[M]=22; reagent ratio [L]/[M]=0.5; solvent composition 44%EtOH. Photographed after 2 months (C). For samples compositions see supporting information.

The previous samples also tell us that the effect of the slow diffusion of the reagents is the generation of multiple crystallization environments inside the tube itself, confirming its availability to scan multiple crystallization conditions and observe the entire phase diagram of the system. Hoping to see a more completed phase diagram, we tried to observe also the formation of the 1D-Cd phase. For this purpose, we studied gel with different solvent composition in terms of %EtOH. Inside gel, we consider %EtOH from 15% to 40% using equimolar solution of the reagents (120mM). When EtOH<20% we observed the precipitation of all the three phases (Fig.2.10).

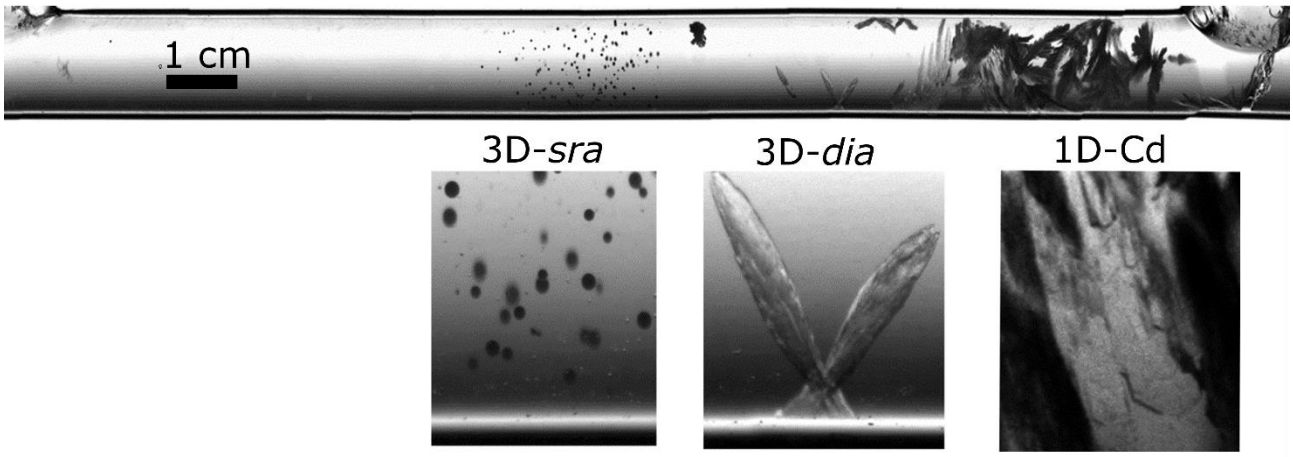

Figure 2.10. U-shaped tube n°15 containing 20:80 water:ethanol gelled (1% w/v agarose) solution. Layered with of $CdCl_2$ (M) 120 mM in 25:75 EtOH:water solution (left) and bpp (L) 120,4 mM in 25:75 EtOH:water solution (right). Overall concentration [L]+[M]=43,8; reagent ratio [L]/[M]=1; solvent composition 22%EtOH. For sample composition see supporting information.

They form starting from the ligand branch and their order is 1D-Cd, 3D-dia, 3D-sra. In particular, we saw the simultaneous precipitation of 3D-dia and 1D-Cd phase. The coexistence of such phases was not detected in solution. Considering the L/M ratio in their formula units (3, 2, 1.5) their disposition is completely consistent with the previously proposed picture of a constantly changing concentration of the reagents along the horizontal branch of the tube. The large formation of 1D-Cd is consistent with the precipitation of powder in solution, confirming its low solubility in this solvent composition. Similar considerations can be done for the 3D-sra phase and the 3D-dia phase, the last one being the only phase that forms large crystals also when precipitated from solution.

Crystal growth kinetics inside gel

The effect of gel concentration on crystal growth has been studied on the system [Cd(*bpp*)$_3$Cl$_2$], a 1D coordination polymer. The experimental set-up was previously described (methods) (Fig.2.11A).

In all samples crystals grow in a similar manner. The nucleation point usually is located at the sol-gel interphase, but also inside the gel. From the nucleation point, one or more branches grow. At first they assume a dendritic aspect but by the time they slightly modify to more regular shapes (Fig.2.11B).

Different gel concentrations are related whit slightly different morphologies of the resulting crystals. For gel concentrations 0,1% and 0,5% was observed a very regular morphology whit sharp angles and plane facets (Fig.2.12A). This regularity is partially lost at gel concentration of about 1%, where can be observed crystals that grew from the axes of the dendrite and perpendicular to it. Crystals growth in gel concentration 3% present a very peculiar aspect. They were aggregates of microscopic platelets that grew perpendicular respect to the axis of the dendrites (Fig.2.12B).

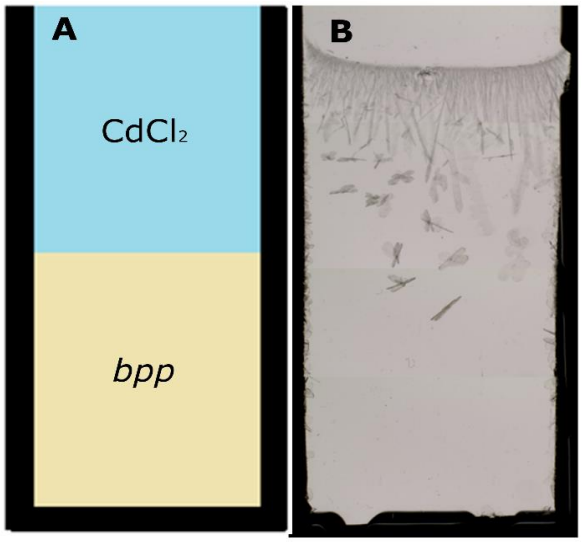

Figure 2.11 schematic representation of the cell used to study crystal growth kinetics (A). Cell used to study crystal growth inside 1% w/v gel (B) $CdCl_2$ 10 mM in gelled water solution layered with 20 mM bpp water

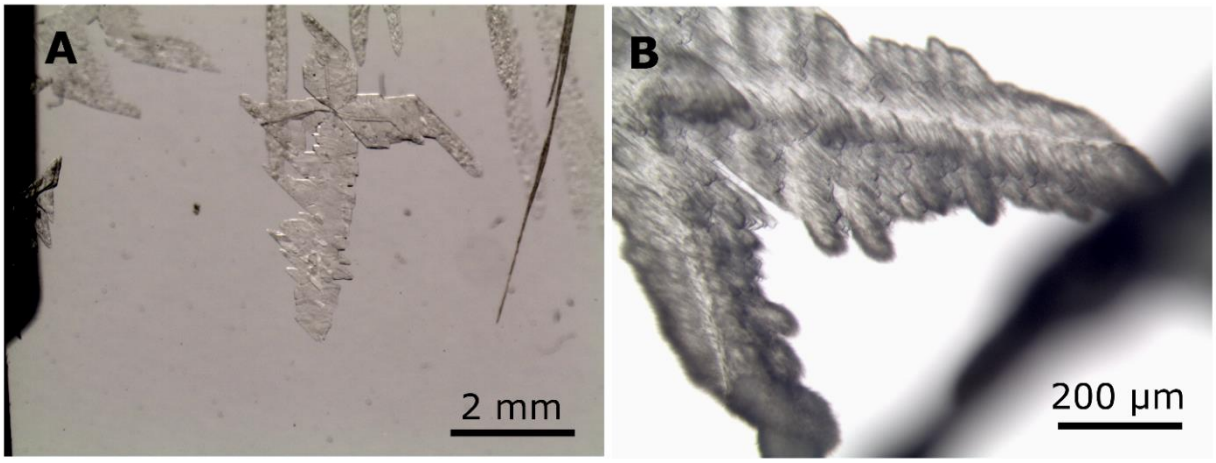

Figure 2.12 1D-Cd crystals grown during kinetic studies inside 0.5 w/v gel (A) and 3% gel (B).

The growth was analysed measuring the length of the main axis of the dendrites in the frames.
In the case of 0.5% w/v gel the length of the single crystal grows plotted respect to the time of growth reveal a parabolic behaviour (Fig.2.13). In the literature is reported that a parabolic behaviour is typical of growth rate determinate by diffusion along a single direction.

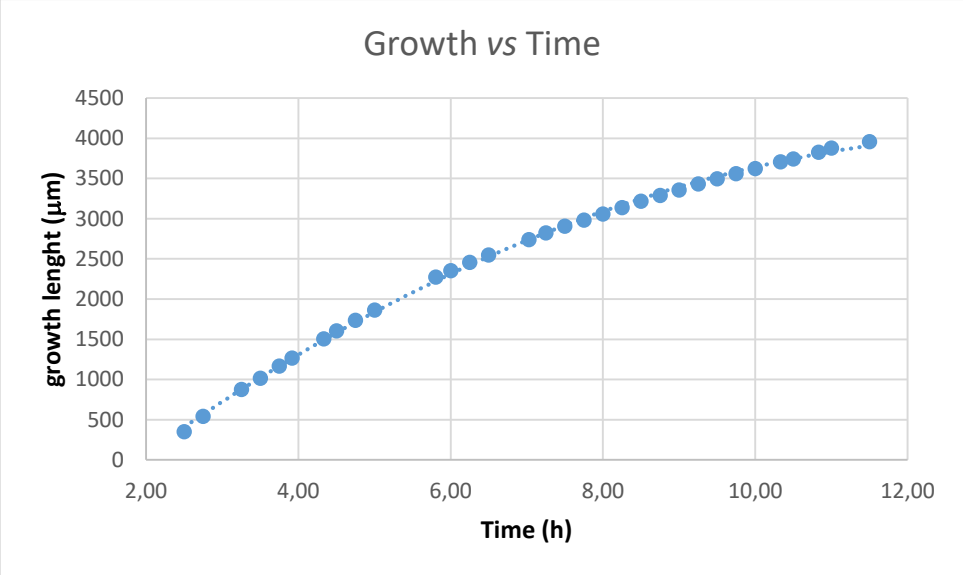

Figure 2.13 plotting of the crystal length against time of growth, agarose concentration: 0.5% w/v. The dotted line is the parabolic function that fitting the data.

In 0,1% w/v, the growth process look different. At first we saw the presence of screw strias over the crystal surface. They are associate whit spiral grow mechanism, that is typical for flat face growing in low supersaturation and is known to form ‘’perfect’’ faces. By the time, the spiral is replaced by new mechanism, as 2D nucleation and adhesive mechanism. The flat surface becomes covered by small well-formed platelets. 2D nucleation is associated with higher supersaturation. In gel of concentration 1% we observed at first a diffusion-dominated kinetics. However, in the last stages the crystals evolve from long dendritic structures to well-formed needles.
Instead, at gel concentration 3% there were a different critical issue. Nucleation inside gel is predominant and no single branch grew enough because the crystals develop as aggregates of small needles.

Conclusions

An extensive study of the crystallization process was performed.
The phase diagram of the system was extensively studied focusing on simple parameter as crystallization media (solution or gel), solvent composition (%EtOH), reagents overall concentration ([M]+[L]) and their molar ratio ([L]/[M]).
We identified in solution proper crystallization condition that let us to isolate single phases and not their mixtures. In particular, phase 3D-sra formation is favoured by a higher amount of metal ions in the solution, but the process is unaffected by the solvent composition. Instead phases 1D-Cd and 3D-

dia precipitation occurs almost at the same concentrations and molar ratio, but in this case the solvent composition is the crucial parameter. For low amount of EtOH (<20%) we observed precipitation of 1D-Cd, while for higher amounts precipitate phase 3D-sra.
Gel media has introduced little modifications in the observed phase diagram. Layering ligand solution over gelled metal solution we observed an increased predominance of the 3D-dia phase, that forms al lower [L]/[M] values. Inside gel the growth of 3D-sra crystals is inhibited, but not their nucleation. In fact, the layering of metal solutions over gelled ligand solutions shows that the presence of gel doesn't affect the stability of a certain phases. Instead, the segregation of the phases (3D-sra in solution, 3D-dia in gel) suggests that the presence of the gel induce the formation of different crystallization environment inside the same sample.
This last hypothesis was definitively confirmed by the counterdiffusion experiments performed inside U-shaped tube. In this case both the reagents freely diffuse from the opposite branches, creating in the different section of the tube slightly different crystallization conditions. For this ligand-metal mixture this has means the possibility to obtained a bunch of different networks.
The study of the crystal growth process introduces an important piece to the picture. In our considered systems we observed the formation of the crystals of phase 1D-Cd, that is highly insoluble. This means that the formation of the crystal is strictly related with the diffusion of the ligand solution inside the cell. For 1% w/v and 0.5%w/v gels we observed a parabolic relation between crystal length and growth time. And this behaviour has been previously associated with growth process limited by mass diffusion.
Gel concentration 0,1% w/v and 3%w/v induce completely different growth process. The softness of 0,1% gel doesn't really affect the diffusion of the reagents, ad after a limited amount of time the concentration of the reagents is high enough to induce 2D nucleation. Instead, inside hard 3%w/v gel the crystals forms aggregates. This suggests that the strength of gel effectively inhibit the diffusion of the layered reagent, creating high concentration related with the formation of small crystals.
Interestingly, gels 1% w/v and 0,5% w/v are the materials that induce the biggest and clear modification in the previously observed phase diagrams. Confirming that the crucial property of the gel media its ability to form purely diffusive media.

Supporting information

Table S.2.1, phase diagram for Cd(II)/bpp mixture in 50% EtOH solvent composition

		Plate I				Plate II			
		D	C	B	A	D	C	B	A
1	[L]+[M] (mM)	60,37	60,43	60,47	60,50	60,52	60,54	60,55	60,56
	[L]/[M]	1,01	1,52	2,02	2,53	3,03	3,54	4,04	4,55
	phases	***sra****	***dia + sra****	***dia+sra***	***dia***	***dia****	***dia****	***dia****	***dia****
2	[L]+[M] (mM)	50,31	50,36	50,39	50,42	50,43	50,45	50,46	50,47
	[L]/[M]	1,01	1,52	2,02	2,53	3,03	3,54	4,04	4,55
	phases	***sra****	***sra+dia***	***dia+sra***	***dia+sra***	***dia+sra***	***dia***	***dia***	***dia***
3	[L]+[M] (mM)	40,25	40,29	40,31	40,33	40,35	40,36	40,37	40,37
	[L]/[M]	1,01	1,52	2,02	2,53	3,03	3,54	4,04	4,55
	phases	***sra****	***sra+dia***	***dia+sra***	***dia+sra***	***dia+sra***	***dia+sra***	***dia***	***dia***
4	[L]+[M] (mM)	30,18	30,21	30,23	30,25	30,26	30,27	30,28	30,28
	[L]/[M]	1,01	1,52	2,02	2,53	3,03	3,54	4,04	4,55
	phases	***sra****	***sra+dia***	***dia+sra***	***dia+sra***	***dia+sra***	***dia+sra***	***dia+sra***	***dia***
5	[L]+[M] (mM)	20,12	20,14	20,16	20,17	20,17	20,18	20,18	20,19
	[L]/[M]	1,01	1,52	2,02	2,53	3,03	3,54	4,04	4,55
	phases	***sra***	***sra+dia***	***dia+sra***	***dia+sra***	***dia+sra***	***dia***	***dia***	***dia***
6	[L]+[M] (mM)	10,06	10,07	10,08	10,08	10,09	10,09	10,09	10,09
	[L]/[M]	1,01	1,52	2,02	2,53	3,03	3,54	4,04	4,55
	phases	***sra***	***dia***	***dia***	***dia***	***dia***	***dia***	/	/

* the well contained powder; / the well was empty

Table S.2.2, Table S.2.1, phase diagram for Cd(II)/bpp mixture at different solvent compositions

		1	2	3	4	5	6
[L]/[M]	A	0,98	0,98	0,98	0,98	0,98	0,98
%H2O		0%	10%	20%	30%	40%	50%
result		***sra***	***sra***	***sra***	***sra/dia***	***sra/dia***	***sra****
[L]/[M]	B	2,03	2,03	2,03	2,03	2,03	2,03
% EtOH		0%	10%	20%	30%	40%	50%
result		***1D-Cd****	***sra****	***dia***	***dia/sra***	***sra/dia***	***sra/dia***
[L]/[M]	C	2,93	2,93	2,93	2,93	2,93	2,93
%H2O		0%	10%	20%	30%	40%	50%
result		***1D-Cd****	***1D-Cd****	***dia***	***dia/sra***	***dia/sra***	***dia/sra***
[L]/[M]	D	3,90	3,90	3,90	3,90	3,90	3,90
%H2O		0%	10%	20%	30%	40%	50%
result		***1D-Cd****	***1D-Cd****	***dia***	***dia***	***dia***	***dia/sra***

* the well contained powder

Table S.2.3 50% phase diagram for Cd(II)/bpp mixture in 50% EtOH solvent composition

plate n°	column [L]/[M]	line	V(M) (mL)	V(L) (mL)	$V(H_2O)$ (mL)	V(EtOH) (mL)	[M] (mM)	[L] (mM)	[M]+[L]
I	1	A	0,57	0,86	0,43	0,14	17,1	43,3	60,5	2,5
I	1	B	0,67	0,80	0,33	0,20	20,1	40,4	60,6	2,0
I	1	C	0,80	0,72	0,20	0,28	24,0	36,4	60,4	1,5
I	1	D	1,00	0,60	0,00	0,40	30,0	30,3	60,4	1,0
I	2	A	0,48	0,71	0,52	0,29	14,4	36,1	50,5	2,5
I	2	B	0,56	0,67	0,44	0,33	16,8	33,7	50,5	2,0
I	2	C	0,67	0,60	0,33	0,40	20,1	30,3	50,5	1,5
I	2	D	0,83	0,50	0,17	0,50	24,9	25,3	50,2	1,0
I	3	A	0,38	0,57	0,62	0,43	11,4	28,9	40,3	2,5
I	3	B	0,44	0,53	0,56	0,47	13,2	27,0	40,2	2,0
I	3	C	0,53	0,48	0,47	0,52	15,9	24,3	40,2	1,5
I	3	D	0,67	0,40	0,33	0,60	20,1	20,2	40,3	1,0
I	4	A	0,29	0,43	0,71	0,57	8,7	21,7	30,4	2,5
I	4	B	0,33	0,40	0,67	0,60	9,9	20,2	30,1	2,0
I	4	C	0,40	0,36	0,60	0,64	12,0	18,2	30,2	1,5
I	4	D	0,50	0,30	0,50	0,70	15,0	15,2	30,2	1,0
I	5	A	0,19	0,29	0,81	0,71	5,7	14,4	20,2	2,5
I	5	B	0,22	0,27	0,78	0,73	6,6	13,5	20,1	2,0
I	5	C	0,27	0,24	0,73	0,76	8,1	12,1	20,2	1,5
I	5	D	0,33	0,20	0,67	0,80	9,9	10,1	20,0	1,0
I	6	A	0,10	0,14	0,90	0,86	3,0	7,2	10,2	2,4
I	6	B	0,11	0,13	0,89	0,87	3,3	6,7	10,0	2,0
I	6	C	0,13	0,12	0,87	0,88	3,9	6,1	10,0	1,6
I	6	D	0,17	0,10	0,83	0,90	5,1	5,1	10,2	1,0
II	1	A	0,36	0,49	0,64	0,51	10,8	24,8	35,6	2,3
II	1	B	0,40	0,48	0,60	0,52	12,0	24,3	36,3	2,0
II	1	C	0,44	0,47	0,56	0,53	13,2	23,6	36,8	1,8
II	1	D	0,5	0,45	0,50	0,55	15,0	22,8	37,8	1,5
II	2	A	0,30	0,98	0,70	0,02	9,0	49,6	58,7	5,5
II	2	B	0,33	0,96	0,67	0,04	9,9	48,5	58,4	4,9
II	2	C	0,37	0,93	0,63	0,07	11,1	47,2	58,3	4,2
II	2	D	0,42	0,90	0,58	0,10	12,6	45,5	58,1	3,6
II	3	A	0,24	0,82	0,76	0,18	7,2	41,4	48,6	5,7
II	3	B	0,27	0,80	0,73	0,20	8,1	40,4	48,6	5,0
II	3	C	0,30	0,78	0,70	0,22	9,0	39,3	48,3	4,4
II	3	D	0,33	0,75	0,67	0,25	9,9	37,9	47,8	3,8
II	4	A	0,18	0,65	0,82	0,35	5,4	33,1	38,5	6,1
II	4	B	0,20	0,64	0,80	0,36	6,0	32,4	38,4	5,4
II	4	C	0,22	0,62	0,78	0,38	6,6	31,5	38,1	4,8
II	4	D	0,25	0,60	0,75	0,40	7,5	30,3	37,8	4,0
II	5	A	0,12	0,33	0,88	0,67	3,6	16,5	20,2	4,6
II	5	B	0,13	0,32	0,87	0,68	3,9	16,2	20,1	4,1
II	5	C	0,15	0,31	0,85	0,69	4,5	15,7	20,2	3,5
II	5	D	0,17	0,30	0,83	0,70	5,1	15,2	20,3	3,0
II	6	A	0,06	0,16	0,94	0,84	1,8	8,3	10,1	4,6
II	6	B	0,07	0,16	0,93	0,84	2,1	8,1	10,2	3,8
II	6	C	0,07	0,16	0,93	0,84	2,1	7,9	10,0	3,7
II	6	D	0,08	0,15	0,92	0,85	2,4	7,6	10,0	3,2

Table S.2.4 20Mm [L]+[M], different solvent composition

Colonna	riga	V (M) mL	V(L) mL	V(H2O) mL	V(EtOH) mL	[M] mM	[L] mM	[L]+[M] mM	[L]/[M]	%EtOH
1	A	0.50	0.50	1.00	0.00	10.3	10.0	20.3	1.0	0
1	B	0.33	0.68	1.00	0.00	6.7	13.5	20.2	2.0	0
1	C	0.25	0.75	1.00	0.00	5.1	15.0	20.1	2.9	0
1	D	0.20	0.80	1.00	0.00	4.1	16.0	20.1	3.9	0
2	A	0.50	0.50	0.80	0.20	10.3	10.0	20.3	1.0	10
2	B	0.33	0.68	0.80	0.20	6.7	13.5	20.2	2.0	10
2	C	0.25	0.75	0.80	0.20	5.1	15.0	20.1	2.9	10
2	D	0.20	0.80	0.80	0.20	4.1	16.0	20.1	3.9	10
3	A	0.50	0.50	0.60	0.40	10.3	10.0	20.3	1.0	20
3	B	0.33	0.68	0.60	0.40	6.7	13.5	20.2	2.0	20
3	C	0.25	0.75	0.60	0.40	5.1	15.0	20.1	2.9	20
3	D	0.20	0.80	0.60	0.40	4.1	16.0	20.1	3.9	20
4	A	0.50	0.50	0.40	0.60	10.3	10.0	20.3	1.0	30
4	B	0.33	0.68	0.40	0.60	6.7	13.5	20.2	2.0	30
4	C	0.25	0.75	0.40	0.60	5.1	15.0	20.1	2.9	30
4	D	0.20	0.80	0.40	0.60	4.1	16.0	20.1	3.9	30
5	A	0.50	0.50	0.20	0.80	10.3	10.0	20.3	1.0	40
5	B	0.33	0.68	0.20	0.80	6.7	13.5	20.2	2.0	40
5	C	0.25	0.75	0.20	0.80	5.1	15.0	20.1	2.9	40
5	D	0.20	0.80	0.20	0.80	4.1	16.0	20.1	3.9	40
6	A	0.50	0.50	0.00	1.00	10.3	10.0	20.3	1.0	50
6	B	0.33	0.68	0.00	1.00	6.7	13.5	20.2	2.0	50
6	C	0.25	0.75	0.00	1.00	5.1	15.0	20.1	2.9	50
6	D	0.20	0.80	0.00	1.00	4.1	16.0	20.1	3.9	50

Figure S.2.1 XRPD patterns used to identify phase 1D-Cd

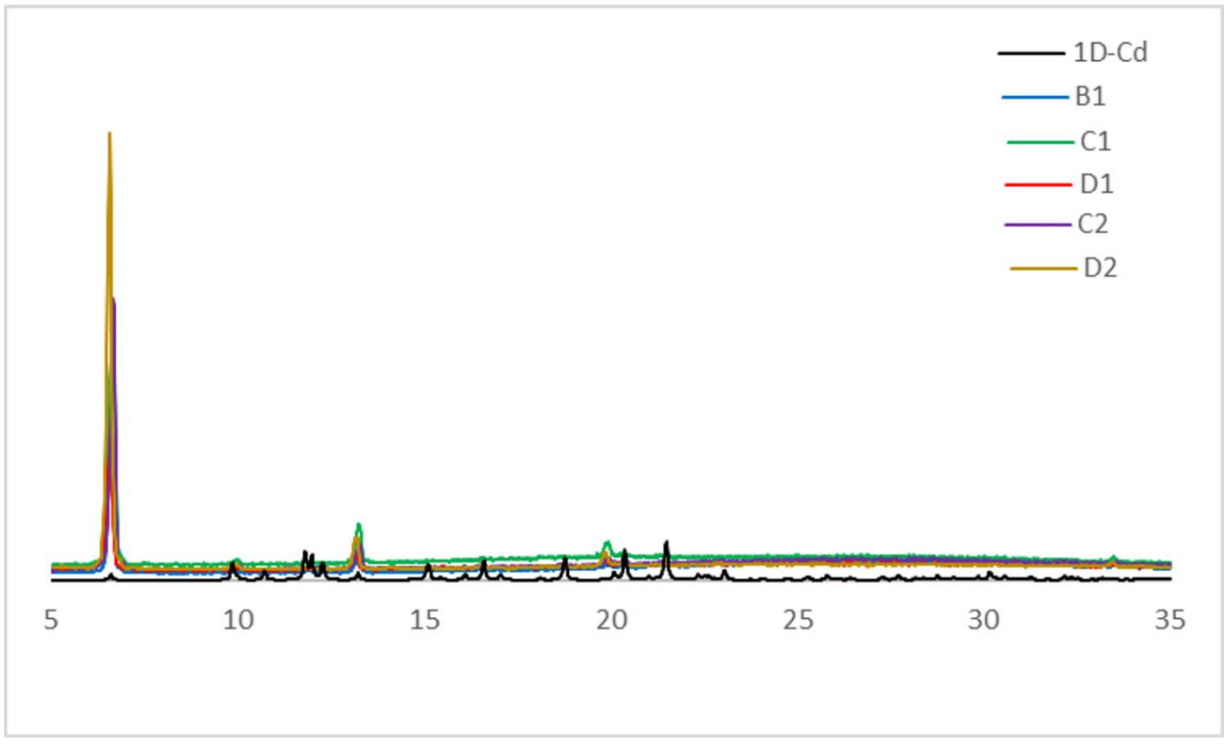

Fig.S.2.2 XRPD patterns of powders precipitated at higher concentrations. From 40mL of a water solution containing $CdCl_2$ (55.6 mg; 15 mM) and *bpp* (127.8 mg; 7.5 mM) we collected powders of pure 3D-sra phase (A).
From 40 mL of an 50% v/v EtOH/H_2O solution containing $CdCl_2$ (114,2 mg; 12.5 mM) and *bpp* (396.5mg; 50 mM) we collected powders of pure 3D-dia phase (B).
From 40 mL of a water solution containing $CdCl_2$ (64 mg; 14 mM) and *bpp* (166.6 mg; 42 mM) we collected powders of pure 1D-Cd phase (C).
Black lines represent calculated spectra for 3D-sra (A), 3D-dia (B), 1D-Cd (C).

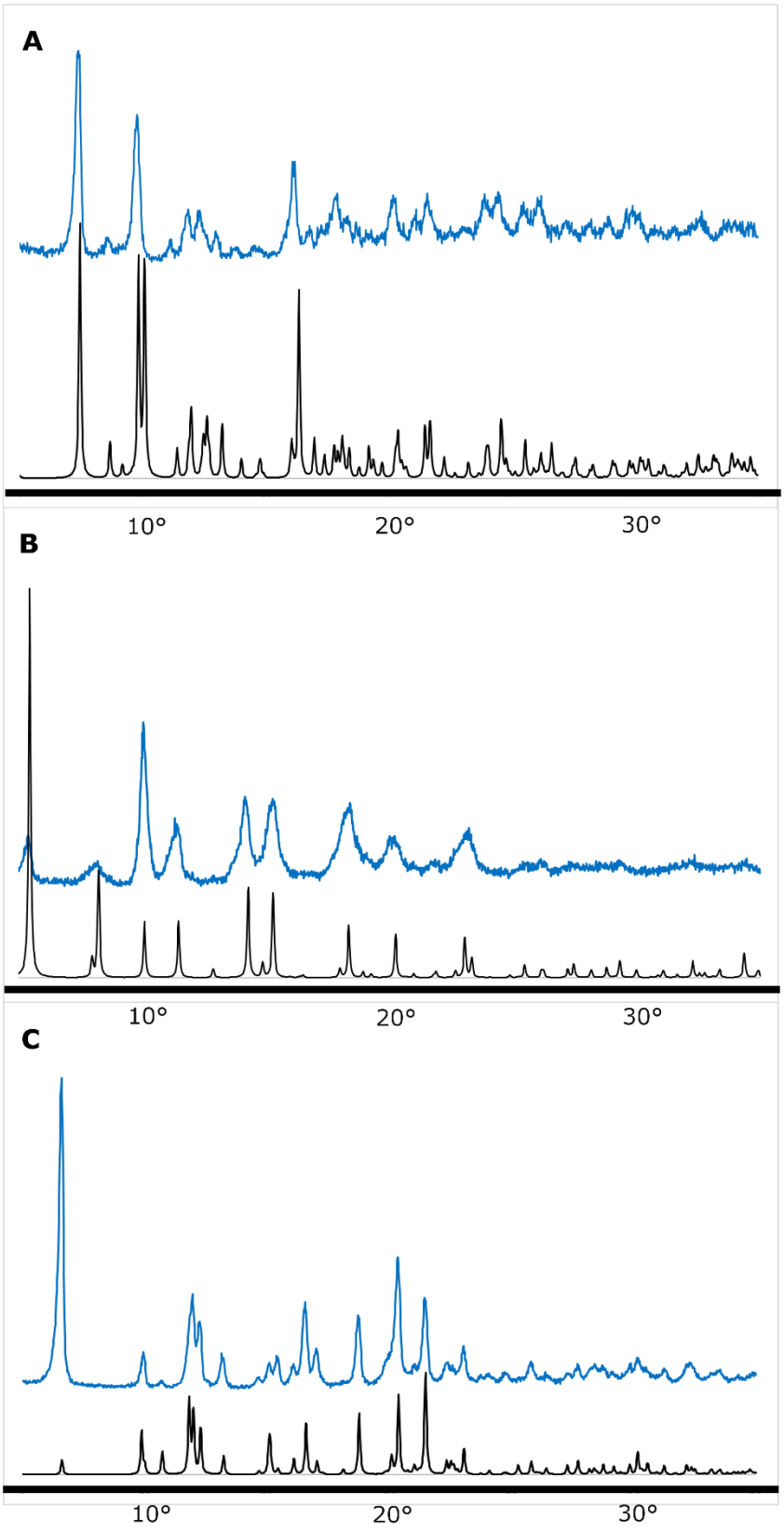

Determination of the phase diagram adopting counterdiffusion inside test tube

Table S.2.5 0,1% w/v agarose

name	agarose concentration	[L]/[M]	[L]+[M]	gel	solution
2gra88	0,1%	0,5	44,2	***sra***	***dia***
2gra91	0,1%	0,5	29,6	***sra***	***dia***
2gra94	0,1%	0,5	15,0	***sra***	***sra***
2gra43	0,1%	1,0	30,3	***sra***	***dia+sra***
2gra46	0,1%	1,0	20,0	\	***sra+dia***
2gra49B	0,1%	1,1	10,3	***sra+dia***	***sra+dia***
2gra89	0,1%	1,5	25,3	\	***sra+dia***
2gra92	0,1%	1,5	16,8	\	***sra+dia***
2gra95	0,1%	1,5	8,3	\	\
2gra42	0,1%	2,0	22,2	***sra***	***dia***
2gra45	0,1%	2,0	15,2	***dia+sra***	
2gra50	0,1%	1,9	16,1	***dia+sra***	
2gra23B	0,1%	2,0	15,0	***sra***	***dia***
2gra48	0,1%	2,1	8,2	\	\
2gra135	0,001	2,3	20,3	***dia+sra***	
2gra136	0,001	2,3	15,1	***dia+sra***	
2gra90	0,1%	2,6	20,8		***dia+sra***
2gra93	0,1%	2,5	14,1		***dia***
2gra96	0,1%	2,5	7,0	\	\
2gra47	0,1%	2,3	7,5	\	\
2gra41	0,1%	3,0	19,7	***dia***	
2gra44	0,1%	2,9	13,5	***dia***	
2gra47B	0,1%	3,6	6,9	\	\

Table S.2.6 0,5% w/v agarose

name	agarose concentration	[L]/[M]	[L]+[M]	gel	solution
2gra70B	0,5%	0,5	45,1	***sra***	***dia***
2gra126	0,50%	0,5	38,0	***sra***	***dia***
2gra76B	0,5%	0,5	30,6	\	***sra+dia***
2gra125	0,5%	0,4	22,2	***sra***	***sra+dia***
2gra79	0,5%	0,5	15,1	***sra***	***sra***
2gra79	0,5%	0,5	16,2	***sra***	***sra***
2gra12	0,5%	1,0	30,3	***dia+sra***	***dia+sra***
2gra11	0,5%	1,0	20,0		***dia+sra***
2gra127	0,5%	1,0	10,2		***dia***
2gra80	0,5%	1,3	8,8	\	\
2gra130	0,5%	1,5	20,2		***dia+sra***
2gra77	0,5%	1,5	16,6	***dia+sra***	***dia+sra***

2gra128	0,5%	1,5	10,0	\	\
2gra20	0,5%	2,0	22,5	***sra***	***dia***
2gra131	0,5%	1,9	19,8	***dia+sra***	***dia+sra***
2gra21	0,5%	2,0	15,1		***dia+sra***
2gra10	0,5%	1,9	14,9	***dia+sra***	\
2gra129	0,5%	2,0	10,5	***dia+sra***	***dia+sra***
2gra81	0,5%	2,3	7,2	\	\
2gra132	0,5%	2,4	19,9	***dia+sra***	\
2gra133	0,5%	2,5	15,1	***dia+sra***	\
2gra19B	0,5%	2,9	20,1	***sra***	***dia***
2gra18	0,5%	3,0	13,2	***dia***	***dia***
2gra17	0,5%	3,0	6,7	\	\

Table S.2.7 1% w/v agarose

name	**agarose concentration**	**[L]/[M]**	**[L]+[M]**	**gel**	**solution**
2gra73	1%	0,5	45,4	***sra***	***dia***
2gra82	1%	0,5	30,6	***sra***	***sra+dia***
2gra85B	1%	0,5	15,5	\	***sra***
2gra7	1%	1,0	29,4	***sra***	***dia***
2gra5	1%	1,0	20,0	***sra***	***dia***
2gra85	1%	0,9	22,1	\	***dia+sra***
2gra9	1%	1,0	10,0	***sra***	***dia***
2gra74B	1%	1,5	25,0	\	***dia+sra***
2gra83	1%	1,5	16,5	\	***dia+sra***
2gra86	1%	1,6	8,1	\	\
2gra23	1%	1,9	22,6	***dia***	***dia***
2gra23B	1%	1,9	22,8	***dia***	***dia***
2gra3	1%	2,0	15,0	***dia***	***dia***
2gra26	1%	2,2	7,7	\	\
2gra87	1%	2,2	7,4	\	\
2gra22	1%	2,5	20,9	***dia***	***dia***
2gra84	1%	2,5	14,0	***dia***	***dia***
2gra22B	1%	3,0	20,3	\	***dia***
2gra24	1%	3,0	13,5	***dia***	***dia***
2gra25	1%	3,0	7,1	\	\
2gra87	1%	2,8	7,3	\	\
2gra1	1%	3,6	12,4	\	\

Table S.2.8 3% w/v agarose

name	agarose concentration	[L]/[M]	[L]+[M]	gel	solution
2gra52	3%	0,5	45,4	***sra***	\
2gra58	3%	0,5	29,8	***sra***	***sra***
2gra64	3%	0,5	15,7	***sra***	***sra***
2gra53	3%	0,9	31,5	\	***sra+dia***
2gra134	3%	1,0	10,1	\	\
2gra59	3%	1,0	19,7	\	***sra+dia***
2gra115	3%	1,7	24,0	***sra***	***dia***
2gra116	3%	1,6	16,2	***dia+sra***	\
2gra60	3%	1,4	18,3	***dia+sra***	***dia***
2gra117	3%	1,7	8,6	***dia***	***dia***
2gra55	3%	2,0	22,7		***dia+sra***
2gra61	3%	2,1	14,7	***dia***	***dia***
2gra67	3%	2,1	7,2	\	\
2gra62	3%	2,5	14,0	\	***dia***
2gra56	3%	2,4	21,3	***dia***	***dia***
2gra68	3%	2,4	7,0	\	\
2gra57	3%	3,0	20,0	***dia***	***dia***
2gra63	3%	3,0	13,3	\	***dia***
2gra69	3%	3,0	6,6	\	\

Table S.2.9 samples composition

code	agarose (mg)	gel (%w/v)	tube d(cm)	L (mg)	M (mg)	V_{EtOH} (mL)	V_{water} (mL)	[L] (mM)	[M] (mM)	L/M	Ctot (mM)
2gra1	50	1,0%	1	15,4	4,9	4,0	4,0	19,4	5,4	3,6	12,4
2gra3	50	1,0%	1	15,9	9,0	4,0	4,0	20,0	9,9	2,0	15,0
2gra5	50	1,0%	1	15,7	18,4	4,0	4,0	19,8	20,1	1,0	20,0
2gra7	50	1,0%	1	22,8	27,5	4,0	4,0	28,7	30,1	1,0	29,4
2gra9	50	1,0%	1	7,9	11,4	4,0	5,0	10,0	10,0	1,0	10,0
2gra10	25	0,5%	1	15,4	11,9	4,0	5,0	19,4	10,4	1,9	14,9
2gra11	25	0,5%	1	15,7	23,0	4,0	5,0	19,8	20,1	1,0	20,0
2gra12	25	0,5%	1	23,9	34,8	4,0	5,0	30,1	30,5	1,0	30,3
2gra17	25	0,5%	1	7,0	3,8	3,5	5,0	10,1	3,3	3,0	6,7
2gra18	25	0,5%	1	13,7	7,6	3,5	5,0	19,7	6,7	3,0	13,2
2gra19	25	0,5%	1	20,7	11,9	3,5	5,0	29,8	10,4	2,9	20,1
2gra20	25	0,5%	1	20,9	16,9	3,5	5,0	30,1	14,8	2,0	22,5
2gra21	25	0,5%	1	14,0	11,4	3,5	5,0	20,2	10,0	2,0	15,1
2gra22	50	1,0%	1	21,0	11,7	3,5	5,0	30,3	10,2	3,0	20,3
2gra23	50	1,0%	1	20,7	17,5	3,5	5,0	29,8	15,3	1,9	22,6
2gra24	50	1,0%	1	14,1	7,7	3,5	5,0	20,3	6,7	3,0	13,5
2gra25	50	1,0%	1	7,4	4,0	3,5	5,0	10,7	3,5	3,0	7,1
2gra26	50	1,0%	1	7,4	5,5	3,5	5,0	10,7	4,8	2,2	7,7
2gra41	5	0,1%	1	20,5	11,3	3,5	5,0	29,5	9,9	3,0	19,7
2gra42	5	0,1%	1	20,5	17,0	3,5	5,0	29,5	14,9	2,0	22,2
2gra43	5	0,1%	1	21,3	34,2	3,5	5,0	30,7	30,0	1,0	30,3

code	agarose (mg)	gel (%w/v)	tube d(cm)	L (mg)	M (mg)	V_{EtOH} (mL)	V_{water} (mL)	[L] (mM)	[M] (mM)	L/M	Ctot (mM)
2gra44	5	0,1%	1	13,9	7,9	3,5	5,0	20,0	6,9	2,9	13,5
2gra45	5	0,1%	1	14,0	11,6	3,5	5,0	20,2	10,2	2,0	15,2
2gra46	5	0,1%	1	13,9	22,9	3,5	5,0	20,0	20,1	1,0	20,0
2gra47	5	0,1%	1	7,1	4,0	3,5	5,0	10,2	3,5	2,9	6,9
2gra48	5	0,1%	1	7,7	6,0	3,5	5,0	11,1	5,3	2,1	8,2
2gra49	5	0,1%	1	7,1	11,9	3,5	5,0	10,2	10,4	1,0	10,3
2gra52	150	3,0%	1	149,5	69,3	25,0	5,0	30,2	60,7	0,5	45,4
2gra53	150	3,0%	1	149,5	37,5	25,0	5,0	30,2	32,8	0,9	31,5
2gra54	150	3,0%	1	149,5	23,1	25,0	5,0	30,2	20,2	1,5	25,2
2gra55	150	3,0%	1	149,5	17,5	25,0	5,0	30,2	15,3	2,0	22,7
2gra56	150	3,0%	1	149,5	14,2	25,0	5,0	30,2	12,4	2,4	21,3
2gra57	150	3,0%	1	149,5	11,3	25,0	5,0	30,2	9,9	3,0	20,0
2gra58	150	3,0%	1	99,1	45,3	25,0	5,0	20,0	39,7	0,5	29,8
2gra59	150	3,0%	1	99,1	22,1	25,0	5,0	20,0	19,4	1,0	19,7
2gra60	150	3,0%	1	99,1	15,2	25,0	5,0	20,0	13,3	1,5	16,7
2gra61	150	3,0%	1	99,1	10,8	25,0	5,0	20,0	9,5	2,1	14,7
2gra62	150	3,0%	1	99,1	9,2	25,0	5,0	20,0	8,1	2,5	14,0
2gra63	150	3,0%	1	99,1	7,6	25,0	5,0	20,0	6,7	3,0	13,3
2gra64	150	3,0%	1	48,8	24,5	25,0	5,0	9,8	21,5	0,5	15,7
2gra65	150	3,0%	1	48,8	11,5	25,0	5,0	9,8	10,1	1,0	10,0
2gra66	150	3,0%	1	48,8	7,8	25,0	5,0	9,8	6,8	1,4	8,3
2gra67	150	3,0%	1	48,8	5,3	25,0	5,0	9,8	4,6	2,1	7,2
2gra68	150	3,0%	1	48,8	4,7	25,0	5,0	9,8	4,1	2,4	7,0
2gra69	150	3,0%	1	48,8	3,8	25,0	5,0	9,8	3,3	3,0	6,6
2gra70	25	0,5%	1	147,0	71,2	25,0	5,0	29,7	62,4	0,5	46,0
2gra71	25	0,5%	1	147,0	22,5	25,0	5,0	29,7	19,7	1,5	24,7
2gra72	25	0,5%	1	147,0	13,3	25,0	5,0	29,7	11,6	2,5	20,7
2gra73	50	1,0%	1	149,5	69,3	25,0	5,0	30,2	60,7	0,5	45,4
2gra74	50	1,0%	1	149,5	23,1	25,0	5,0	30,2	20,2	1,5	25,2
2gra75	50	1,0%	1	149,5	14,2	25,0	5,0	30,2	12,4	2,4	21,3
2gra76	25	0,5%	1	117,6	47,4	30,0	5,0	19,8	41,5	0,5	30,6
2gra77	25	0,5%	1	117,6	15,3	30,0	5,0	19,8	13,4	1,5	16,6
2gra78	25	0,5%	1	117,6	9,9	30,0	5,0	19,8	8,7	2,3	14,2
2gra79	25	0,5%	1	59,9	23,0	30,0	5,0	10,1	20,1	0,5	15,1
2gra80	25	0,5%	1	59,9	8,6	30,0	5,0	10,1	7,5	1,3	8,8
2gra81	25	0,5%	1	59,9	5,0	30,0	5,0	10,1	4,4	2,3	7,2
2gra82	50	1,0%	1	117,6	47,4	30,0	5,0	19,8	41,5	0,5	30,6
2gra83	50	1,0%	1	117,6	15,2	30,0	5,0	19,8	13,3	1,5	16,5
2gra84	50	1,0%	1	117,6	10,2	30,0	5,0	19,8	8,9	2,2	14,4
2gra85	50	1,0%	1	59,9	24,0	30,0	5,0	10,1	21,0	0,5	15,5
2gra86	50	1,0%	1	59,9	7,1	30,0	5,0	10,1	6,2	1,6	8,1
2gra87	50	1,0%	1	59,9	5,3	30,0	5,0	10,1	4,6	2,2	7,4
2gra88	5	0,1%	1	178,5	66,6	30,0	5,0	30,0	58,3	0,5	44,2
2gra89	5	0,1%	1	178,5	23,6	30,0	5,0	30,0	20,7	1,5	25,3
2gra90	5	0,1%	1	178,5	13,3	30,0	5,0	30,0	11,6	2,6	20,8
2gra91	5	0,1%	1	119,2	44,7	30,0	5,0	20,0	39,2	0,5	29,6

code	agarose (mg)	gel (%w/v)	tube d(cm)	L (mg)	M (mg)	V_{EtOH} (mL)	V_{water} (mL)	[L] (mM)	[M] (mM)	L/M	Ctot (mM)
2gra92	5	0,1%	1	119,2	15,5	30,0	5,0	20,0	13,6	1,5	16,8
2gra93	5	0,1%	1	119,2	9,3	30,0	5,0	20,0	8,1	2,5	14,1
2gra94	5	0,1%	1	59,2	23,1	30,0	5,0	10,0	20,2	0,5	15,1
2gra95	5	0,1%	1	59,2	7,5	30,0	5,0	10,0	6,6	1,5	8,3
2gra96	5	0,1%	1	59,2	4,6	30,0	5,0	10,0	4,0	2,5	7,0
2gra22B	50	1,0%	1	147,3	13,8	25,0	5,0	29,7	12,1	2,5	20,9
2gra23B	50	1,0%	1	147,3	18,2	25,0	5,0	29,7	15,9	1,9	22,8
2gra47B	5	0,1%	1	52,1	5,2	25,0	5,0	10,5	4,6	2,3	7,5
2gra50B	5	0,1%	1	104,5	12,8	25,0	5,0	21,1	11,2	1,9	16,1
2gra51B	5	0,1%	1	104,5	13,0	25,0	5,0	21,1	11,4	1,9	16,2
2gra60B	150	3,0%	1	104,5	17,8	25,0	5,0	21,1	15,6	1,4	18,3
2gra65B	150	3,0%	1	52,1	11,9	25,0	5,0	10,5	10,4	1,0	10,5
2gra74B	50	1,0%	1	147,3	23,1	25,0	5,0	29,7	20,2	1,5	25,0
2gra85B	50	1,0%	1	104,5	26,3	25,0	5,0	21,1	23,0	0,9	22,1
2gra94B	5	0,1%	1	52,1	22,3	25,0	5,0	10,5	19,5	0,5	15,0
2gra19B	25	0,5%	1	147,3	12,1	25,0	5,0	29,7	10,6	2,8	20,2
2gra70B	25	0,5%	1	147,3	69,1	25,0	5,0	29,7	60,5	0,5	45,1
2gra71B	25	0,5%	1	147,3	22,5	25,0	5,0	29,7	19,7	1,5	24,7
2gra72B	25	0,5%	1	147,3	16,2	25,0	5,0	29,7	14,2	2,1	22,0
2gra76B	25	0,5%	1	104,5	46,6	25,0	5,0	21,1	40,8	0,5	30,9
2gra79B	25	0,5%	1	52,1	25,0	25,0	5,0	10,5	21,9	0,5	16,2
2gra30B	5	0,1%	1	148,9	18,1	25,0	5,0	30,0	15,9	1,9	22,9
2gra23C	5	0,1%	1	99,6	11,4	25,0	5,0	20,1	10,0	2,0	15,0
2gra47C	5	0,1%	1	53,7	3,4	25,0	5,0	10,8	3,0	3,6	6,9
2gra49B	5	0,1%	1	53,7	11,2	25,0	5,0	10,8	9,8	1,1	10,3
2gra75B	50	1,0%	1	148,9	13,6	25,0	5,0	30,0	11,9	2,5	21,0
2gra84B	50	1,0%	1	99,6	9,1	25,0	5,0	20,1	8,0	2,5	14,0
2gra87B	50	1,0%	1	53,7	4,4	25,0	5,0	10,8	3,9	2,8	7,3
2gra90B	50	1,0%	1	148,9	14,2	25,0	5,0	30,0	12,4	2,4	21,2
2gra93B	50	1,0%	1	99,6	9,9	25,0	5,0	20,1	8,7	2,3	14,4
2gra115	150	3,0%	1	148,9	20,6	25,0	5,0	30,0	18,0	1,7	24,0
2gra116	150	3,0%	1	99,6	14,0	25,0	5,0	20,1	12,3	1,6	16,2
2gra117	150	3,0%	1	53,7	7,3	25,0	5,0	10,8	6,4	1,7	8,6
2gra125	25	0,5%	1	300,9	35,3	112,0	5,0	13,6	30,9	0,4	22,2
2gra126	25	0,5%	1	300,9	58,2	61,0	5,0	24,9	51,0	0,5	37,9
2gra127	25	0,5%	1	300,9	11,8	152,0	5,0	10,0	10,3	1,0	10,2
2gra128	25	0,5%	1	300,9	9,2	127,0	5,0	11,9	8,1	1,5	10,0
2gra129	25	0,5%	1	300,9	8,1	108,0	5,0	14,1	7,1	2,0	10,6
2gra130	25	0,5%	1	300,9	18,7	63,0	5,0	24,1	16,4	1,5	20,2
2gra131	25	0,5%	1	300,9	15,6	58,0	5,0	26,2	13,7	1,9	19,9
2gra132	25	0,5%	1	300,9	13,4	54,0	5,0	28,1	11,7	2,4	19,9
2gra133	25	0,5%	1	300,9	9,9	71,0	5,0	21,4	8,7	2,5	15,0
2gra134	150	3,0%	1	300,9	11,6	152,0	5,0	10,0	10,2	1,0	10,1
2gra135	5	0,1%	1	300,9	14,0	53,0	5,0	28,6	12,3	2,3	20,4
2gra136	5	0,1%	1	300,9	10,5	73,0	5,0	20,8	9,2	2,3	15,0
2gra137	50	1,0%	1	300,9	11,0	60,0	5,0	25,3	9,6	2,6	17,5

code	agarose (mg)		gel (%w/v)	tube d(cm)	L (mg)	M (mg)	V_{EtOH} (mL)	V_{water} (mL)	[L] (mM)	[M] (mM)	L/M	Ctot (mM)
2gra138		50	1,0%	1	300,9	8,0	83,0	5,0	18,3	7,0	2,6	12,6
2gra1		50	1,0%	1	15,4	4,9	4,0	4,0	19,4	5,4	3,6	24,8
2gra3		50	1,0%	1	15,9	9,0	4,0	4,0	20,0	9,9	2,0	29,9
2gra5		50	1,0%	1	15,7	18,4	4,0	4,0	19,8	20,1	1,0	39,9
2gra7		50	1,0%	1	22,8	27,5	4,0	4,0	28,7	30,1	1,0	58,9
2gra9		50	1,0%	1	7,9	11,4	4,0	5,0	10,0	10,0	1,0	19,9
2gra10		25	0,5%	1	15,4	11,9	4,0	5,0	19,4	10,4	1,9	29,8
2gra11		25	0,5%	1	15,7	23,0	4,0	5,0	19,8	20,1	1,0	39,9
2gra12		25	0,5%	1	23,9	34,8	4,0	5,0	30,1	30,5	1,0	60,6
2gra17		25	0,5%	1	7,0	3,8	3,5	5,0	10,1	3,3	3,0	13,4
2gra18		25	0,5%	1	13,7	7,6	3,5	5,0	19,7	6,7	3,0	26,4
2gra19		25	0,5%	1	20,7	11,9	3,5	5,0	29,8	10,4	2,9	40,3
2gra20		25	0,5%	1	20,9	16,9	3,5	5,0	30,1	14,8	2,0	44,9
2gra21		25	0,5%	1	14,0	11,4	3,5	5,0	20,2	10,0	2,0	30,2
2gra22		50	1,0%	1	21,0	11,7	3,5	5,0	30,3	10,2	3,0	40,5
2gra23		50	1,0%	1	20,7	17,5	3,5	5,0	29,8	15,3	1,9	45,2
2gra24		50	1,0%	1	14,1	7,7	3,5	5,0	20,3	6,7	3,0	27,1
2gra25		50	1,0%	1	7,4	4,0	3,5	5,0	10,7	3,5	3,0	14,2
2gra26		50	1,0%	1	7,4	5,5	3,5	5,0	10,7	4,8	2,2	15,5
2gra41		5	0,1%	1	20,5	11,3	3,5	5,0	29,5	9,9	3,0	39,4
2gra42		5	0,1%	1	20,5	17,0	3,5	5,0	29,5	14,9	2,0	44,4
2gra43		5	0,1%	1	21,3	34,2	3,5	5,0	30,7	30,0	1,0	60,6
2gra44		5	0,1%	1	13,9	7,9	3,5	5,0	20,0	6,9	2,9	26,9
2gra45		5	0,1%	1	14,0	11,6	3,5	5,0	20,2	10,2	2,0	30,3
2gra46		5	0,1%	1	13,9	22,9	3,5	5,0	20,0	20,1	1,0	40,1
2gra47		5	0,1%	1	7,1	4,0	3,5	5,0	10,2	3,5	2,9	13,7
2gra48		5	0,1%	1	7,7	6,0	3,5	5,0	11,1	5,3	2,1	16,4
2gra49		5	0,1%	1	7,1	11,9	3,5	5,0	10,2	10,4	1,0	20,7
2gra52		150	3,0%	1	149,5	69,3	25,0	5,0	30,2	60,7	0,5	90,9
2gra53		150	3,0%	1	149,5	37,5	25,0	5,0	30,2	32,8	0,9	63,0
2gra54		150	3,0%	1	149,5	23,1	25,0	5,0	30,2	20,2	1,5	50,4

Table S.2.9 layering of metal ethanolic solution over water gelled ligand solution

code	[gel]	L/M	Ctot	gel	sol
2gra147	0,1%	0,49	14,95	***dia+sra***	***sra***
2gra148	0,1%	1	15,02	***dia+sra***	***sra***
2gra149	0,1%	1,93	14,635	***dia***	***sra***
2gra150	0,1%	2,9	14,645	***dia***	***sra***
2gra143	0,5%	0,51	15,1	***dia+sra***	***sra***
2gra144	0,5%	1,03	15,27	***dia+sra***	***sra***
2gra145	0,5%	1,99	14,94	***dia***	***sra***
2gra146	0,5%	3,10	16,00398	***dia***	***sra***
2gra139	1%	0,51	15,15	***dia+sra***	***sra***
2gra140	1%	1,01	15,12	***dia+sra***	***sra***
2gra141	1%	1,95	14,74	***dia***	***sra***
2gra142	1%	3,06	15,25	***dia***	***sra***
2gra151	3%	0,48	14,785	***dia+sra***	***sra***
2gra152	3%	1,05	15,17	***dia+sra***	***sra***
2gra153	3%	1,92	14,58	***dia***	***sra***
2gra154	3%	3,15	15,355	***dia***	***sra***

Table S.2.9 layering of metal ethanolic solution over water gelled ligand solution, samples composition

code	agarose (mg)	gel (%w/v)	tube d(cm)	L (mg)	M (mg)	V_{EtOH} (mL)	V_{water} (mL)	[L] (mM)	[M] (mM)	L/M	Ctot (mM)
2gra139	50	1,0%	1	10,2	137,1	5	30	10,3	20,0	0,5	15,2
2gra140	50	1,0%	1	15,1	137,1	5	40	15,2	15,0	1,0	15,1
2gra141	50	1,0%	1	19,3	137,1	5	60	19,5	10,0	2,0	14,7
2gra142	50	1,0%	1	22,8	137,1	5	80	23,0	7,5	3,1	15,3
2gra143	25	0,5%	1	10,1	137,1	5	30	10,2	20,0	0,5	15,1
2gra144	25	0,5%	1	15,4	137,1	5	40	15,5	15,0	1,0	15,3
2gra145	25	0,5%	1	19,7	137,1	5	60	19,9	10,0	2,0	14,9
2gra146	25	0,5%	1	24	137,1	5	20	24,2	30,0	0,8	27,1
2gra147	5	0,1%	1	9,8	137,1	5	30	9,9	20,0	0,5	14,9
2gra148	5	0,1%	1	14,9	137,1	5	40	15,0	15,0	1,0	15,0
2gra149	5	0,1%	1	19,1	137,1	5	60	19,3	10,0	1,9	14,6
2gra150	5	0,1%	1	21,6	137,1	5	80	21,8	7,5	2,9	14,6
2gra151	150	3,0%	1	9,5	91,3	5	20	9,6	20,0	0,5	14,8
2gra152	150	3,0%	1	15,4	91,3	5	27	15,5	14,8	1,1	15,2
2gra153	150	3,0%	1	19	91,3	5	40	19,2	10,0	1,9	14,6
2gra154	150	3,0%	1	23,1	91,3	5	54	23,3	7,4	3,2	15,4

Table S.2.9 U-shaped tube, overall parameters and results

n°	[M] (mM)	[L] (mM)	[L]/[M]	[L]+[M] (mM)	V (mL)	V (mL)	%EtOH	results
1	11,3	11,4	1,0	22,6	1,9	2,5	44%	\
2	7,5	7,6	1,0	15,1	1,9	2,5	44%	\
3	14,9	7,3	0,5	22,2	1,9	2,5	44%	sra
4	7,4	14,5	2,0	22,0	1,9	2,5	44%	sra+dia, then exclusively dia
5	14,9	14,5	1,0	29,4	1,9	2,5	44%	sra+dia
6	5,6	5,7	1,0	11,3	1,9	2,5	44%	\
7	22,2	22,0	1,0	44,2	1,9	2,5	44%	sra+dia
8	22,2	22,0	1,0	44,2	1,9	2,5	44%	\
9	22,2	21,6	1,0	43,7	1,9	2,5	44%	sra+dia
10	14,8	14,4	1,0	29,1	1,9	2,5	44%	sra+dia
11	22,2	21,6	1,0	43,7	1,9	2,5	44%	sra+dia
12	14,8	14,4	1,0	29,1	1,9	2,5	44%	sra+dia
13	22,2	22,5	1,0	44,7	1,4	3,0	31%	sra+dia
14	14,8	15,0	1,0	29,8	1,4	3,0	31%	sra+dia
15	21,9	21,9	1,0	43,8	1,0	3,4	22%	sra+dia+1D
16	14,6	14,6	1,0	29,2	1,0	3,4	22%	sra+dia+1D
17	21,9	21,9	1,0	43,8	0,7	3,7	15%	sra+dia+1D
18	14,6	14,6	1,0	29,2	0,7	3,7	15%	sra+dia+1D

Table S.2.9 U-shaped tube, samples preparation

	AGAROSE GEL				METAL SOLUTION				LIGAND SOLUTION			
sample n°	agar mg	gel %w/v	V (mL)	%EtoH	M (mg)	V (mL)	%EtOH	[M] (mM)	L (mg)	V (mL)	%EtOH	[L] mM
1	200	1%	20	40%	283	20	50%	62	248	20	50%	62,4
2	200	1%	20	40%	284	30	50%	41	248	30	50%	41,6
3	200	1%	20	40%	94	5	50%	82	79	10	50%	40,0
4	200	1%	20	40%	94	10	50%	41	79	5	50%	80,0
5	200	1%	20	40%	94	5	50%	82	79	5	50%	80,0
6	200	1%	20	40%	283	40	50%	31	248	40	50%	31,2
7	300	1%	30	40%	558	20	50%	122	479	20	50%	120,8
8	300	1%	30	40%	558	20	50%	122	479	20	50%	120,8
9	50	0,5%	10	40%	278	10	50%	122	235	10	50%	118,6
10	50	0,5%	10	40%	278	15	50%	81	235	15	50%	79,1
11	300	3%	10	40%	278	10	50%	122	235	10	50%	118,6
12	300	3%	10	40%	278	15	50%	81	235	15	50%	79,1
13	100	1%	20	30%	279	10	33%	122	246	10	33%	123,9
14	100	1%	20	30%	279	15	33%	81	246	15	33%	82,6
15	100	1%	20	20%	275	10	25%	120	239	10	25%	120,4
16	100	1%	20	20%	275	15	25%	80	239	15	25%	80,3
17	100	1%	20	10%	275	10	25%	120	239	10	25%	120,4
18	100	1%	20	10%	275	15	25%	80	239	15	25%	80,3

Bibliography

1. Carlucci, L. *et al.* Crystallization behavior of coordination polymers. 1. kinetic and thermodynamic features of 1,3-Bis(4-pyridyl)propane/MCl2 Systems. *Cryst. Growth Des.* **9,** 5024–5034 (2009).
2. Luo, F., Che, Y. xia & Zheng, J. min. Synthesis, structures and characters of one 3D 2-fold interpenetrating net with rare 42638 topology. *Inorg. Chem. Commun.* **9,** 856–858 (2006).
3. Rizzato, S., Moret, M., Merlini, M., Albinati, A. & Beghi, F. Crystal growth in gelled solution: applications to coordination polymers. *CRYSTENGCOMM* **18,** 2455–2462 (2016).
4. Rizzato, S., Moret, M., Merlini, M., Albinati, A. & Beghi, F. Crystal growth in gelled solution: applications to coordination polymers. *Crystengcomm* **18,** 2455–2462 (2016).

II-System Cu(II)/isonicotinic acid

Introduction

In CSD database (March 2016 release) there are more than 500 structures containing isonicotinic acid (HIso) revealing both the arising interest in this ligand and the high variability in terms of structures and topologies that can be obtained from such a simple molecule.

The molecule is rigid. In fact, its only degree of freedom is the dihedral angle between the pyridine ring and the carboxylic group. It bears both an acidic site and a basic site. The dissociation constants were determined from UV adsorption data. pKa of Carboxylic group is 4.95, while the protonated nitrogen has an pKa of 1.7. The isoelectric point is at pH value 3.45 (Fig.3.1).[1]

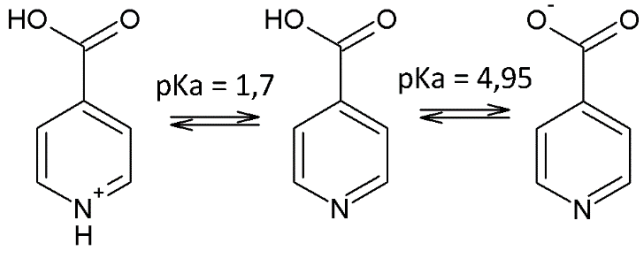

Figure 3.1 acid-base behaviour of isonicotinic acid

The proton of the carboxylic group and the nitrogen of the pyridine ring can form a strong hydrogen bond. This behaviour is important for the crystal structure of HIso (refcode: ISNICA),[2] that contains infinite chains of HIso molecules bonded trough this hydrogen bonds. When used as a ligand, its ability to form hydrogens bonds is displayed towards other ligands or water molecules, resulting in interesting effects in the supramolecular architecture.

The ligand can bond the metals when protonated (HIso) or deprotonated (Iso), with both the two sites. Considering a large group of 500 HIso ligand-containing structures, nine different coordination modes have been identified [3] (Fig.3.2). In five of these mode (A, B, C, E, I) the ligand acts as bridge joining different metal centres, but only in the A, B, C modes it uses both the nitrogen and the oxygen atoms. In the D, F, G, H modes Iso acts as a monodentate ligand. For an undissociated acid molecule, mode G is the only feasible. In the modes H and I HIso assumes a zwitterionic form.

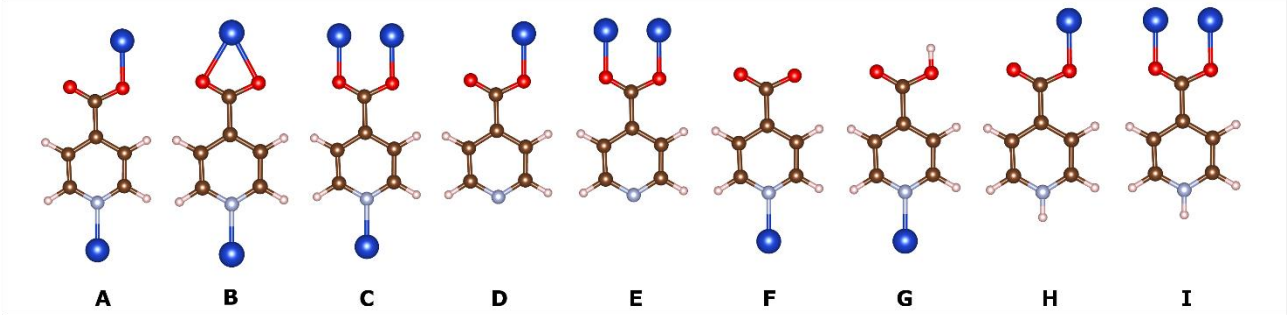

Fig 3.2 HIso coordination modes, from left to right:

INA κ-N, κ-O (η^1:η^1:μ^2) (A); κ-N, κ-O, κ-O (η^1:η^1:η^1:μ^2)(B) ; κ-N, κ-O, κ-O (η^1:η^1:η^1:μ^3)(C); (D); κ-O, κ-O (η^1:η^1:μ^2)(E) ; κ-N (F); HINA κ-N (η^1:η^1:μ^2)(G), κ-O (H), κ-O, κ-O (η^1:η^1:μ^2)(E) (H and I contain the zwitterionic form of the ligand)

We identified a smaller group of 62 structures containing exclusively isonicotinic acid as ligand and a single divalent metal ion (M^{2+}: Mn(II); Fe(II); Co(II); Ni(II), Cu(II), Cd(II)). We also considered structures containing Cu(I). The following table (Tab.3.1) summarizes the occurrence of the different coordination mode for the considered metal cations (CCDC release 2018). HIso/Iso ligand can adopt more than a single coordination mode in the same structure. The ligand is usually deprotonated and negatively charged, then the majority of the structures does not contain any counter-anion. However, we considered also structures where the counter anion is present to balance the charge. SCN^-, N_3^-, CN^- are widely used. Their presence is always crucial also for the structure topology because, like Iso, they are rigid, linear and can act as bidentate ligands[4–7].

	A	**B**	**C**	**D**	**E**	**F**	**G**	**H**	**I**
Mn	1		5	1		1		1	
Fe			1			1			
Co	2	2	7			1		2	
Ni	1	1	1			1	1		
Cu	10		10			2	3	1	
Cd	1	8	3			1		1	
All	*15*	*11*	*27*	*1*	*0*	*7*	*4*	*5*	*0*

Tab.3.1 Occurrence in CSD database (March 2018 release) of structures containing only HINA and a metal cation among Mn(II); Fe(II); Co(II); Ni(II), Cu(II), Cd(II)),

The coordination modes A, B, and C are the most frequent. This reflects the importance of HINA for crystal engineering as a linear connector. Mode C is the most important: it is present in 27 structures over 62. They are implied in the formation of di- or tri- dimensional network that will be later discussed. The monodentate coordination modes (D, F, G, H) are less represented.

All the considered metals can coordinate HIso using mode F, forming a series of isomorphous structures, the triclinic crystals of the coordination compound $[M(Iso)_2(H_2O)_4]$, [8–11] (M = Mn(II); Fe(II); Co(II); Ni(II), Cu(II), Cu(I); Cd(II)). These compounds are obtained when a M(II) salt and HIso are mixed at room temperature, in water or alcohols, using a stoichiometric amounts of the reagents (L:M=2:1). Coordination mode D is observed exclusively in a 3D polymer were Iso adopts both mode D and C [12].

Coordination modes G and H seem to be almost equally represented in the overall count. However, mode G is characteristic of Copper respect to the other metals (3 copper-containing structure over 4), probably due to the well-known affinity between copper atoms and nitrogen-based ligands. Mode G is typical of a class of 1D polymers were the presence of the protonated group plays an important role. These polymers consist of octahedral copper centres bonded by SCN^- or N_3^-, while Hiso ligands occupy two trans positions. Ttrough the classical coupling of the carboxylic groups due to the formation of two strong hydrogen bonds, the 1D polymers connect forming 2D networks that shown excellent sorption properties[5,12]. Mode H is present only in few structure, and it is interesting because it is based on the zwitterionic form of the ligand [3,13–16] . Coordination modes I and E are not adopted in the considered selection of structures.

As previously introduced, hydrogen bonds introduce interesting supramolecular architectures. For example, it leads to the formation of 2D networks able to host aromatic molecules [5], links conductive Cu-Cl 1D chains [17], connects 2D network leading to a robust 3D structure [18].
Considering the metallic centres, most of them adopts the octahedral coordination geometry. Octahedral metallic centres bound by Iso adopting its mode C form the majority of the structure. In these cases, the Iso is a μ^3 bridging ligand. A group of 3D network of composition $[M(Iso)_2]$ (M = Fe(II), Co(II), and Mn(II)) shows a structure formed by square grids of octahedral sites connected by ligand molecules. The grids are staked and connected by the coordination of the carboxylic groups with the metal centres of the upper and lower grids, forming square channels [19–21].
Ni(II) and Co(II) can bind Iso in its coordination mode B. Respect to mode C, using mode B both carboxylic oxygen coordinate the same metal centre. It is characterized by a larger steric hindrance over the metal cation. The metal centre adopts a tetrahedral coordination geometry to host two ligands coordinated in this way [27,28]. The result is a complex 3D network.
Curiously, Cd(II) atom adopts a trigonal bipyramidal coordination geometry, with two ligand molecules bound via their carboxylic groups (coordination mode B) at two equatorial sites. In the third equatorial position there can be a water molecule or a counter anion, while the apical positions are occupied by pyridine groups [22–26].
Copper(II) cation (Cu(II)) is the most used (26 structure over 62). Cu(II) shows a peculiar behaviour. It usually assumes a square pyramidal coordination geometry and the ligand usually adopt both modes C and A. As can be seen from tab.3.1, for copper they have the same occurrence. The most common features of its structures is the formation of 2D grids of composition $[Cu(Iso)_2]$. These grids can stack with or without the formation of coordination bond between carboxylic groups and staked metal centres. However, due the square pyramidal geometry, these 3D structures are not isomorphs with the previously described ones. In these structures Iso adopts both coordination mode C (when bridge cation belonging to different planes) or A [29–31].
The large number of structures revels both the arising interest on this ligand and the high variability in terms of structures and topology that can be obtained from such a simple molecule. The majority of compounds have been obtained by mixing the metal salts and isonicotinic acid using solvothermal condition and water, alcohols or DMF as solvents.
As shown in the previous chapter, slightly different crystallization conditions can lead to the formation of different crystalline phases from the same starting reagents.
The present project is focused on the species obtained by mixing $CuCl_2 \cdot 2H_2O$ salt and HIso at room temperature, using water, THF, DMSO or their mixtures as solvents. In particular, we have used different crystallization techniques (batch crystallization, counterdiffudion/free interface diffusion applied using gelled solutions) to study the effect of the crystallization environment in terms of obtained phases. We focus our attention on the effect of the same parameters (that is the solvent composition, the reagents ratio and the total concentration) on the final products obtained by using different crystallization methods.

Experimental methods

Solution methods

We performed batch crystallization for the evaluation of the phases precipitated from solution.

At first we performed batch crystallization using DMSO as solvent. We used DMSO solutions of Hiso (246.5 mg, 2mmol, 50 mL DMSO, 40 mM) and $CuCl_2 \cdot 2H_2O$ (50.5 mg, 0,3 mmol, 10 mL DMSO, 29.6 mM). The solutions were poured into batches of 24 well PE plates using a micropipette. We followed the order: copper chloride solution, DMSO if necessary, HIso solutions. We considered 4 different crystallization environment, all with the same volume (2mL) and solvent (DMSO). The parameter modified were: the [L]/[M] ratio and the concentration [L]+[M] the following table (Tab.3.2) summarizes the parameter for all the samples. The batches were closed, sealed and kept at room temperature for 6 months. On the same day they were opened and photographed.

DMSO batches	**DMSO_1a**	**DMSO_1b**	**DMSO_2a**	**DMSO_2b**
[L]/[M]	1.3	1.3	2.7	0.7
[M]+[L]	35 mM	17,5 mM	27,5 mM	25 mM

Table 3.2, batch precipitation experiment using DMSO as solvent

In second place we studied phase precipitation from water solutions. We prepared water solutions of $CuCl_2 \cdot 2H_2O$ (1.724g, 10 mmol, 25mL DDW, 404.6 mM) and HINA (1.23g, 10 mmol, 250mL DDW, 40 mM). We poured the solutions into batches of 24 well PE plates using a micropipette. We followed the order: copper chloride solution, water if necessary, HIso solutions. We create a bunch of 47 different crystallization environment, all with the same volume (2mL) and solvent (DDW). We modify [M]/[L] values ranging from 0.25 to 4 (0,25; 0,3; 0,5; 1; 2; 3; 4) and from 10 to 80 mM (10; 20; 30; 40; 50; 60 ; 70 ; 80). Due to low HIso solubility in water, high value of both concentration and reagents ratio cannot be reached. The batches were closed, sealed and kept at room temperature for 6 months. On the same day the wells were opened and photographed. The detailed volumes for any well are reported in the supporting information (Tab.S.3.1)
Finally we perform batch crystallization using water/THF mixtures as solvents. We used the previously prepared water solutions of the reagents adding increasing amount of THF. Hiso is almost insoluble in THF so we cannot reach high amount of THF. The following table summarize the four considered crystallization environment (Tab.3.3).

Water/THF batches	**THF_1**	**THF_2**	**THF_3**
[L]/[M]	0.5	1	2
[M]+[L]	60 mM	40 mM	30 mM
%THF (v/v)	9%	23%	35.5%

Table 3.2, batch precipitation experiment using water/THF as solvent

Using water/THF solutions we also performed classical precipitation experiment considering larger volumes and concentrations. In this case we added a suspension of HIso (10 mL, 80 mM in 1.1 water/THF) to solution of $CuCl_2 \cdot 2H_2O$ (10 mL, 160 mM in 1.1 water/THF). The precipitated powder was filtered, washed with water and dried, then analized using X-ray Powder Diffraction (XRPD).

Gel technique

The counterdiffusion experiments were performed adopting gelled solution. We used silica gel from polymerization of TetraMethylOrthoSilane (TMOS). We prepared the gels adding the appropriate amount of TMOS and water to the solution (TMOS requests the presence of water to gelify). The mixture was stirred at least for 1 hour, then poured and sealed in the selected device (test tube or U-shaped tube). Gelification occurs overnight. Gel concentration is determined by the volume of TMOS respect to overall volume of the solution. We used concentration of TMOS of about 10% or 20% for test tubes and 15% for the U-shaped tubes.

Counterdiffusion in test tube

HIso is insoluble in pure THF. However, the ligand is quite soluble in water (until about 40 mM), and 1:1 water/THF (50% THF) mixtures (until about 25 mM). Layering a THF metal solution on a gelified water solution of HIso, THF triggers the precipitation of Hiso inside the gel media.

We had to calibrate two variables of the experiments: the solvent composition and which reagent (metal salt or ligand) is dissolved in the gelified solution. We considered six different experimental setup: 50%THF solution poured over a gelified water solution (overall %THF = 24%); water solution poured over a gelified 50%THF solution (overall %THF = 24%) and 50%THF solution poured over a gelified 50%THF solution (overall %THF = 50%). For all these cases we adopt two set-ups: pouring the metal solution over the gelled ligand solution (Tab.S.3.2,3) and vice versa (Tab.S.3.4,5). The tubes were closed and sealed and left at rom temperature for 6 months. The detailed parameters for all the samples are reported in the supporting information

Counterdiffusion inside U-shaped tube

We filled a U-shaped with a gelified 50%THF. The two branches of the U-tube were charged using a 100 mM 50%THF solution of $CuCl_2 \cdot 2H_2O$ and a 100 mM suspension of Hiso in 50%THF. The tube was sealed and left undisturbed for 3 months.

Structure solution and refinement

Single crystal X-ray diffraction experiment was performed on a Bruker APEX II CCD area detector diffractometer using MoKα radiation (λ=0.71073 Å). Experiment were performed using ω (0° to 180°) and ϕ (0°, 90°, 180°, 270°) scans. An empirical absorption correction (SADABS or TWINABS) was applied on the collected data.

The structures were solved by direct methods (SHELXS) and refined by full-matrix least-squares on F^2 (SHELXL-97) against ALL data using WINGX interface.

For all the metal ions and ligand atoms the anisotropy of the thermal motion was refined. In any case the data/parameter ratio was kept above 10.

For all the structures hydrogen of the pyridine rings were modelled using a riding model with Uiso=1.2 and fixed C-H distance (0.95 Å). Hydrogens of water molecules were firstly localized using the difference density map and then refined using a riding model (Uiso=1.5) and fixed O-H distance (0.993 Å).

In the case of structure 4, the disorder of a coordinated DMSO molecule was resolved using two isotropic models of the molecule, which position and isotropic thermal motion were refined.

Solvent molecules disorder (structures 2,3,5) were resolved using two isotropic model of the molecules, refining exclusively atom position. Hydrogen atoms positions were modelled and positions and thermal motion were not refined. The most important data regarding the structure solutions and refinements are summarized in table 3.4.

XRPD analysis

Powder X-ray diffraction experiment were performed using a Philips PW 1830 vertical scan diffractometer using CuKα radiation (λ=1.54 Å). For the generation of X-ray we used a 40 mA current at 40 kV voltage.

Table 3.4, structures determination and refinement

Phase	1	2	3	4	5
Formula	$CuC_{12}N_2O_8H_{16}$	$Cu_2C_{18}N_3O_8H_{16}Cl$, C_4H_8O	$CuC_{12}N_2O_5H_{10}$, $C_2H_4O_{0.5}$	$Cu_4C_{40}N_6O_{16}H_{40}Cl_2S$	$CuC_{12}N_2O_5H_{10}$, C_2H_6OS
FW (g/mol)	381.82	636.97	361.81	1249.96	403.89
T(K)	296(2)	120(2)	120(2)	296(2)	296(2)
Crystal system	triclinic	monoclinic	orthorhombic	triclinic	orthorhombic
Space group	P-1	C2/c	Pba2	P-1	Pccn
a (Å)	6.3424(8)	24.454(2)	10.4155(6)	13.1296(4)	17.7448(12)
b (Å)	5.8985(8)	17.6708(16)	14.2297(10)	13.7611(4)	17.7624(12)
c (Å)	9.1876(11)	11.9502(11)	5.6708(14)	15.4614(4)	11.3906(8)
α	99.430(2)°	90°	90°	65.318(1)°	90°
β	105.230(2)°	105.565(2)°	90°	88.354(1)°	90°
γ	108.240(2)°	90°	90°	69.589(1)°	90°
V (Å^3)	354.87(7)	4974.6(8)	840.5(2)	2356.42(12)	3590.2(4)
Z	1	8	2	2	8
μ (mm^{-1})	1.59	1.88	1.33	2.059	1.363
Reflection measured	4313	30640	9134	47745	56823
Independent reflection	2160	8058	2532	17958	6442
R_{int}	1.2%	7.49%	4.04%	4.55%	4.98%
R_1[I>2σ(I)]	2.30%	5.38%	5.15%	4.85%	5.82%
***w*R_2[I>2σ(I)]**	6.80%	15.55%	14.24%	8.27%	12.29%
$\Delta\rho_{min}$ (e Å^{-3})	-0.414	-0.870	-0.908	-1.06	-0.622
$\Delta\rho_{max}$ (e Å^{-3})	0.384	1.000	0.128	1.389	1.665

Results

Identified phases

Tetra-aqua-bis-Iso copper (II) complex [1], $[Cu(Iso)_2(H_2O)_4]$

After 1 hour of stirring, a TMS solution (15% v/v; 1.5 mL TMS; 3.5 mL THF; 5mL H_2O) was poured in a U-shaped glass tube. After gel setting, the branches were filled with 100 mM of water solution of $CuCl_2{\cdot}2H_2O$ and a100 mM water suspension of HIso. The tube was then closed and sealed. After 1 month, light blue, prismatic crystals of this phase were isolated inside the gel near the branch filled with the ligand solution.

The crystal structure of tetra-aqua-bis-Iso copper (II) ([Cu(κ-N,Iso)$_2$(H_2O)$_4$]) has been already reported in the literature (CSD database with refcodes QANRON and XAXFUX). [1–5] There are one entry under QANRON refcode and nine entries under XAXFUX refcode. One without coordinates (06), two without hydrogen atom coordinates (03, 04) and five with full atomic coordinates determined. One determination (07) is at low T (150K), [5] the others are at room temperature. R_1 range from 2.6 to 6.8 %. The structure of this complex will be further analyse in a following chapter dedicated to morphology prediction.

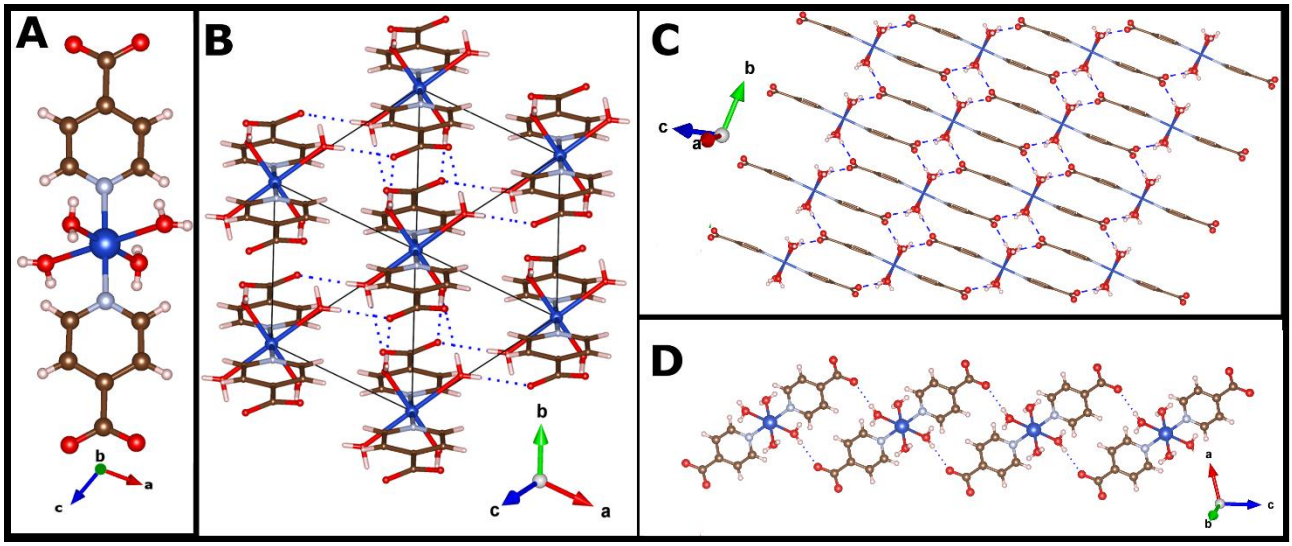

Fig 3.3 A) tetra-aqua-bis-Iso copper (II) complex, B) projection of the unit cell along [111]. C) Hydrogen bond network parallel to ($10\bar{1}$) plane, (D) hydrogen bond ladder along [001], hydrogen bond is represented by blue dotted lines.

The crystal structure of tetra-aqua-bis-isonicotinate copper (II) complex (Fig. 3.3A), shows a distorted octahedral coordination geometry with two N and two O equatorial atoms (from two isonicotinate ligands and two water molecules) and two weak Cu-water axial interactions due to Jahn-Teller distortion. Ligand molecule adopt the coordination mode F (Fig.2) and Cu-N distance is about 2,01Å, while there are two different Cu-O distance: 1.99 Å (equatorial) and 2.45 Å (apical). The crystal space group is $P\bar{1}$. In the structure the copper atoms are located on the cell edges, on an inversion centres (Fig. 3.3B).

The complex has no net charge, but exposes charged groups as the copper cation and deprotonated carboxylic groups. In a separate chapter will be calculated the energy of these interactions. The carboxylic groups and the coordinated water molecules are acceptors and donors of strong hydrogen bonds. Along [101] direction the complexes are related by translations and connected by four hydrogen bonds (O···H, 1.87 Å and 2.16 Å). Along [111], complexes are related by inversion and form two hydrogen bonds (O···H, 1.98 Å). Through this H-bonds form a 2D network parallel to ($10\bar{1}$) plane (Fig. 3.3C). The coordinated water molecules, that display the longest Cu-O bond distance, form a H-bonds chains along [001] direction (O···H, 2.09 Å) (Fig.3.3D). This interactions connect to each other the ($10\bar{1}$) planesleading to theformation of a complex supramolecular 3D network.

2D coordination polymer [$Cu_2(Iso)_3Cl(H_2O)$] · THF [2]

A small amount of $CuCl_2{\cdot}2H_2O$ (44.1 mg, 0.26 mmol) was dissolved in a TMS solution (10% v/v; 0,5 mL TMS; 2 mL THF; 2.5 mL H_2O). The solution was poured in a glass tube after 1 h of stirring. After gel setting (about 3 h), 5 mL of a THF\water (1:1) suspension of HIso (31.5 mg, 0.26 mmol) was layered over the gel. Then, the tube was closed and sealed. After some weeks, dark blue, hexagonal prismatic crystals of this phase were collected at the sol-gel interphase.

The structure of $[Cu(\kappa\text{-}N,\kappa\text{-}O,\eta^1{:}\eta^1{:}\mu^2\text{-}Iso)_3(\mu^2\text{-}Cl)(H_2O)_2]_n{\cdot}THF$ has already been reported in CSD database [6](refcode EYODUT) as a disordered structure, with a R_1 value of 3.53 %. We collected new crystal data, resolve and refine the structure, reaching a value of 5.37 % for R_1 parameter and resolving also the solvent contribution from THF molecules hosted in the channels of the network.

The product consists of a 2D coordination polymer formed by copper(II) chloride and Iso ligand. The space group is C2/c. The asymmetric unit consists of three ligands, a chloride anion, and two copper atoms.

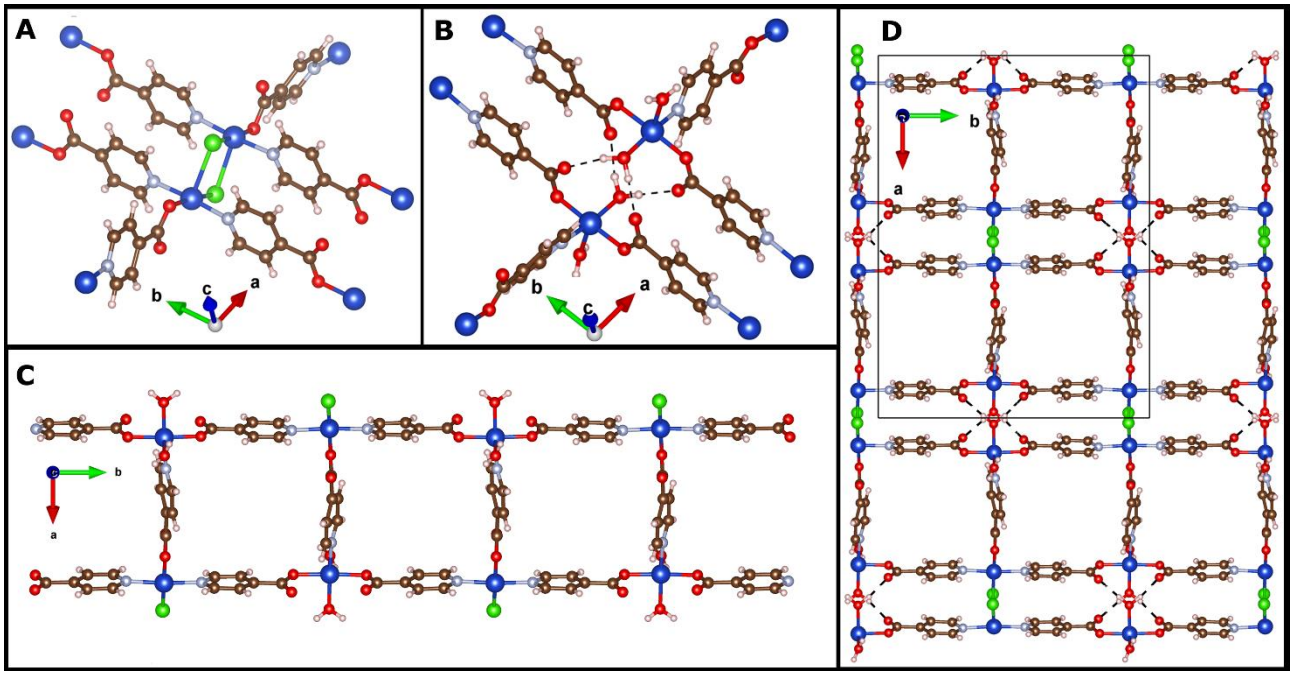

Fig.3.4 2D MOF [$Cu_2(Iso)_3Cl(H_2O)$] · THF structure. Coordination sphere of Cu1(A) and Cu2(B) atoms. C) structure of the ladder formed by alternation along b and a of atoms Cu1 and Cu2; D) structure of the 2D layers, the unit cell is projected along c axis and shown. Dotted lines represent hydrogen bonds.

There are two different metal coordination sites. he geometry around Cu1 atoms (Fig. 3.4A) may be described as a distorted square *pyramid* with the axial and an equatorial positions occupied by the chlorine atoms (Cu-Cl, 2.27 Å and 2.76 Å). The other equatorial positions are occupied by an oxygen atom of a Iso ligand (Cu-O, 1.98 Å) and two nitrogen atoms of other two ligand molecules (in *cis* positions, Cu-N, 2.02 Å).

The coordination geometry of atom Cu2 (Fig. 3.4B) is square pyramidal with two water molecules, displaying different Cu-O bond lengths (Cu-O, 2.21 Å and 1.99 Å), coordinated in the apical and at one of the base positions. In *trans* position respect to the "equatorial" water molecule, an Iso ligand is bound via the nitrogen atom (Cu-N, 2.02 Å). While the other two base positions there are two Iso

ligands bound by the carboxylic groups (Cu-O, 1.94 Å). The first type of copper atoms, Cu1, shares the chloride ions, while the other type, Cu2, shear both the coordinated water molecules.
The ligand coordination is specular for Cu2 and Cu1 because all the Iso molecules are connectors between the two different copper atoms, adopting coordination mode A (Fig.2). The copper atoms and the shared Iso molecules form ladder-like structures along the b axis, (Fig.3.4C), (Cu1-Cu2, 8.92 Å along rails, 8.85 Å along step).
The chlorine bridges between the Cu1 atoms (Cu1-Cu1, 3.56 Å) (Fig. 3.4A) connect the ladders leading to the formation of a bidimensional network parallel to (001) plane characterize by a pattern of alternating square and rectangular meshes. The coordinated water molecules at the base of the pyramid of the Cu2 copper atom generate a further connection between the ladder binding, via H-bond (O···H, 1.83 Å and 1.88 Å), two of oxygen atoms of the carboxylic groups of the facing Cu2 (Cu2-Cu2, 4.93 Å) (Fig.3.4B).
The 2D (001) planes are undulated (Fig. 3.5A). The layers, which are related by a glide plane, *stack* in an offset *ABAB* pattern along the c crystal direction (fig. 5). The staking of the grids creates channels along [001] directions (Fig. 3.5B) that are occupied by THF molecules. After removal of the solvent molecules, the calculated solvent accessible volume (probe radius = 1.2 Å) is about 19% of the total crystal volume.

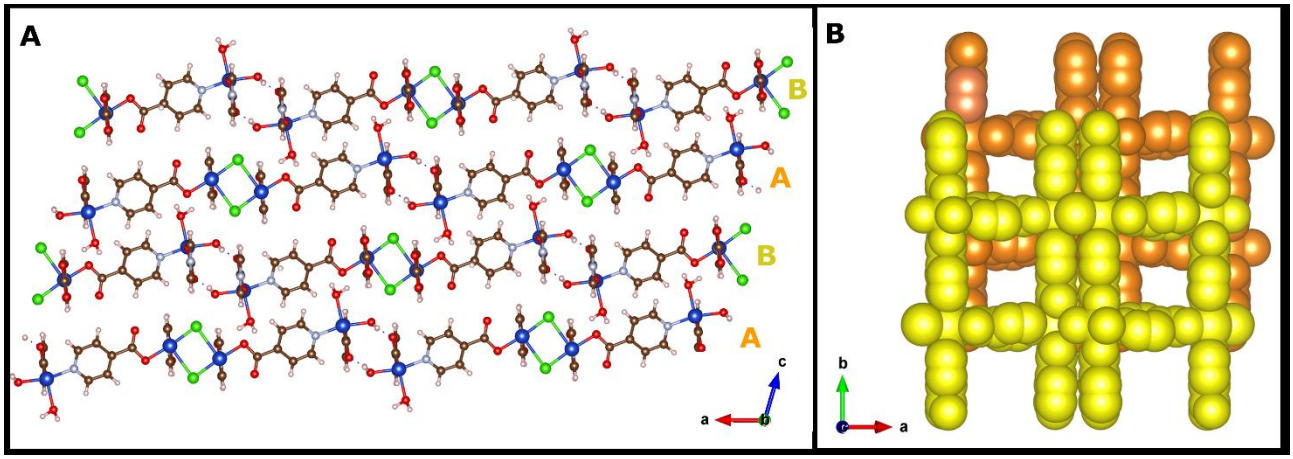

Fig.5 2D MOF [$Cu_2(Iso)_3Cl(H_20)$] · THF structure. (A) Projection along [010] direction; B)projection along 001 directions (for this image planes are characterized by different colours).

2D coordination polymer [$Cu(Iso)_2(H_2O)$] · 0.5 THF [3]

The preparation was similar to that of the product **2**. CuF_2 salt (37.8 mg, 0.37 mmol) was dissolved in a TMS solution (10% v/v; 0.5 mL TMS; 2 mL THF; 2.5mL H_2O). The solution was poured in a glass tube after 1 h of stirring. After gel setting (c.a. 3h), 5 mL of a THF suspension of HIso (30.5 mg, 0.24 mmol) was layered over the gel. The tube was then closed and sealed. After some weeks, blue prismatic crystals formed at the sol-gel interphase.
Crystals correspond to the compound $[Cu(\kappa\text{-}N,\kappa\text{-}O,\eta^1{:}\eta^1{:}\mu^2\text{-}Iso)_2(H_2O)]_n{\cdot}0.5n$ THF and consists of two-dimensional four connected layers. The space group is Pba2. The asymmetric unit consists of a copper atom, two Iso ligands and a water molecule.

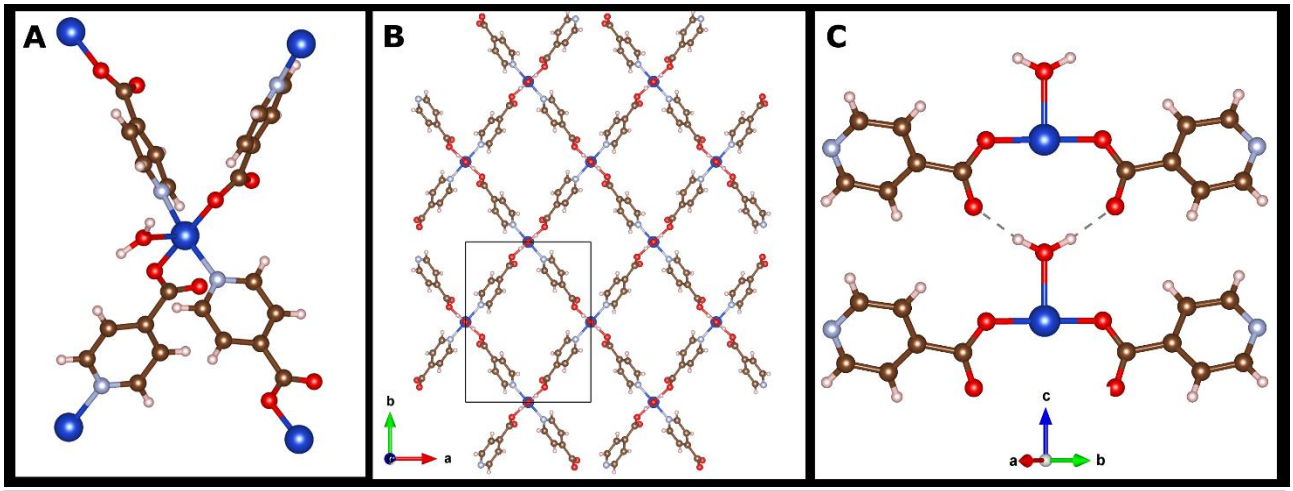

Fig.3.6 2D MOF [Cu(Iso)$_2$(H$_2$O)] · 0.5 THF *structure. (A) A single copper node, (B) structure projected along [001] direction showing the rhombic grid, (C) interaction through hydrogen bond between staked copper atoms*

Copper atoms display a square-pyramidal coordination geometry. Ligand molecules occupy the equatorial plane. Two, in *trans* positions, bound by the nitrogen atoms (Cu-N, 2.00 Å), the other two by an oxygen atom of the carboxylate groups (Cu-O, 1.96 Å). A water molecule is coordinated at the apical position of the pyramid (Cu-O, 2.14 Å) (Fig. 3.6A).

All the ligands display coordination mode A. They act as spacers between copper atoms (Cu-Cu distance 8.82 Å) leading to the formation of infinite two-diemsional layers of rhombic meshes (Fig. 3.6B).

The 2D polymer sheets are stacked along the [001] direction in a AA sequence (Cu-Cu, 5.67 Å). The superposition of the planes lead to the formation of 1D parallel channels that are filled with THF solvent molecules. All the coordinated water molecule pointing in the same direction, that is along the c axis, forming strong H-bonds with the non-coordinated oxygen atoms of the carboxylate groups of the upper layer (O···H, 1.75 Å) (Fig. 3.6C) leading the formation of a 3D network. After removal of the solvent molecule, solvent accessible volume (probe radius = 1.2Å) is about 20% of the total crystal volume.

2D coordination polymer [Cu$_4$(Iso)$_6$Cl$_2$(H$_2$O)(DMSO)] [4]

The product was obtained by batch crystallization: $CuCl_2 \cdot 2H_2O$ (5.05mg, 0.03 mmol) and HIso (4.93 mg; 0.04 mmol) were dissolved in 2 mL of DMSO in a well of a 24-well plate . The well was then sealed with a cover slide to prevent the evaporation. After several weeks, the formation of light blue elongated hexagonal platelets was observed at the bottom of the well.

The product consists of a 2D network having formula $[Cu(\kappa\text{-}N,\kappa\text{-}O,\eta^1{:}\eta^1{:}\mu^2\text{-}Iso)_6(\mu^2\text{-}Cl)_2\ (\kappa\text{-}O,DMSO)_2(H_2O)_2]_n \cdot THF$] The space group is $P\bar{1}$ and the asymmetric unit contains four copper atoms, six ligands, two chloride atoms, two water molecules and two DMSO molecules. The structure of this phase shows strong similarity to those of phase **2**.

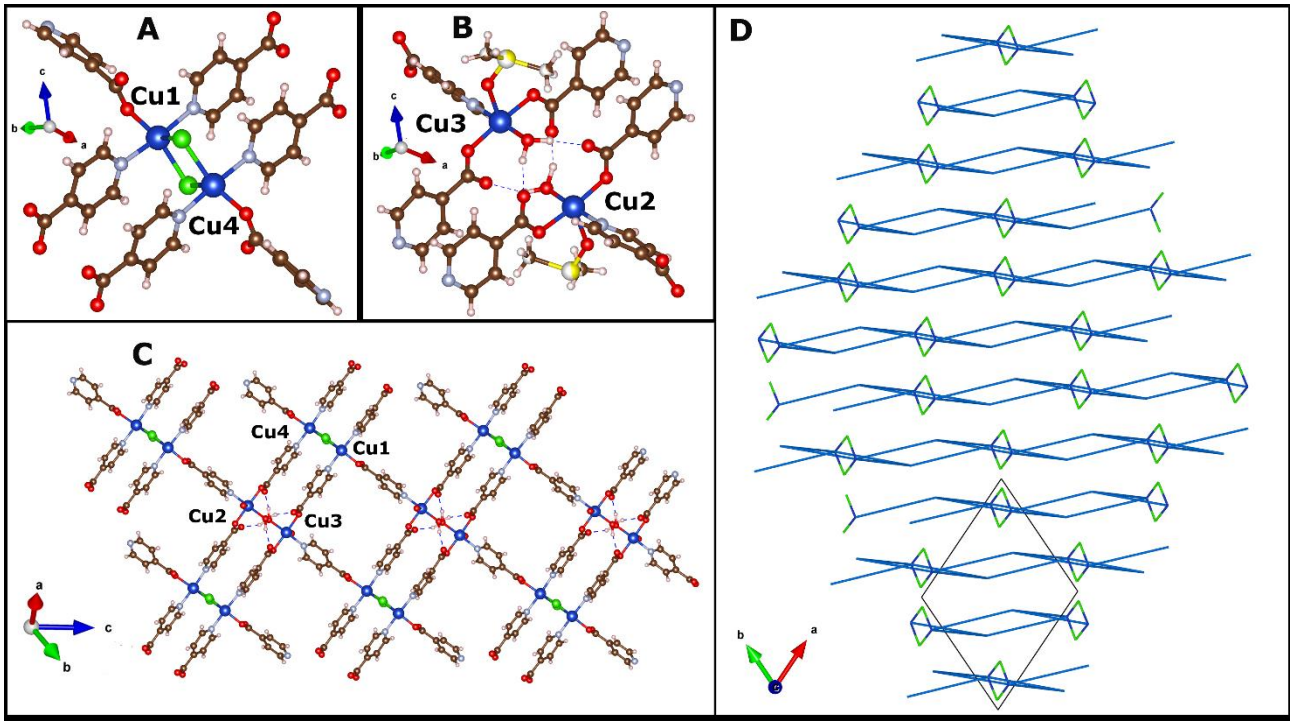

Fig.3.7 2D MOF [$Cu_4(INA)_6Cl_2(H_2O)(DMSO)$] structure. Coordination sphere of Cu1 and Cu4 (A), Cu2 and Cu3(B) atoms. C) structure of the 2D layers dotted lines represent hydrogen bonds. D) Staking of the planes along [110]*. Only copper and chloride atoms are showed, ligand molecule are represented as blue straight lines, DMSO molecules are not showed.*

There are four independent copper atoms showing two different coordination environments. The coordination geometry around Cu1 and Cu4 atoms (Fig. 3.7A) is trigonal bipyramidal, with two equatorial positions occupied by two chlorine atoms (Cu-Cl, 2.41 Å and 2.59 Å). An oxygen atom of an Iso ligand occupies the third equatorial position (Cu-O, 1.97 Å). Two nitrogen atoms of other two ligands molecules occupy the apex positions (Cu-N, 2.00 Å). The geometry is highly distorted (angles Cl-Cu-Cl, 91.6°, O-Cu-Cl 133.8° and 134.5°).

The coordination geometry of atoms Cu2 and Cu3 is square pyramidal (Fig. 3.7B). A water molecule and three ligands occupy the base positions. The water molecule (Cu-O, 1.96 Å) is in *trans* position respect to an Iso ligand bound via nitrogen atom (Cu-N, 1.99 Å). Two Iso ligands bound by the carboxylic groups (Cu-O, 1.96 Å) occupy the remaining positions. A disordered DMSO molecule, bound via oxygen atom, occupies the apical position (Cu-O, 2.31 Å).

All the ligand molecules act as connectors between the copper atoms, adopting the coordination mode A (Fig.3.2). Iso ligands connect Cu1 and Cu3 and Cu2 and Cu4 forming a series of parallel chains. Iso ligands connect also Cu1 to Cu2 and Cu3 to Cu4 metal centres leading to the formation of ladder-like structures that run parallel to [$1\bar{1}1$] direction (Fig.3.7C).

Moreover, chlorine atoms bridge Cu1 with Cu4 (Cu1-Cu4, 3.48 Å) (Fig.3.7A), while the water molecule bound to Cu2 forming hydrogen bonds with the oxygen atom of the carboxylic groups bound to Cu3 (Fig.7B) connect the Cu2 and Cu3 centres (Cu2-Cu3, 4.91 Å). These connections between the ladders lead the formation of a bidimensional network parallel to plane (110) (Fig.3.7C). These planes are characterized by a pattern made of the previously described square (Cu1-Cu2-Cu4-

Cu3) and of rectangular (Cu1-Cu3-Cu1-Cu4-Cu2-Cu4) meshes (Fig.3.7C). The following table (Tab.3.5) summarizes the Cu-Cu distance along these planes.

	Cu2		Cu3	
Cu1	8.83 Å		8.93 Å	8.91 Å
Cu4	8.94 Å	8.92 Å	8.78 Å	

Tab.3.5 2D MOF [$Cu_4(INA)_6Cl_2(H_2O)(DMSO)$] Distances between metal centres connected by Iso

The 2D (110) planes are undulated (Fig.3.7D) and *stack* in an offset *AABB* pattern along the [110] direction (fig.4). The coordinated DMSO molecules fill the square holes of the staked planes.
The 2D planes are equivalent to the ones formed by the phase **2** (Fig.3.3D, for comparison). The main difference is the coordination of a DMSO molecule instead of a water molecule. The bulkiness of DMSO avoids the superposition of the square meshes and the formation of the channels.

2D coordination polymer [Cu (Iso)$_2$)] · 0.5 DMSO [5]

The product was obtained by batch crystallization: $CuCl_2 \cdot 2H_2O$ (2.5mg, 0.015 mmol) and HIso (4.9mg; 0.04 mmol) were dissolved in 2 mL of DMSO in a well of a 24-well plate. The well was then sealed with a cover slide to prevent the evaporation. After several weeks, the formation of blue square platelets and prisms was observed at the bottom of the well.
The product consists of a 2D network having formula $[Cu(\kappa\text{-}N,\kappa\text{-}O,\eta^1{:}\eta^1{:}\mu^2\text{-}Iso)_2(H_2O)]_n \cdot DMSO$ The space group is Pccn (SG n° 56) and the asymmetric unit contains one copper atom, two Iso molecules, a molecule of water and a molecule of DMSO.

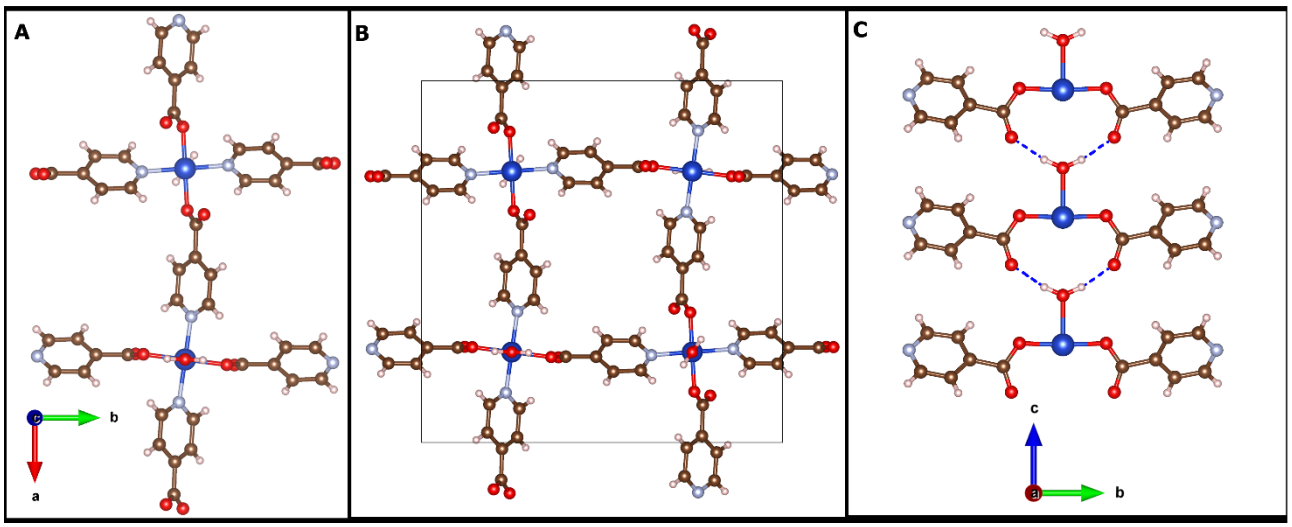

Fig.3.8 2D MOF [Cu(Iso)$_2$)] · 0.5 DMSO structure. (A) copper nodes; (B) structure projected along [$\bar{1}$10] direction showing a single square grid; (C) copper atoms staked along [001] direction (hydrogen bonds are drawn with blue dotted lines)

The coordination geometry is square pyramidal. Ligands in *trans* positions bound the copper atom via the same donor group, that is nitrogen atom (Cu-N, 2.02 Å), and an oxygen atom of the carboxylate group (Cu-O, 1.95 Å). A water molecule occupies the apical position of the pyramid (Cu-O, 2.21 Å).

The Iso molecule acts as bidentate ligands to link two copper atoms (coordination mode A, Fig.3.2). The metal centres show the same coordination environment but a different orientation respect to the [1 0 0] and [0 1 0] axis (Fig.3.8A). Copper atoms are the nodes of the network and Iso ions the connectors of an infinite 2D square mesh (Cu-Cu, 8.92 Å) (Fig.3.8B). The 2D layers are superimposed along the [0 0 1] direction with an ABAB sequence, (Cu-Cu distances, 5,69 Å). The holes of the grids superimpose forming channels parallel to [0 0 1] that host the DMSO molecules. After removal of the solvent molecule, solvent accessible volume (probe radius = 1.2Å) is 20% of the total crystal volume.
The coordinated water molecules form hydrogen bonds with the non-coordinated oxygen atoms of the carboxylic groups of the Iso ligands of the nearest plane (O···H, 1,81 Å) (Fig.3.8C).
The structure shows strong similarity with MOF phase **3**. There are two main differences: phase **3** is acentric, with all the water molecule point in the same direction; its channels are narrower and host THF instead of DMSO.

Behaviour in Solution

We perform a fast screening of the phases that precipitate from solution. We focus our study on the effects related to the overall concentration ([L]+[M]) and reagent ratio ([L]/[M]) and the solvent composition. HIso shows a very low solubility in DMSO and water (c.a. 40 mM), and it is almost insoluble in all the most common organic solvents as THF. 50%THF solution can dissolves HIso (until a concentration of c.a. 25 mM). Instead, $CuCl_2 \cdot 2H_2O$ salt is soluble in DMSO, water and THF. We usually worked considering clear solutions, so water or DMSO must be present in all the samples to solubilize HIso. We have also considered water\THF solutions characterized by an increasing % of THF.

DMSO

We have considered four conditions: 1) ([DMSO_1a and DMSO_1b), we considered a) high and b) low total concentration at a fixed reagent ratio; 2) ([DMSO_2a and DMSO_2b), a) high and b) low ratio at a fixed overall concentration. We have isolated crystals from all the samples. Phase identification were performed by using XRD.
In the first two samples we obtain a mixture of phase **4** and phase **5**, observing a predominance of phase **4** crystals. Increasing ligand amount (DMSO_2a), we obtained exclusively crystals of phase **4**. Instead, increasing metal salt concentration (DMSO_2b) we observe precipitation of exclusively phase **5**.

Water and THF

We performed a large number of experiments in water solution, by varying the total ligand-metal concentration ([L]+[M]) (from 10 mM to 80mM) and the reagents ratio ([L]/[M]) (from 0,25 to 4). In all trials, we have isolated the crystals of the phase **1**, on which we focused to study its peculiar habits experimentally observed (see chapther 4). Due to the insolubility of HIso in THF, we performed a single experiment dissolving metal salt in THF and adding a suspension of HIso (overall [L]+[M]=30mM, [L]/[M]=0.5). During the stirring of the suspension we observed the precipitation of a dark blue powder. Using XRPD (supporting information, S.3.6) we have identified this phase as phase **2**, which was recently reported in literature[1]. In the original paper, this phase has been synthetized by refluxing HIso with a small excess of $CuCl_2 \cdot 6H_2O$ and NaN_3 in a water/MeOH

solution. Both phases **1** and **2** are stable outside their solutions. We have never observed co-precipitation of the two phases from solution.

Gel technique

TMOS requires a minimum amount of water in order to gelify, so we did not perform counterdiffusion experiments using pure DMSO or pure THF solutions.
Adopting gel techniques, we were able to isolate crystalline phases from almost every sample. Phase recognition was performed firstly from crystal habit, and then confirmed by using XRD analysis of selected crystals.

Test tubes

HIso has a low solubility and must to be solubilized in presence of water. Due to this limitation, we started considering systems where HIso (25 mM) was dissolved in water and gelled with TMOS.
At first, we studied the effect of the solvent composition. We considered equal amount of the reagents ([L]/[M]=1) and a fixed overall concentration ([L]+[M] = 25mM), using 25mM solutions of the of copper chloride (25mM) layered over a water gelled gelled solution of the ligand (25 mM). We have considered the three different conditions previously described for crystallization in solution. By layering the water solution of the metal salt over the 50%THF gelled solution of the ligand we have observed the formation of the phase **1** (Fig.3.9A). Layering 50%THF (metal salt) solution over a gelled water solution (of the ligand), we observed the formation of two phases. Phase **1,** over the gel, in solution and the phase **3** inside the gel (Fig.3.9B). Instead, by using exclusively a 50%THF mixture for both components (Metal-solution, gelled Ligand solution), we have isolated in the gel media the phase **3** (Fig.3.9C).
Subsequently, we have increased the concentration of the metal solution from 25 mM to 50 mM. In this way we have increased the total concentration (37,5 mM) and decreased the ratio ([L]/[M]=0,5). We consider the same combinations of solvents (see above). For the first two samples, the results are the same: phase **1** (Fig.3.9D), phase **1** and phase **3** (phase **1** over the gel, phase **3** inside the gel (Fig.3.9E). In a third case, we have obtained crystals of phase **2** at the interphase and phase **3** inside the gel (Fig.3.9F).

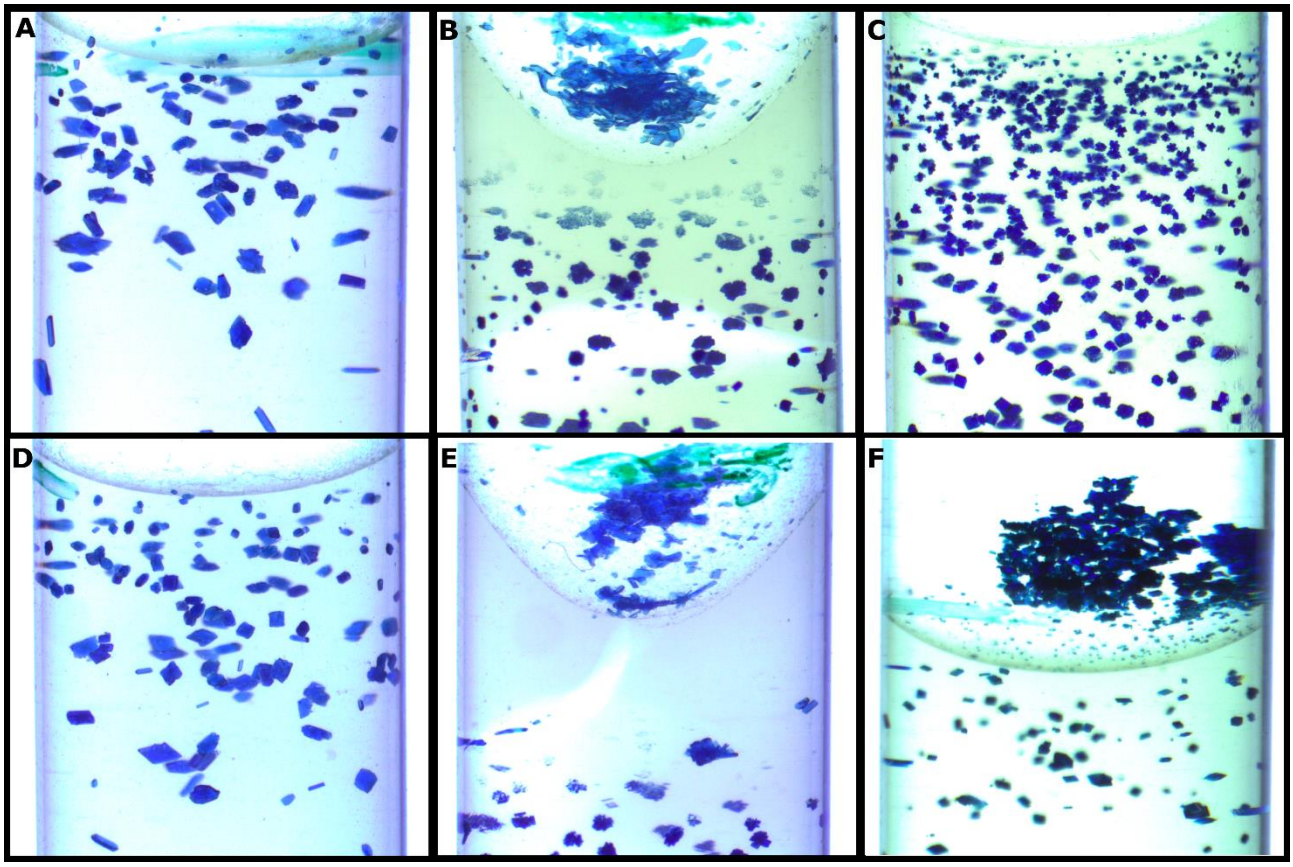

Fig.3.9. Metal salt solution layered over gelled (10% v/v) ligand solution. HIso 25mM in water, $CuCl_2 \cdot 2H_2O$ 25mM (A) and 50mM (D) in 50%THF. B) HINA 25mM in 50%THF, $CuCl_2 \cdot 2H_2O$ 25mM (B) 50mM (E) in water. HIso 25mM in 50%THF, $CuCl_2 \cdot 2H_2O$ 25mM (C) and 50mM (F) in 50%THF.

We have repeated the last experiments increasing the concentration of TMOS from 10% v/v to 20% v/v. As expected, we have observed the formation of the two phases **1** and **2**, but phase **2** this time was observed also inside gel. The transition between the two phases is very clear and we can see that where the oversaturation of phase **2** is very low (high quantity of ligand) phase **3** is insoluble and precipitates as small crystals. Once more, counterdiffusion experiments performed inside gel media as revealed the ability to create multiple crystallization conditions inside the same tube.

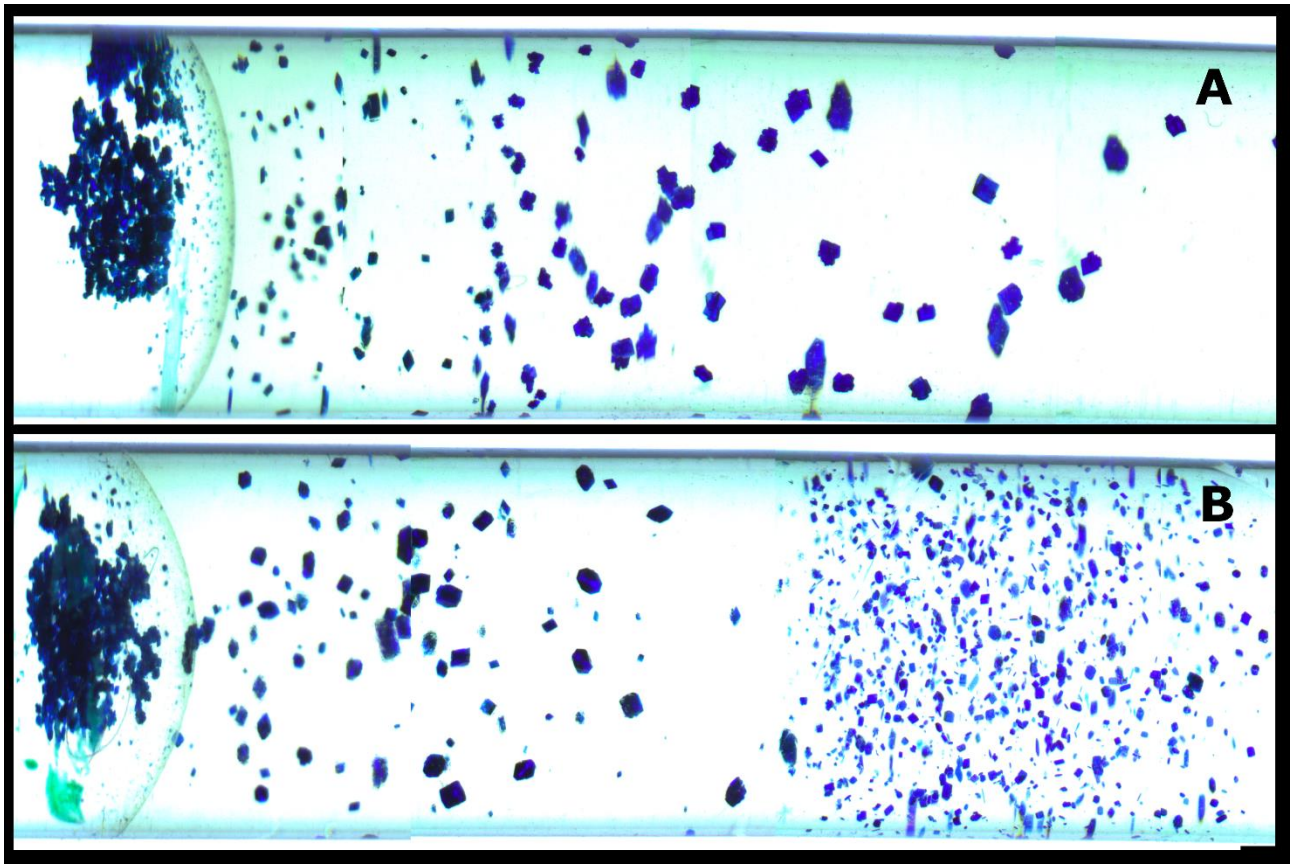

Figure.3.10. Metal salt solution layered over gelled ligand solution, HIso 25mM in 50%THF, $CuCl_2 \cdot 2H_2O$ 25mM in 50%THF solution.TMOS 10% v/v (A) and 20% v/v.

The third considered solvent composition (Fig.3.9C and F) is symmetric (for both gel and solution we used a mixture 50%THF), so we considers also their inversion, that is, ligand solution (25 mM) poured over a metal gelled solution (25 and 50 mM). In these cases, we have never observed the coexistence of phases **2** and **3**. For [L]/[M]=1 we have observed the formation of the phase **3** alone(Fig.3.11A), while for [L]/[M]=0,5 we have observed exclusively the formation of the phase **2** at the interphase (Fig.3.11B).

The last configuration considered in a test-tube was formed by a THF suspension of HIso layered over a water/THF gelled solution of the metal salt (50mM). We have obtained only aggregates of the phase **2** inside the gel. In this case we have observed a modification of the habit of phase **2** from the usual hexagonal prism to elongated hexagonal platelets (Fig.3.11C).

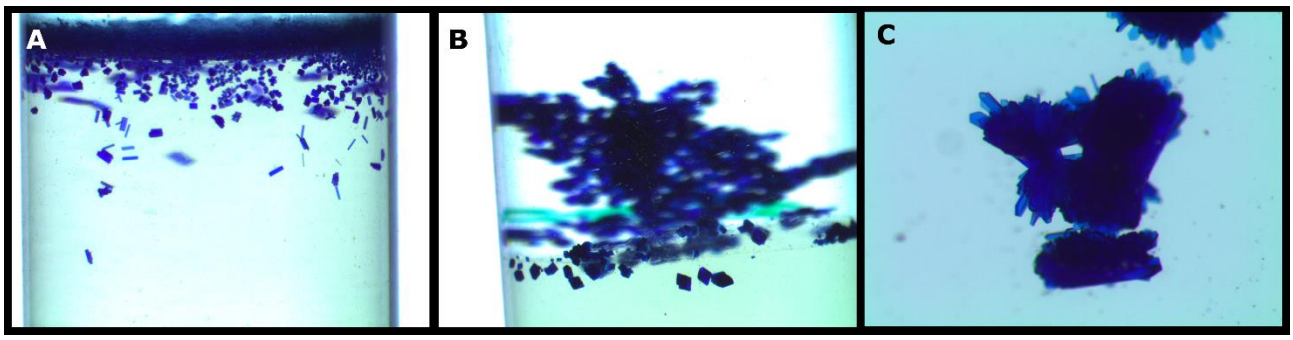

Figure.3.11 Ligand solution layered over gelled (10% v/v) metal salt solution. A) $CuCl_2 \cdot 2H_2O$ 25mM in 50%THF, HINA 25mM in 50%THF. B)) $CuCl_2 \cdot 2H_2O$ 50mM in 50%THF, HINA 25mM in 50%THF. C) $CuCl_2 \cdot 2H_2O$ 50mM in 50%THF, HINA 25mM (suspension) in THF.

U-shaped tubes

The U-shaped tube was filled using a gelled water/THF (50%THF) solution, while its branches were filled with equimolar water solutions of HIso and copper chloride. After 3 months, we observed the formation of two types of crystals and identified two phases (Fig.3.12). Right below the branch charged with Hiso solution, we observed the formation of large crystals of the phase **1** . Very near to this branch, in the horizontal part of the tube, we observed the formation of phase **3** crystals. In this case, we have never isolated all the three phases inside the same U-shaped tube.

Figure.3.12 Counterdiffusion experiment inside U-shaped tube, the photo show the half tube near the branch chargd with ligand (50mM) water solution. The other branch was filled by $CuCl_2 \cdot 2H_2O$ (50mM) water solution. The tube was filled with a gelled TMS (15% v/v) solution in 50%THF.

Discussion

By using three common solvents, working at room temperature, we were able to obtain five different coordination compounds, two new 2D-networks from DMSO solutions (**4** and **5**) and three 2D-networks from water/THF (50%THF) solutions (**1**,**2**,**3**). Three compounds (**3**, **4** and **5**) are new and correspond to 2D coordination networks, two are yet reported in the literature but one of them was obtained using solvothermal conditions. This confirm that the same metal / ligand couple can create a large number of coordination polymer phases, showing different dimensionalities and topologies in the obtained networks.

Secondly, we observed how the variation of crystallization parameters as reagent ratio and solvent composition, can have a deep influence on the obtained network.

In the case of precipitation from pure DMSO solvent, the variation of the [L]/[M] parameter has been enough to drive the crystallization process. High ligand amount induce the precipitation of phase **4**, while high metal concentrations are related with the precipitation of phase **5**. Interestingly, the ratio between ligand and metal in the formula unit (1.5 for phase **4** and 2 for phase **5**) correlates with the precipitation of, for example, ligand-richer phase (**5**) from ligand-rich solution.

The copper atom shows an unusual trigonal bipiramidal coordination geometry in phase **4**, respect to more common square pyramidal geometry.

From pure water solution we have observed the exclusive precipitation of the phase **1**. On the other hand by using a THF (100%) suspension of the reagents we have isolated the phase **2** that is a new 2D coordination polymer.
from water/THF mixtures we observed no modification of the precipitated phases for amount of THF in the mixture below 30%. In this case, the solvent composition results to be crucial respect to the reagents ratio.
The application of counterdiffusion method adopting gelled solutions shed light on the behaviour of the system. As was seen in solution, water solvent induces the formation of the phase **1** only. Interestingly, this phase forms crystals inside gel only if the ligand is trapped inside gel (that is, layering a water or water/THF metal solution over a gelled water solution of the ligand), suggesting that an high value of [L]/[M] ratio is required for the formation of phase **1**
In presence of THF inside the gel, other phases have been isolated. from a % of THF of about 25% (of the overall volume of the tube), the phase **1** crystallizes at the sol-gel interface while in the gel crystallizes the phase **3.** it is important to note that phase **3** has been isolated only by using gel and has never been found in solution The crystals of this phase are unstable outside gel. For a higher amount of THF (%THF = 50%) phase **1** completely disappears. In this case (50% water, 50% THF), we observed the formation of the phase **3** alone, if the tube contains an equal amount of the reagents, while phase **2** precipitates from the solution in presence of an excess of the metal in the solution.
This means that low value of [L]/[M] parameter is as crucial as a THF-rich environment to isolate phase **2**. Considering phase **2** and **3,** their occurrence seems to be related with with the [L]/[M] ratio in the solution. As in DMSO system, this behaviour reflects the formula unit composition (L/M phase **2,** 1.5; L/M phase **3,** 2). To confirm this observation, inside a single test tube (Fig.3.10) we have obtained both phases, phase **2** in the metal rich solution and phase **3** in the ligand rich gelled solution. The inversion of the configuration, that is layering the ligand solution over a gelled metal solution does not produce any changes in the crystallization behaviour. For equal amount of the reagents, phase **3** forms inside the metal rich gelled solution but only at the interphase, while it was previously observed at the bottom of the tubes, and phase **2** cannot forms inside the ligand rich solution. Instead, if we work at higher metal salt concentration phase **2** precipitates at the interphase as well formed crystals, while phase **3** doesn't form, maybe due to its instability outside gel media.
Inside the U-shape tube (50% water-50% THF, see above), we have observed the precipitation of the phase **1** and phase **3**, both near the ligand charged branch, confirming that both phases request the presence of higher amount of ligand respect to metal salt. Phase **2** hasn't been precipitated, negating the opportunity to see all the three phases in the same tube.
Phase **2** shows a topology of the 2D planes that is peculiar for copper atom and similar to the topology of the phase **4** planes. Both these phases were obtained working with excess of metal salt. Similarly, working with high excess of ligand we obtained phase **3** and **5.** In addition, these phases shows the same topology of the 2D planes and the same metal centre coordination geometry. Both phases **3** and **5** are unstable outside their mother liquor. This fact suggest us that there is some correlation between the reagent ratio, the solvent composition and the coordination geometry obtained. Interestingly, the stable phases shows uncommon copper coordination geometries, while the unstable phase shows the more common square pyramidal geometry.

Conclusions

Cu(II)/Iso is an already extensively studied systems, and different techniques have been already applied in order to obtain different network from this metal-ligand couple. This project shows that the process leading to formation of such system are still little known. In fact, carefully design of precipitation conditions has led to the identification of a bunch of new 2D network at mild reaction conditions (room temperature and pressure, common solvents).

Counterdiffusion inside gel media creates multiple crystallization conditions is a single samples. This project shows that gel methods are important tools in order to shed light on the complex crystallization phenomena. In particular gel media let us to identify proper crystallization conditions and to point out the crucial parameters that lead the process towards precipitation of certain phases (reagent ratio and solvent composition). In the studied case, a relatively simple application (counterdiffusion inside test tube) has revealed to be extremely meaningful.

There is an intriguing difference between Cd/bpp system and Cu/Hiso system. In the latter case the gel media (silica gel) let us to identify a completely new phase, never observed in solution (phase **3**). The phase is extremely labile outside gel media, but is stabilized by the presence of the gel media itself. If stabilization arise from a slowing of the degradation process or by an effective stabilization of the new phase is still unclear.

Supporting information

Tab.S.3.1, batch crystallization in water solution

plate	line	column	V(M) (mL)	V(L) (mL)	[M] (mM)	[L] (mM)	[M]+[L] (mM)	[L]/[M]
I	A	1	0.04	0.10	8.1	2.0	10.1	0.2
I	A	2	0.03	0.17	6.7	3.3	10.0	0.5
I	A	3	0.03	0.25	5.1	5.0	10.1	1.0
I	A	4	0.02	0.33	3.4	6.7	10.0	2.0
I	A	5	0.01	0.38	2.5	7.5	10.0	3.0
I	A	6	0.01	0.40	2.0	8.0	10.0	4.0
I	B	1	0.08	0.20	16.2	4.0	20.2	0.2
I	B	2	0.07	0.33	13.5	6.7	20.2	0.5
I	B	3	0.05	0.50	10.1	10.0	20.1	1.0
I	B	4	0.03	0.67	6.7	13.3	20.1	2.0
I	B	5	0.03	0.75	5.1	15.0	20.1	3.0
I	B	6	0.02	0.80	4.0	16.0	20.0	4.0
I	C	1	0.12	0.30	24.3	6.0	30.3	0.2
I	C	2	0.10	0.50	20.2	10.0	30.2	0.5
I	C	3	0.08	0.75	15.2	15.0	30.2	1.0
I	C	4	0.05	1.00	10.1	20.0	30.1	2.0
I	C	5	0.04	1.13	7.6	22.5	30.1	3.0
I	C	6	0.03	1.20	6.1	24.0	30.1	4.0
I	D	1	0.16	0.40	32.4	8.0	40.4	0.2
I	D	2	0.13	0.67	27.0	13.3	40.3	0.5
I	D	3	0.10	1.00	20.2	20.0	40.2	1.0
I	D	4	0.07	1.33	13.5	26.7	40.2	2.0
I	D	5	0.05	1.50	10.1	30.0	40.1	3.0
I	D	6	0.04	1.60	8.1	32.0	40.1	4.0
II	A	1	0.20	0.50	40.5	10.0	50.5	0.2
II	A	2	0.17	0.83	33.7	16.7	50.4	0.5
II	A	3	0.13	1.25	25.3	25.0	50.3	1.0
II	A	4	0.08	1.67	16.9	33.3	50.2	2.0
II	A	5	0.06	1.88	12.6	37.5	50.1	3.0
II	A	6	0.04	0.13	7.6	2.5	10.1	0.3
II	B	1	0.24	0.60	48.6	12.0	60.6	0.2
II	B	2	0.20	1.00	40.5	20.0	60.5	0.5
II	B	3	0.15	1.50	30.3	30.0	60.3	1.0
II	B	4	0.10	1.90	20.2	38.0	58.2	1.9
II	B	5	0.19	0.63	37.9	12.5	50.4	0.3
II	B	6	0.08	0.25	15.2	5.0	20.2	0.3
II	C	1	0.28	0.70	56.6	14.0	70.6	0.2
II	C	2	0.23	1.17	47.2	23.3	70.5	0.5
II	C	3	0.18	1.75	35.4	35.0	70.4	1.0
II	C	4	\	\	\	\	\	\
II	C	5	0.23	0.75	45.5	15.0	60.5	0.3
II	C	6	0.11	0.38	22.8	7.5	30.3	0.3
II	D	1	0.32	0.80	64.7	16.0	80.7	0.2
II	D	2	0.27	1.33	53.9	26.7	80.6	0.5
II	D	3	0.20	1.80	40.5	36.0	76.5	0.9
II	D	4	0.30	1.00	60.7	20.0	80.7	0.3
II	D	5	0.26	0.88	53.1	17.5	70.6	0.3
II	D	6	0.15	0.50	30.3	10.0	40.3	0.3

Tab.S.3.2, counterdiffusion crystallization, metal solution layered over ligand gelled solution

code	[L] (mM)	solvent	%TMOS	[M] (mM)	solvent	[L]+[M] (mM)	[L]/[M]	%THF	phases solution	gel
Cu4nick4	25.0	H_2O	20%	25.0	H_2O	25.0	1.0	0%	\	1
Cu4nick10	27.2	H_2O	10%	27.6	50%THF	27.4	1.0	24%	\	1
Cu4nick16	25.3	H_2O	20%	27.6	50%THF	26.4	0.9	24%	\	1
Cu4nick9	27.2	H_2O	10%	50.8	50%THF	39.0	0.5	24%	\	1
Cu4nick15	25.3	H_2O	20%	50.8	50%THF	38.0	0.5	24%	\	1
Cu4nick13	26.5	50%THF	10%	25.0	H_2O	25.8	1.1	24%	1	3
Cu4nick19	26.7	50%THF	20%	28.8	H_2O	27.7	0.9	24%	1	3
Cu4nick11	26.5	50%THF	10%	50.0	H_2O	38.3	0.5	24%	1	3
Cu4nick17	26.7	50%THF	20%	53.6	H_2O	40.1	0.5	24%	1	3
Cu4nick14	26.5	50%THF	10%	25.0	50%THF	25.8	1.1	50%		3
Cu4nick20	26.7	50%THF	20%	29.0	50%THF	27.8	0.9	50%		3
Cu4nick12	26.5	50%THF	10%	50.0	50%THF	38.3	0.5	50%	2	3
Cu4nick18	26.7	50%THF	20%	54.7	50%THF	40.7	0.5	50%	2	3
Cu4nick23	24.4	50%THF	10%	26.4	THF	25.4	0.9	50%	*	*
Cu4nick24	26.9	50%THF	20%	26.4	THF	26.6	1.0	50%		2 e 3
Cu4nick21	24.4	50%THF	10%	52.7	THF	38.6	0.5	50%		2 e 3
Cu4nick22	26.9	50%THF	20%	52.7	THF 3	9.8	0.5	50%		2 e 3

Tab.S.3.3, counterdiffusion crystallization, metal solution layered over ligand gelled solution

code	L (mg)	solvent	V (gel) (mL)	V (TMOS) (mL)	%gel (mM)	[L]	M	X	MX2 (mg)	solvente	V (mL)
Cu4nick1	16,2	50%THF	5	0.5	10	26,3	Cu(II)	Br	28,5	50%THF	5
Cu4nick2	17,3	50%THF	5	1	20	28,1	Cu(II)	Br	28,5	50%THF	5
Cu4nick3	596,3	H_2O	120	24	20	40,4	Cu(II)	F	15,3	H_2O	5
Cu4Nick4	596,3	H_2O	120	24	20	40,4	Cu(II)	Cl	24,4	H_2O	5
Cu4Nick5	596,3	H_2O	120	24	20	40,4	Cu(II)	Br	35,2	H_2O	5
Cu4Nick6	596,3	H_2O	120	24	20	40,4	Cu(II)	NO3	37,7	H_2O	5
Cu4nick7	25,8	50%THF	10	2	20	21,0	Cu(II)	Cl	42	50%THF	10
Cu4nick8	25,8	50%THF	10	2	20	21,0	Cu(II)	Br	56	50%THF	10
Cu4nick9	33,5	H_2O	10	1	10	27,2	Cu(II)	Cl	86,6	50%THF	10
Cu4nick10	33,5	H_2O	10	1	10	27,2	Cu(II)	Cl	47,1	50%THF	10
Cu4nick11	65,3	50%THF	20	2	10	26,5	Cu(II)	Cl		H_2O	
Cu4nick12	65,3	50%THF	20	2	10	26,5	Cu(II)	Cl		50%THF	
Cu4nick13	65,3	50%THF	20	2	10	26,5	Cu(II)	Cl		H_2O	
Cu4nick14	65,3	50%THF	20	2	10	26,5	Cu(II)	Cl		50%THF	
Cu4nick15	31,1	H_2O	10	2	20	25,3	Cu(II)	Cl	86,6	50%THF	10
Cu4nick16	31,1	H_2O	10	2	20	25,3	Cu(II)	Cl	47,1	50%THF	10
Cu4nick17	65,7	50%THF	20	4	20	26,7	Cu(II)	Cl	91,3	H_2O	10
Cu4nick18	65,7	50%THF	20	4	20	26,7	Cu(II)	Cl	93,2	50%THF	10
Cu4nick19	65,7	50%THF	20	4	20	26,7	Cu(II)	Cl	49,1	H_2O	10
Cu4nick20	65,7	50%THF	20	4	20	26,7	Cu(II)	Cl	49,4	50%THF	10
Cu4nick21	30,1	50%THF	10	1	10	24,4	Cu(II)	Cl	89,9	THF	10
Cu4nick22	33,1	50%THF	10	2	20	26,9	Cu(II)	Cl	89,9	THF	10
Cu4nick23	30,1	50%THF	10	1	10	24,4	Cu(II)	Cl		THF	
Cu4nick24	33,1	50%THF	10	2	20	26,9	Cu(II)	Cl		THF	
Cu4nick25	31,5	H_2O	10	1	10	25,6	Cu(II)	Cl	84	THF	10
Cu4nick26	32,9	H_2O	10	2	20	26,7	Cu(II)	Cl	84	THF	10
Cu4nick27	31,5	H_2O	10	1	10	25,6	Cu(II)	Cl	47,7	THF	10
Cu4nick28	32,9	H_2O	10	2	20	26,7	Cu(II)	Cl	47,7	THF	10

Tab.S.3.4, counterdiffusion crystallization, ligand solution layered over metal gelled solution

code	[M] (mM)		solvent	%gel	[L] (mM)	solvent	[L]+[M] (mM)	[L]/[M]	%THF	phases sol	gel
4nick34		50,0	H_2O	20%	50,0	H_2O	50,0	1,0	0%	1	\
4nick64		25,8	H_2O	10%	51,3	50%THF	38,5	2,0	24%	1	\
4nick62		25,8	H_2O	20%	24,7	50%THF	25,2	1,0	24%	1	\
4nick60		50,6	H_2O	10%	51,3	50%THF	50,9	1,0	24%	1	\
4nick58		50,6	H_2O	20%	24,7	50%THF	37,6	0,5	24%	1	\
4nick55		26,0	50%THF	10%	50,5	H_2O	38,2	1,9	24%	1	\
4nick52		26,0	50%THF	20%	25,2	H_2O	25,6	1,0	24%	1	\
4nick49		50,6	50%THF	10%	50,5	H_2O	50,5	1,0	24%	1	\
4nick46		50,6	50%THF	20%	25,2	H_2O	37,9	0,5	24%	1	\
4nick56		26,0	50%THF	10%	52,2	50%THF	39,1	2,0	50%	3	\
4nick53		26,0	50%THF	20%	26,1	50%THF	26,0	1,0	50%	3	\
4nick50		50,6	50%THF	10%	52,2	50%THF	51,4	1,0	50%	\	2
4nick47		50,6	50%THF	20%	26,1	50%THF	38,3	0,5	50%	\	2
4nick57		26,0	50%THF	10%	51,1	THF	38,5	2,0	50%	1	2
4nick54		26,0	50%THF	20%	25,5	THF	25,8	1,0	50%	1	\
4nick51		50,6	50%THF	10%	51,1	THF	50,8	1,0	50%	1	2
4nick48		50,6	50%THF	20%	25,5	THF	38,1	0,5	50%	1	\

Tab.S.3.5, counterdiffusion crystallization, ligand solution layered over metal gelled solution

code	M	X	MX2 (mg)	solvent	V (gel) (mL)	V (TMOS) (mL)	%gel	[M] (mM)	L (mg)	[L] (mM)	solvent	V (mL)
4nick3	Cu (II)	Br	85,3	50%THF	15	1,5	10	25,5	30,5	24,8	THF	10
4nick6	Cu (II)	Br	84,6	50%MeOH	15	1,5	10	25,3	30,7	24,9	MeOH	10
4nick9	Cu (II)	F	37,8	50%THF	15	1,5	10	24,8	30,5	24,8	THF	10
4nick12	Cu (II)	F	37,8	50%MeOH	15	1,5	10	24,8	30,7	24,9	MeOH	10
4nick13	Co (II)	F	21,5	50%THF	5	0,5	10	25,4	77,8	25,3	50%THF	25
4nick14	Fe (II)	F	11,4	50%THF	5	0,5	10	24,3	77,8	25,3	50%THF	25
4nick15	Mn (II)	F	12,8	50%THF	5	0,5	10	27,5	77,8	25,3	50%THF	25
4nick16	Ni (II	F	13,7	50%THF	5	0,5	10	28,3	77,8	25,3	50%THF	25
4nick17	Co (II)	Br	27,3	50%THF	5	0,5	10	25,0	77,8	25,3	50%THF	25
4nick18	Fe (II)	Br	27,0	50%THF	5	0,5	10	25,0	18,4	24,9	50%THF	6
4nick19	Mn (II)	Br	26,8	50%THF	5	0,5	10	25,0	77,8	25,3	50%THF	25
4nick20	Ni (II)	Br	27,3	50%THF	5	0,5	10	25,0	77,8	25,3	50%THF	25
4nick21	Cd (II)	Br	43,1	50%THF	5	0,5	10	25,0	77,8	25,3	50%THF	25
4nick22	Co (II)	Br	57,7	50%THF	5	0,5	10	52,8	154,2	50,1	50%THF	25
4nick23	Fe (II)	Br	53,6	50%THF	5	1	20	49,7	18,4	24,9	50%THF	6
4nick24	Mn (II)	Br	56,9	50%THF	5	0,5	10	53,0	154,2	50,1	50%THF	25
4nick25	Ni (II)	Br	56,9	50%THF	5	0,5	10	52,1	154,2	50,1	50%THF	25
4nick26	Cd (II)	Br	87,6	50%THF	5	0,5	10	50,9	154,2	50,1	50%THF	25
4nick27	Mn (II)	Cl	49,9	50%THF	5	0,5	10	50,4	157,7	51,2	50%THF	25
4nick28	Cu (II)	Cl	44,1	50%THF	5	0,5	10	51,7	157,7	51,2	50%THF	25
4nick29	Ni (II)	Cl	60,0	50%THF	5	0,5	10	50,5	157,7	51,2	50%THF	25
4nick30	Co (II)	Cl	61,0	50%THF	5	0,5	10	51,3	157,7	51,2	50%THF	25
4nick31	Cd (II)	Cl	58,9	50%THF	5	0,5	10	51,6	157,7	51,2	50%THF	25
4nick32	Fe (II)	Cl	49,7	50%THF	5	0,5	10	50,0	157,7	51,2	50%THF	25
4nick33	Cu (II)	Br	14,0	50%THF	5	0,5	10	12,5	7,7	12,5	50%THF	5
4nick34	Cu(II)	Cl	36,3	H_2O	5	1	20	36,7	496,6	40,3	H_2O	100
4nick35	Cu(II)	Br	46,6	H_2O	5	1	20	41,7	496,6	40,3	H_2O	100
4nick36	Co(II)	Cl	47,2	H_2O	5	1	20	39,7	496,6	40,3	H_2O	100
4nick37	Co(II)	Br	47,0	H_2O	5	1	20	43,0	496,6	40,3	H_2O	100
4nick38	Cd(II)	Cl	48,2	H_2O	5	1	20	42,2	496,6	40,3	H_2O	100
4nick39	Cd(II)	Br	73,0	H_2O	5	1	20	42,4	496,6	40,3	H_2O	100
4nick40	Ni(II)	Cl	47,8	H_2O	5	1	20	40,2	496,6	40,3	H_2O	100

code	M	X	MX2 (mg)	solvent	V (gel) (mL)	V (TMOS) (mL)	%gel	[M] (mM)	L (mg)	[L] (mM)	solvent	V (mL)
4nick41	Ni(II)	Br	44,3	H_2O	5	1	20	40,5	496,6	40,3	H_2O	100
4nick42	Fe(II)	Cl	39,8	H_2O	5	1	20	40,0	496,6	40,3	H_2O	100
4nick43	Fe(II)	Br	46,9	H_2O	5	1	20	43,5	496,6	40,3	H_2O	100
4nick44	Mn(II)	Cl	39,8	H_2O	5	1	20	40,2	496,6	40,3	H_2O	100
4nick45	Mn(II)	Br	43,3	H_2O	5	1	20	40,3	496,6	40,3	H_2O	100
4nick46	Cu(II)	Cl	258,7	50%THF	30	3	10	50,6	62,2	25,2	H_2O	20
4nick47	Cu(II)	Cl	258,7	50%THF	30	3	10	50,6	64,3	26,1	50%THF	20
4nick48	Cu(II)	Cl	258,7	50%THF	30	3	10	50,6	62,9	25,5	THF	20
4nick49	Cu(II)	Cl	258,7	50%THF	30	3	10	50,6	124,3	50,5	H_2O	20
4nick50	Cu(II)	Cl	258,7	50%THF	30	3	10	50,6	128,5	52,2	50%THF	20
4nick51	Cu(II)	Cl	258,7	50%THF	30	3	10	50,6	125,8	51,1	THF	20
4nick52	Cu(II)	Cl	132,8	50%THF	30	3	10	26,0	62,2	25,2	H_2O	20
4nick53	Cu(II)	Cl	132,8	50%THF	30	3	10	26,0	64,3	26,1	50%THF	20
4nick54	Cu(II)	Cl	132,8	50%THF	30	3	10	26,0	62,9	25,5	THF	20
4nick55	Cu(II)	Cl	132,8	50%THF	30	3	10	26,0	124,3	50,5	H_2O	20
4nick56	Cu(II)	Cl	132,8	50%THF	30	3	10	26,0	128,5	52,2	50%THF	20
4nick57	Cu(II)	Cl	132,8	50%THF	30	3	10	26,0	125,8	51,1	THF	20
4nick58	Cu(II)	Cl	172,4	H_2O	20	2	10	50,6	30,4	24,7	50%THF	10
4nick59	Cu(II)	Cl	172,4	H_2O	20	2	10	50,6	31,1	25,3	THF	10
4nick60	Cu(II)	Cl	172,4	H_2O	20	2	10	50,6	63,1	51,3	50%THF	10
4nick61	Cu(II)	Cl	172,4	H_2O	20	2	10	50,6	63,4	51,5	THF	10
4nick62	Cu(II)	Cl	87,8	H_2O	20	2	10	25,8	30,4	24,7	50%THF	10
4nick63	Cu(II)	Cl	87,8	H_2O	20	2	10	25,8	31,1	25,3	THF	10
4nick64	Cu(II)	Cl	87,8	H_2O	20	2	10	25,8	63,1	51,3	50%THF	10
4nick65	Cu(II)	Cl	87,8	H_2O	20	2	10	25,8	63,4	51,5	THF	10

Fig.S.3.6, powder precipitation from 20 mL of 50% THF suspension of $CuCl_2 \cdot 2H_2O$ (287,6 mg, 1.7 mmol) and HIso (108.2 mg, 0.9 mmol). [L]+[M] = 160 mM, [L]/[M] = 0.5. XRPD pattern collected from the precipitated powder (blue line) and simulated from phase **2** structure (black line)

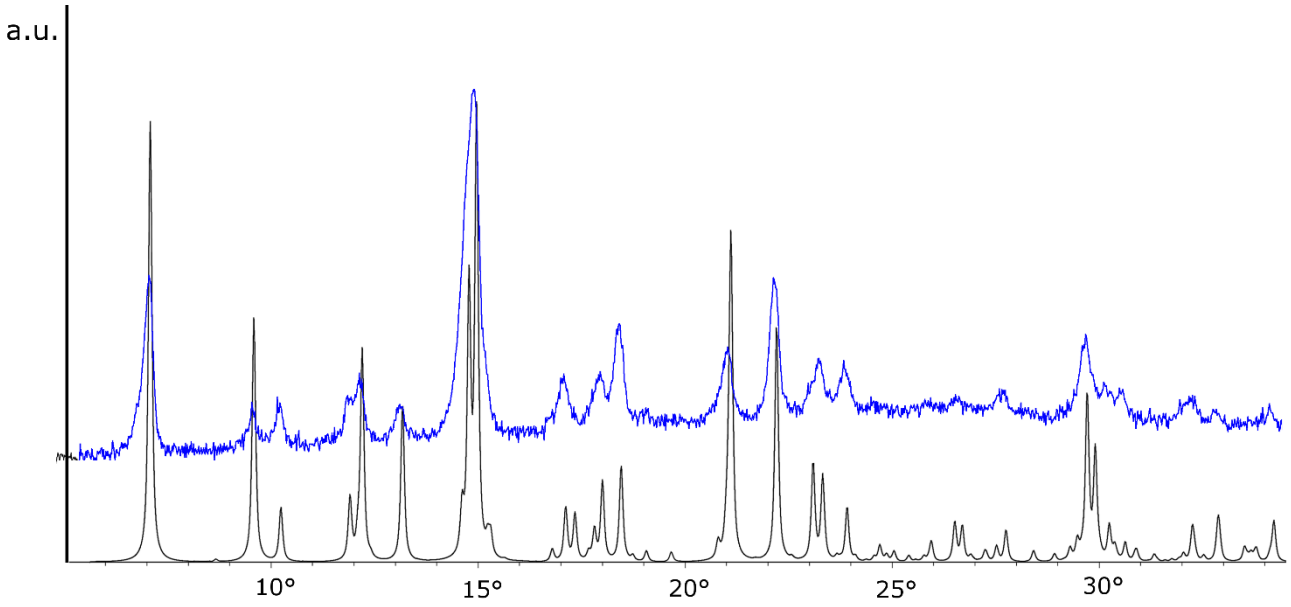

Bibliography

(1) Jellinek, H. H. G.; Urwin, J. R. Ultraviolet Absorption Spectra and Dissociation Constants of Picolinic, Isonicotinic Acids and Their Amides. *J. Phys. Chem.* **1954**, *58* (7), 548–550.

(2) Takusagawa, F.; Shimada, A. Isonicotinic Acid. *Acta Cryst* **1976**, *B32*, 1925–1927.

(3) Almáši, M.; Vargová, Z.; Gyepes, R.; Varga, R.; Zeleňák, V. An Unprecedented Coordisotion Mode of Isonicotisote Ligand in Novel Copper(II) Polymeric Complex: Synthesis, Spectral, Thermal and Magnetic Properties and Their Comparison with Known Molecular Analog. *Inorg. Chem. Commun.* **2014**, *46*, 118–121.

(4) Yang, G.; Zhu, H. G.; Liang, B. H.; Chen, X. M. Syntheses and Crystal Structures of Four Metal-Organic Co-Ordisotion Networks Constructed from Cadmium(II) Thiocyanate and Nicotinic Acid Derivatives with Hydrogen Bonds. *J. Chem. Soc. Dalt. Trans.* **2001**, No. 5, 580–585.

(5) Sekiya, R.; Nishikiori, S. I.; Ogura, K. Crystalline Inclusion Compounds Constructed through Self-Assembly of Isonicotinic Acid and Thiocyanato Coordisotion Bridges. *J. Am. Chem. Soc.* **2004**, *126* (50), 16587–16600.

(6) Sekiya, R.; Nishikiori, S. I. Adsorption and Separation of Poly-Aromatic Hydrocarbons by a Hydrogen-Bonded Coordisotion Polymer. *Chem. Commun.* **2012**, *48* (41), 5022–5024.

(7) Neumann, T.; Werner, J.; Jess, I.; Näther, C. Poly[(μ-1,3-Thiocyanato-κ *N* , *S*)(Isonicotisoto-κ *N* , *O*)(Ethanol-κ *O*)Cadmium(II)]. *Acta Crystallogr. Sect. E Struct. Reports Online* **2012**, *68* (11), m1338–m1338.

(8) Yu, J. H.; Lu, J.; Xu, Y.; Zhang, X.; Xu, J. Q. Supramolecular Structures and Fluorescence Properties of Three Transition-Metal Complexes. *Inorganica Chim. Acta* **2006**, *359* (10), 3205–3211.

(9) Liu, Q.; Wei, Y.; Wang, W.; Zhang, S. Tetraaquabis(4-Pyridinecarboxylato- *N*)Iron(II). *Acta Crystallogr. Sect. C Cryst. Struct. Commun.* **1999**, *55* (10), IUC9900127.

(10) Yu, J. H.; Xu, J. Q.; Ye, L.; Ding, H.; Jing, W. J.; Wang, T. G.; Xu, J. N.; Jia, H. Bin; Mu, Z. C.; Yang, G. Di. Hydrothermal Synthesis and Characterization of a Copper(I) Halide Coordisotion Polymer with Isonicotinic Acid (IN) Ligand as a Template Possessing Three-Dimensional Supramolecular Network Structure. *Inorg. Chem. Commun.* **2002**, *5* (8), 572–576.

(11) Batten, S. R.; Harris, A. R. *Trans* -Tetraaquabis(Pyridine-4-Carboxylate-κ *N*)Nickel(II). *Acta Crystallogr. Sect. E Struct. Reports Online* **2001**, *57* (1), m7–m8.

(12) Matoga, D.; Roztocki, K.; Wilke, M.; Emmerling, F.; Oszajca, M.; Fitta, M.; Bałanda, M. Crystalline Bilayers Unzipped and Rezipped: Solid-State Reaction Cycle of a Metal-Organic Framework with Triple Rearrangement of Intralayer Bonds. *CrystEngComm* **2017**, *19* (22), 2987–2995.

(13) Cai, Y.; Kulkarni, A. R.; Huang, Y. G.; Sholl, D. S.; Walton, K. S. Control of Metal-Organic Framework Crystal Topology by Ligand Functionalization: Functionalized HKUST-1 Derivatives. *Cryst. Growth Des.* **2014**, *14* (11), 6122–6128.

(14) Wang, Z.; Wilson, S. R.; Foxman, B. M.; Lin, W. 3)] ♁. **1999**, *2* (99), 91–100.

(15) Neumann, T.; Werner, J.; Jess, I.; Näther, C. Poly[(μ $_3$ -Pyridine-4-Carboxylato-κ ^{3} *O* : *O* ′: *N*)(Pyridin-1-Ium-4-Carboxylato-κ *O*)(Thiocyanato-κ *N*)Cobalt(II)]. *Acta Crystallogr. Sect. E Struct. Reports Online* **2012**, *68* (12), m1435–m1435.

(16) Huang, D.; Wang, W.; Zhang, X.; Chen, C.; Chen, F.; Liu, Q.; Liao, D.; Li, L.; Sun, L. Synthesis, Structural Characterizations and Magnetic Properties of a Series of Mono-, Di- and Polynuclear Manganese Pyridinecarboxylate Compounds. *Eur. J. Inorg. Chem.* **2004**, No. 7, 1454–1464.

(17) Fellows, S. M.; Prior, T. J. Polymorphism and Solid−gas/Solid−solid Reactions of Isonicotinic Acid, Isonicotisomide, and Nicotisomide Copper Chloride Compounds. *Cryst. Growth Des.* **2017**, *17* (1), 106–116.

(18) Lu, J. Y.; Babb, A. M. An Unprecedented Interpenetrating Structure with Two Covalently Bonded Open-Frameworks of Different Dimensionality. *Chem. Commun.* **2001**, 821–822.

(19) He, Y. C.; Guo, J.; Zhang, H. M.; Yang, J.; Liu, Y. Y.; Ma, J. F. Syntheses of Two Coordisotion Polymers with Rutile-Type Topology and the Single-Crystal-to-Single-Crystal Transformation of Mg(Ii) Complex Induced by Methanol. *CrystEngComm* **2014**, *16* (20), 4210–4214.

(20) Xiong, R.; Wilson, R.; Lin, W. Bis(Isonicotisoto)Iron(II): A Rare, Neutral Three-Dimensional Iron Coordisotion Polyme. *Dalt. Commun.* **1998**, 4089–4090.

(21) Wei, Q.; Nieuwenhuyzen, M.; Meunier, F.; Hardacre, C.; James, S. L. Guest Sorption and Desorption in the Metal–organic Framework [Co(ISO) $_2$] (ISO = Isonicotisote) – Evidence of Intermediate Phases during Desorption. *Dalt. Trans.* **2004**, No. 12, 1807–1811.

(22) Liao, J. H.; Lai, C. Y.; Ho, C. De; Su, C. T. Syntheses and Characterization of Two Coordisotion Polymers: [Cd(Isonicotisote)2(H2O)]·DMF and Cd3(Isonicotisote)4(NO3)2(4,4'-Bipy)2(H2O)2. *Inorg. Chem. Commun.* **2004**, *7* (3), 402–404.

(23) Liu, B.; Yuan, Q. Two Novel Linear Arrangement D10 Hexamers with Isonicotinic Acid: Structures, Blue Luminescent and Semiconducting Properties. *Inorg. Chem. Commun.* **2005**, *8* (11), 1022–1024.

(24) Evans, O. R.; Wang, Z.; Xiong, R.-G.; Foxman, B. M.; Lin, W. Nanoporous, Interpenetrated Metal-Organic Diamondoid Networks. *Inorg. chem* **1999**, *38* (8), 2960–2973.

(25) Lu, J. Y.; Runnels, K. A. An Unprecedented Mixed-Valent-Copper Mutual-Face-Insertion Layered Metal-Organic Polymer Displaying Graphite-like Properties. *Inorg. Chem. Commun.* **2001**, *4* (11), 678–681.

(26) Granifo, J.; Baggio, R. Poly[[Aquabis(μ $_2$ -Isonicotisoto-κ ^{3} *N* : *O* , *O* ')Cadmium(II)] 1,4-Di-3-Pyridyl-2,3-Diaza-1,3-Butadiene Hemisolvate]. *Acta Crystallogr. Sect. C Cryst. Struct. Commun.* **2007**, *63* (7), m327–m330.

(27) Lu, T.-B.; Luck, R. L. Interpenetrating Nets in *Cis* -Bis(Pyridine-4-Carboxylate)Nickel(II). *Acta Crystallogr. Sect. C Cryst. Struct. Commun.* **2002**, *58* (3), m152–m154.

(28) Li, Z.; Du, L.; Zhou, J.; Li, L.; Hu, Y.; Qiao, Y.; Xie, M.; Zhao, Q. A Chiral Porous Cobalt-Organic Framework Based on Reinforced Sinusoidal-like SBUs Involving in Situ-Generated Formate. *New J. Chem.* **2013**, *37* (8), 2473–2478.

(29) Liu, Y.-H.; Lu, Y.-L.; Tsai, H.-L.; Wang, J.-C.; Lu, K.-L. Hydrothermal Synthesis, Crystal Structure, and Magnetic Property of Copper(II) Coordisotion Networks with Chessboard Tunnels. *J. Solid State Chem.* **2001**, *158* (2), 315–319.

(30) Lian, T. T.; Chen, S. M. A New Microporous Cu(II)-Isonicotisote Framework with 8-Connected Bcu Topology. *Inorg. Chem. Commun.* **2012**, *18*, 8–10.

(31) Lu, J. Y.; Babb, A. M. An Extremely Stable Open-Framework Metal-Organic Polymer with

Expandable Structure and Selective Adsorption Capability. *Chem. Commun. (Camb).* **2002**, No. 13, 1340–1341.

III-Gel media effect on crystal habit

Introduction

Crystal habit can become a sensitive issue when planning practical applications of coordination polymer materials, for example, for catalysis or gas sorption.

All processes involved during its nucleation and growth from solution determine the actual habit of a crystal. The processes of self assembly of the crystal imply all the interactions occurring between the constituting units of the crystal, the solution and the growing solid surface.

For coordination polymers these phenomena are far more complex because the process of self-assembly of the crystal also determines the topology and dimensionality of the obtained material. In the previous chapters we have already shown how small variations of simple features like reagent concentration and ratio can induce the formation of completely different networks.

Indeed, besides a careful choice of suitable building blocks and reaction conditions, only approximate models for the network formation from solution are presently available[1].

The last years, application of optical or atomic microscopy techniques has shed some light over these features. Studies were performed on coordination polymers. these studies reveal the importance of the solution behaviour of ligand molecules and metallic centres, which lead towards the formation of complexes, or small oligomers that play crucial roles during the growing process. [2–8].

From the point of view of crystal habit, the determining factor is the grow rate of the different faces, that is determined by the potential energy that binds a growing unit over a crystal surface. Methods developed for the simulation of crystal habit and morphology are based on this assumption.

The first developed method for the simulation of crystal morphology of already known phases, the Bravais-Friedel-Donnay-Harker method (FBDH), is based exclusively on the geometry of the unit cell and its symmetry. Briefly, the interplanar distances are related with the actual energy of interaction, and their reciprocal values approximate the relative growth rate.

On the contrary, the PBC theory developed by Hartman and Perdok (HP) is founded on the interactions that the constituting units display inside the crystalline structure as will be later better discussed. Briefly, according to PBC theory, the behaviour (or character) of a face (*hkl)* is determined by the number of PBC vectors, representing repeated patterns of strong intermolecular interactions, running inside the stoichiometric d_{hkl} growth layer.

Two main issues arise with the application of the PBC theory to coordination polymers. The first is the identification of a proper building unit (B.U.), that is, the molecular entity that is actually added during the growth process. This is not trivial, considering the network nature of these systems and what has been previously discussed about the complex solution equilibria displayed by ligands and metal ions. The second issue is the choice of a proper potential to model all the interactions. This aspect is crucial, because some preliminary approaches have already shown that the identification of coordination bonds as the dominating, on the basis of chemical intuition, does not bring results consistent with experimental evidence [3,4].

PIXEL[9] is a widely used method for the evaluation of interaction energies between organic molecules. Recently the parametrization of the program has been extended to the first row of the transition metals[10], extending the applicability of this method. PIXEL was originally meant for non-charged atoms, but educated parameter guessing can fix the problem for our purposes. The method calculates not only the interaction potentials but also their coulombic, polarization, dispersion, and repulsion components, giving valuable information about the nature of the interaction itself. the overall reliability of PIXEL is documented by comparisons with ab initio calculations[11].

The task of this project is to identify what is the effect of gel media on the crystallization of a coordination compound from the point of view of the crystal habits. The simulation the the crystal habit of a coordination compound will be performed using different approaches. Results will be compared with output from crystallization experiments, performed both in bulk solution and in gel media. Simulation will be performed using PIXEL formalism in the framework of HP theory and classical BFDH method. In the present project we studied the copper bis-isonicotinate tetra-aquo complex, which triclinic crystal structure (phase **1** in chapter 3) has been previously determined.

Bravais –Friedel-Donnay-Harker (FBDH) approach

The Friedel-Bravais method for the simulation of crystal morphology relies on the assumption that the most morphologically important forms of a crystal are the ones showing the highest *reticular density*, that is the largest amount of lattice nodes or *space group equipoints* per unit area. The reticular density is inversely proportional to the *reticular area S* of a face, that is the smallest mesh in the net, and directly proportional to the interplanar distance d_{hkl}. Using this last assumption, the importance of forms can be ranked accordingly with their characteristic d_{hkl} value.

Donnay and Harker [12] introduced in the method some corrections related to the symmetry of the net. Mainly, they focused on the property of glide planes and screw axes to generate *lattice equipoints*, that are analogous to the regular *space group equipoints*, but cannot be generated from them using only the translation vector of the lattice without applying also a rotation or a reflection operation. Due to the symmetry operation the former and the latter equipoints do not display the same motif. *Space group equipoints* are surrounded by perfectly congruent and equioriented motifs. *Lattice equipoints* generated by screw axis show a congruent motif but with a different orientation, *Lattice equipoints* generated by glide planes show an enantiomorphous motif. According to Donnay and Harker, the reticular density of both the *space group equipoints* and the *lattice equipoints* determines the importance of the forms. Let us consider a direction [*hkl*] parallel to a screw axis with a screw component 1/*n*. The screw operation will span *n* equivalent planes whose distance is d_{hkl}/n, that is the distance that has to be considered evaluating the importance of a form.

From an energetic point of view, the method relies on the low anisotropy of the interactions between the constituting units. If this is assumed the distance can be considered inversely proportional to the strength of the interactions, and then became a key parameter about the growth [13].

Hartman-Perdok (HP) approach

The method is based on the identification of the Building Unit (BU) of a crystals and of the strongest interactions that it forms [14–16]. The BU is a portion of the crystal content representative of the stoichiometry and that can be considered as the single ‘’brick’’ by which the crystal is formed. The strongest attractive interactions are responsible for the cohesion of the crystalline solid; they can be identified as the bonds that hold the crystal BUs together.

A PBC consists of BUs bind by strong interactions and repeating themselves along a precise crystallographic direction. No net dipole moment can be normal to the PBC direction as well as the repeating unit must represent the stoichiometry of the crystalline compound. The simplest PBCs are formed by the repetition of the same strong interaction, but PBCs can come also from combination of different strong bonds. PBC terminations (ends) are sites where the growing crystal more likely adds new particles. The importance of a PBC is determined by the End Chain Energy (ECE) parameter, that is the energy released placing a BU on the crystallographic position at the end of a

semi-infinite PBC. The crystal is then considered a fabric of Periodic bond chains (PBC) that determines the behaviour of the different forms according to the following working hypothesis.
Considering a face (*hkl)*, within a layer of thickness d_{hkl} , as determined by the extinction rules of the space group, can run any number of PBC. If there are at least two non-parallel PBC's, the face is considered flat (F) at the molecular level. This means an F face adds more likely BU along its edges than over itself. F faces are also the most stables, so when crystals reach their equilibrium morphology they should show only F faces. If only one PBC is parallel to a face it is considered stepped (S), kinked (K) faces has not any parallel PBC. These two last kinds of faces are more unstable and shouldn't have any relevance in the equilibrium morphology. This is a qualitative evaluation of the forms bounding a crystal. Calculations of some energetic parameters can lead to effective simulation of the equilibrium and growth morphology.
The attachment energy $E_{att}^{(hkl)}$ is defined as the energy released per BU when a layer of thickness d_{hkl} adds over a face (*hkl*). This parameter is important for the kinetics of growth and leads to the direct identification of the *growth morphology*. In particular, the direct relation for a F face (*hkl*) of the growth rates (R_{hkl}) orthogonal to the surface and attachment energy is well-known from literature [17,18]. The actual stability of a form determines its area compared to the total surface area of the crystal in the *equilibrium morphology*. The stability can be estimated calculating the surface tension $\gamma(hkl)$. The simplest approach is to treat all the interactions as exactly additive. Let's consider a crystal as a stacking of slices of thickness d_{hkl}. The potential experienced by a BU sitting over the uppermost layer comes from the summation of all the interactions that the BU forms with the layer below. This is the attachment energy $E_{att}^{(hkl)} = \sum_{i=1}^{n} E_i^{(hkl)}$, where *n* is the total number of slices and n=1 is the first slice below the BU. If the BU belong to the surface, the interactions with the molecules belonging to its same slice has to be added. This quantity is $E_{slice}^{(hkl)}$ and can be described also as the energy released per BU forming a single slice of thickness d_{hkl}.
$E_{slice}^{(hkl)}$ and $E_{att}^{(hkl)}$ are strictly related because the potential energy of a BU in the bulk of the crystal can be defined as $E_{cry} = E_{slice}^{(hkl)} + E_{att}^{(hkl)} + E_{att}^{(\overline{hkl})}$. The quantity E_{cry} is equal to twice of the lattice energy of the crystal. Its halved modulus correspond to the sublimation enthalpy. For centrosymmetric crystals: $\Delta H_{sub} = \frac{1}{2} E_{slice}^{(hkl)} + E_{att}^{(hkl)}$ [19].
The surface tension can be calculated as the work needed to move a BU from the bulk to the surface of a face (*hkl)*, normalized with respect to the area of the face (*hkl*) spanned by a single BU ($A_{mesh}^{(hkl)}$). This work corresponds to the difference of potential energy between a molecule in the crystal bulk and inside the surface ($U_{sur}^{(hkl)} - U_{bulk}$). Adopting the previously defined energetic quantities:

$$\gamma_{hkl} = \frac{(U_{sur}^{(hkl)} - U_{bulk})}{A_{mesh}^{(hkl)}} = \frac{(E_{slice}^{(hkl)} + E_{att}^{(hkl)} - E_{cry})}{A_{mesh}^{(hkl)}} = \frac{-E_{att}^{(hkl)}}{A_{mesh}^{(hkl)}}$$

In this way the surface tension (a thermodynamic quantity) can be calculated normalizing the E_{att}^{hkl} respect to the area actually covered by a BU over a certain face (*hkl*). Applying Wulff construction, we can draw the equilibrium morphology.

Methods

Crystallization experiments

Batch technique

Solution precipitation occurred in batch from water solutions of isonicotinic acid (HINA) and copper(II) chloride. Firstly, we prepared water solutions of the reagents, $CuCl_2 \cdot 4H_2O$ (1.724g, 10 mmol, 25mL water, 404.6 mM) and HINA (1.23g, 10 mmol, 250mL water, 40 mM). We poured the solutions into batches of 24 well PE plates using a micropipette. We followed the order: copper chloride solution, DDW if necessary, HINA solutions. We created a bunch of 47 different crystallization environments, all with the same volume (2mL) and solvent (water). We modify [M]/[L] values ranging from 0.25 to 4 (0,25; 0,3; 0,5; 1; 2; 3; 4) and from 10 to 80 mM with 10mM steps. Due to low HINA solubility in water, high value of both concentration and reagents ratio cannot be reached. The batches were closed and sealed for 6 months. On the same day were opened and photographed. (Experimental detail in supporting information chapter 3, S.3.1)

Gel technique

Gel technique method has already been widely described in the previous chapters, here we report the materials and the preparation method used.

Test tube

Different counterdiffusion experiments were performed inside test tubes. Here we report a general description of the procedure adopted, while in Tab.4.1 are reported the reagents concentrations and solvents composition for any experiment. TetraMethylOrthoSilane (TMOS) solution were prepared by direct mixing of TMOS, water and a reagent (Hiso or $CuCl_2 \cdot H_2O$). The solution was sealed and stirred for 1h, then poured in a glass tube and left overnight to settle. After gel setting, the THF\H_2O solutions of the second is poured over it. The tubes were closed and sealed. After 6 months the samples were photographed.

name	gel	solute	[c] mM	solution	solute	[c] mM	[L]+[M] mM	[L]/[M]
ML1	TMS 10%v/v)	INA	27,21	1:1THF\H_2O	$CuCl_2 \cdot 2H_2O$	50,80	78,01	0,5
ML2	TMS 10%v/v)	INA	27,21	1:1THF\H_2O	$CuCl_2 \cdot 2H_2O$	27,63	54,84	1,0
ML3	TMS 20%v/v)	INA	25,26	1:1THF\H_2O	$CuCl_2 \cdot 2H_2O$	50,80	76,06	0,5
LM	TMS 10%v/v)	$CuCl_2 2H_2O$	25,75	1:1THF\H_2O	INA	51,25	77,01	2,0

Tab.4.1

U-shaped tube

A solution of TMOS in water and THF (1.5 mL TMS; 3.5 mL THF; 5 mL H_2O) was stirred for 1h and dropped in the glass tube. After gel setting, water solutions of HINA (50 mM) and copper chloride (50 mM) were layered over gel in the two different branches. After 6 months the samples were photographed.

Theoretical determination of crystal morphology

PIXEL

The PIXEL package[9,20] was used for the calculation of interactions energies.

This code requests the *ab initio* charge density of the considered structural unit. In fact, In PIXEL view, the structural unit is a grid of charge density points for the cloud of the valence electrons, sourronding nuclear point charges. Information about types of atom and their bonding environments is needed to select an appropriate set of parameters (atomic radius (Å), atomic polarizability ($Å^3$), electronegativity, ionization potential (au)).

The PIXEL environment works on clusters of structural units. Different modules can consider either a single reference unit inside a crystal (PIXELc), or all the interactions displayed by the components of the cluster (PIXELd). For both cases, single unit-unit interaction energies are calculated. Calculation of the interaction energy between two structural units involves the summation of all the interactions between each point charge of a unit with all the point charges of the other. The Coulombic potential is as reliable as the considered wave function, while all the other potential components are calculated and weighted with an appropriate set of parameters.

The total energies reported by PIXELd are the summation of interaction energies of each unit with all the surrounding ones. This additive approach does not apply to polarization energies, that are multi-body interactions and are approximately treated as pairwise additive. For a cluster on *n* units:

$$E_{PIXELd} = \sum_{i=1}^{n}\sum_{j=1}^{n}(E_c + E_p + E_d + E_r)_{i,j} \quad i \neq j$$

PIXELc calculates the packing energy (PE), the energy gained in forming a crystal from a mole of units in the gas phase. To obtain this quantity it considers a portion of crystal formed by structural units within a given distance from the reference unit. Then it calculates the coulombic, polarization, dispersion and repulsion components of each interaction between the reference unit and the selected units. These components are summed and halved except for the polarization energy, that is properly calculated as the polarizing effect of the field formed by all surrounding molecules. For *n* units within a distance *r*:

$$E_{PIXELc} = PE = E_p + \frac{1}{2}\sum_{i=2}^{n}(E_c + E_d + E_r)_{1,i} = -\Delta H_{sub}$$

PIXELc can also be used to study the potential energy exerted by a cluster on a single reference molecule. In this case, the coulombic, dispersion and repulsion components are not halved, but still polarization is calculated as is the field of the cluster polarizing the reference unit. This last approach is useful to describe the potential of a molecule interacting with an already formed crystal, for example a molecule over or inside a surface. It can be used to calculate also the packing potential energy (PPE), the energy cost payed to remove a molecule from a hole in the crystal bulk to gas phase:

$$E_{PIXELc} = PPE = E_p + \sum_{i=2}^{n}(E_c + E_d + E_r)_{1,i}$$

Computational method

PIXELc module estimates the potential energy of interactions between a crystalline cluster and a single reference unit. For the purpose of the present study, the cluster can be formed by the crystal bulk or by planes, ribbons, slices formed by structural units in their crystallographic positions.

The BU of our crystal was used as the structural unit considered by PIXELc. The calculation of PE value is straightforward. Through its energy decomposition in single unit-unit interaction energies, we identify the most relevant interactions inside the structure and their directions. These interactions can be ranked as the strong bonds that give cohesion to the structure, and as such are considered as the most probable component of the PBCs.

To rank the importance of the different PBC we calculated the End Chain Energy values. For every PBC, this value was obtained by creating a cluster with an appropriate chain of BU, then calculating the potential exerted by this chain on the reference molecule. The chain was lengthened until the potential converged. PBCs with ECE<RT (2.48 kJ/mol) were excluded because considered to be too weak top rovide stable binding of the BU.

Using the identified PBC, we determined the character of all the faces. At first, we consider any face (*hkl*) parallel to at least two PBCs, then using a crystal graph to verify that at least two non parallel PBC actually run inside a layer of thickness d_{hkl}. A crystal graph is a schematic representation where the BU are represented only as their centre of mass and strong bond are represented as sticks that connect them. Using this representation all F faces can be tested and plausible S or K faces can be identified.

The set of F faces dominates the stable equilibrium morphology (that is a minimum of surface energy), and can be relevant to identify the kinetically determined growth morphology.

The attachment of a new BU over an already formed face is a pivotal step for crystal growth. For this reason $E_{att}^{(hkl)}$ is a crucial kinetic parameter [17]. To calculate it we consider a hemisphere of appropriate radius exposing the crystal surface cut by the considered plane, onto which the reference molecule sticks on the crystallographic position over its centre.

The relative stability of the faces determines the equilibrium morphology. The stability is reflected in the surface tension. The surface tension was calculated as the work needed to move a BU from the bulk to the surface of face (*hkl*), divided by the area of the face *hkl* covered by a single BU ($A_{mesh}^{(hkl)}$). As previously shown, we calculated this value normalizing $E_{att}^{(hkl)}$ respect to the surface area:

$$\gamma_{hkl} = \frac{-E_{att}^{(hkl)} \cdot z}{A_{mesh}^{(hkl)}}$$

A_{mesh}^{hkl} is the area of the 2D unit cell of the surface (*hkl*). The cell can be defined by the two non parallel PBC that define also the face (*hkl*) itself. Considering the number of 3D unit cell that are cut by a cell of thickness d_{hkl} and as wide as the defined 2D cell and using the Z value of the unit cell, the number of BU insisting on $A_{mesh}^{(hkl)}$ (z) could be found.

The obtained morphologies were compared with both BFDH calculated morphology and experimental outputs.

Results

Structure refinement and description

Crystals for structure determination were grown by counterdiffusion method in gelled solution inside a U-shaped tube. After 1 month large, light blue, prismatic crystals were collected from the gel. Single crystal X-ray diffraction experiments were performed on a Bruker APEX II CCD area detector diffractometer using MoKα radiation (λ=0.71073 Å). An empirical absorption correction (SADABS) was applied, the structures were solved by direct methods (SHELX) and refined by full-matrix least-squares on F^2 (SHELXL-97)46 with WINGX interface. Hydrogens of the pyridine rings are on geometrical calculated positions and refined using a riding model with Uiso=1.2. Hydrogen of water molecules were found using Fourier density difference, then refined using a riding model (Uiso=1.5) and fixed O-H distance (0.993 Å). The following table (Tab.4.2) shows the most important parameters of data collection and structure refinement.

Formula	$CuC_{12}N_2O_8H_{16}$
Fw	381.82
T(K)	298.15
Crystal system	triclinic
Space group	P-1
a (Å)	6.3424(8)
b (Å)	6.8985(8)
c (Å)	9.1876(11)
α	99.43(2)
β	105.23(2)
γ	108.24(2)
V (Å^3)	354.87(7)
Z	1
μ (mm^{-1})	1.59
Reflection measured	4.313
Independent reflection	2160
R_{int}	0.012
$R_1[I>2\sigma(I)]$	0.023
$wR_2[I>2\sigma(I)]$	0.068
$\Delta\rho_{min}$ (e Å^{-3})	-0.414
$\Delta\rho_{max}$ (e Å^{-3})	0.384

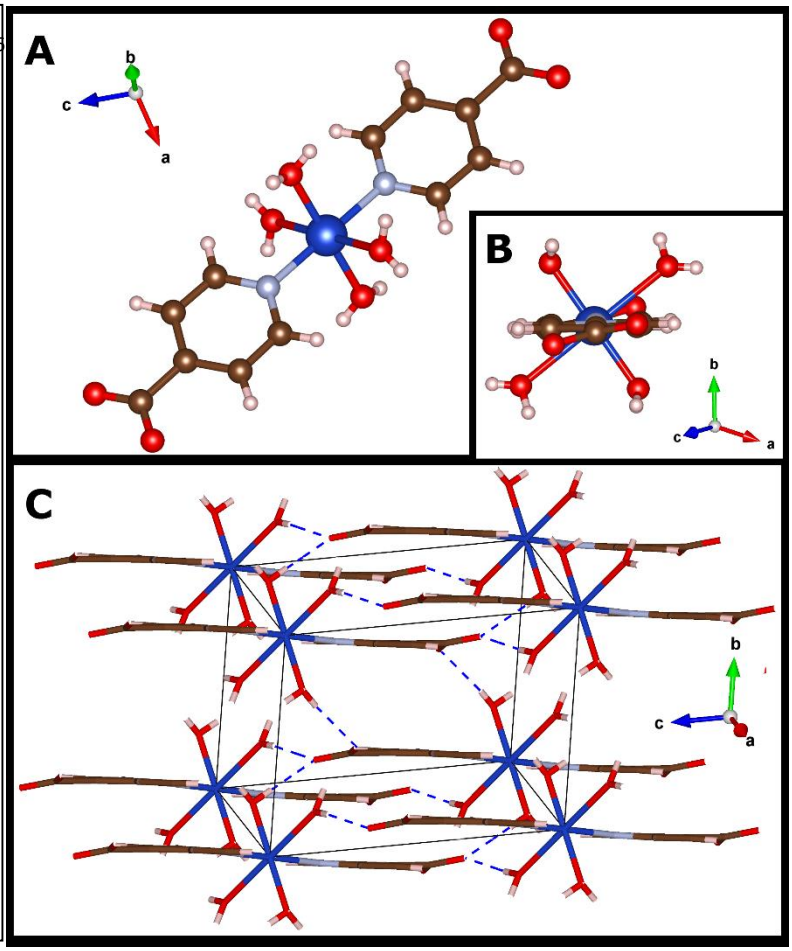

Table 4.2 Parameters regarding data collection, treatment and structure refinement.

Figure5.1, Copper bis-isonicotinate tetra hydrate [Cu(Iso)$_2$(H$_2$O)$_4$] complex (A), detail of the coordinated water molecules (B), packing and H-bonds network (H-bonds represented as blue dotted lines).

Copper(II) bis-isonicotinate tetra hydrate [Cu(Iso)$_2$(H$_2$O)$_4$] complex crystallizes in the triclinic system in space group $P\bar{1}$. The structure consists of discrete copper bis-isonicotinate tetra hydrate complexes (Fig.4.1A). The coordination geometry is octahedral, distorted by Jahn-Teller effect. The

Iso ligands are deprotonated and coordinate the copper atom via their nitrogen atom, occupying two *trans* positions. The water molecules are not coplanar with the pyridine rings and have different Cu-O distances (1.99 Å, 2.45 Å) (Fig.4.1B). The copper atoms sit at cell vertices, insisting on inversion centres. All the carboxylic oxygens and water molecules act respectively as acceptors and donors of strong hydrogen bonds. The resultant is a three dimensional complex network of interactions (Fig.4.1C).

Every complex is connected to six others through charge-assisted hydrogen bonds.[21]
Considering the complex at the origin of the cell, it forms four H-bonds (O···O distances: 2.96 Å; 2.62 Å) with the complex along [101] direction (Fig.2A), and two (O···O distance: 2.73 Å) with the complex in [111] direction (Fig.2B). Both interactions are strengthened by the dipole-dipole interaction between stacked Iso ligands (dipole distances: 3.54 Å [101]; 3.46 Å [111]) and by π-π staking of their pyridine rings (4.013 Å; 4.252 Å). These interactions let the complexes to form a net parallel to the $(10\bar{1})$ plane (Fig.4.2C).
A hydrogen of the more distant water molecule points outside this net. This hydrogen interacts with a carboxylic group of a complexes along [001] direction (O···O distance: 2.83 Å) (Fig.5.2D). Also in this case can be identified a dipole-dipole interaction between Iso ligands (dipole distance 6.11 Å).
The stacking of the complex creates short Cu-Cu distance along axis a and b (6.34 Å, 6.90 Å). Complexes are perpendicular respect to (001) (Fig.4.2E), with short distance between same-charged groups. They form H-bonds with complexes belonging to upward and downward (001) planes (Fig.4.2F).

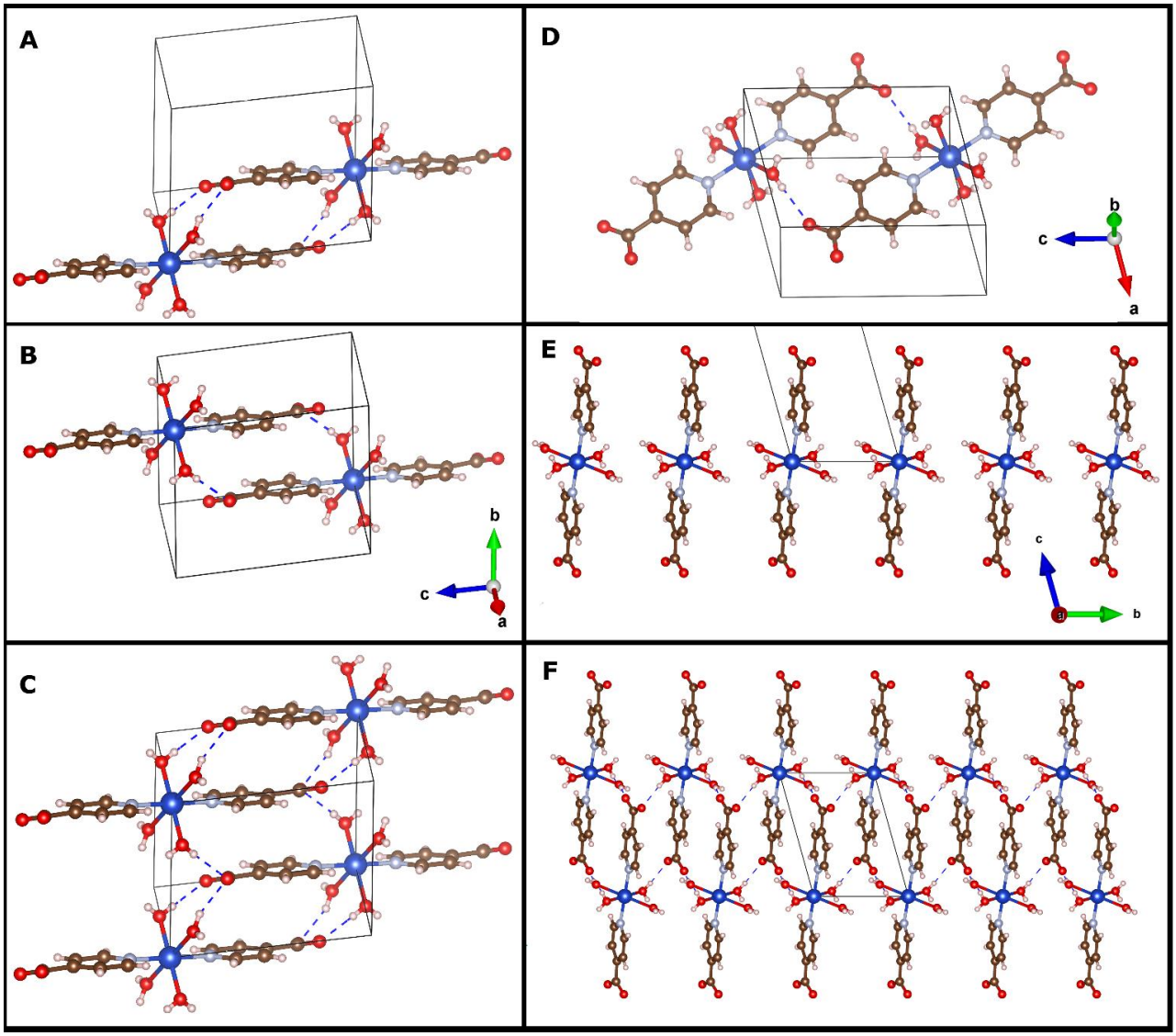

Figure 4.2. Hydrogen bonds along [101] *(A),* [111] *(B), resultant network* [10$\bar{1}$] *(C). Interaction along* [001]*(D). Single plane* (001) *projected along* [100] *(E), two intercalated planes* (001) *projected along* [100] *(H-bonds represented as blue dotted lines).*

Experimental crystal morphology

The crystals of the studied phase show four different habits, presented in the following image (Fig.5.3). The five forms describing all of them are, in order respect to their importance in the habit, {10$\bar{1}$}, {010}, {01$\bar{1}$}, {001}, {$\bar{1}$11}, {1$\bar{1}$0}. Forms {010} and {10$\bar{1}$} are equivalent in the habit labelled as prismatic, and with form {$\bar{1}$11} they bound a prism capped by forms {01$\bar{1}$} and {1$\bar{1}$0} (Fig.4.3A). The other three habits are platelet whose large faces belong to form {10$\bar{1}$}. For the simplest one (Fig.5.3B) the sides of the platelet are forms {010} and {01$\bar{1}$}, describing an elongated rhombic shape. The other two (Fig.4.3C, hexagonal A, and 3D, hexagonal B) derive their pseudo-hexagonal shape from the introduction of form {001}, that became more prominent for the habit labelled hexagonal B. All these habits are related with the relative importance of form {001}. Often the plane (10$\bar{1}$) is a twin plane, this is particularly common for crystals showing platelet habits.

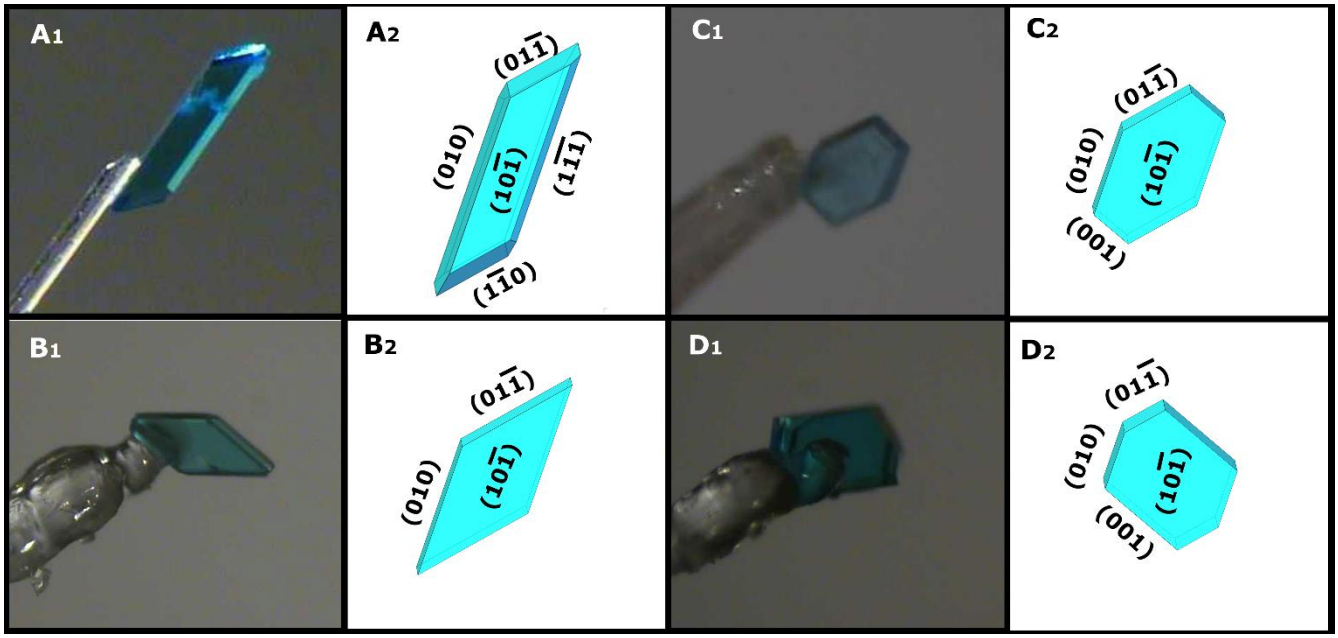

Figure 4.3. Experimental habits, for each of them we report a crystal and the indices of the face. Prismatic (A); rhombic (B); hexagonal A (C); hexagonal B (D).

Crystals precipitated from solutions show all these habits; the platelets are by far predominant. The concentration of the reagents determines the relative importance of the different habits. The prismatic crystals were observed only for the lowest concentration ([L]+[M] = 10 mM; Fig.4.4A). At low concentration (30 mM) the majority of the crystals show the rhombic morphology (Fig.4.4B). Increasing the concentration, we observed the increasing presence of hexagonal morphologies, at first (50 mM; Fig.4.4C) hexagonalA, then (70 mM; Fig.4.4D) hexagonalB. The use of different ratio of [L] and [M] has not shown strong univocal effects.

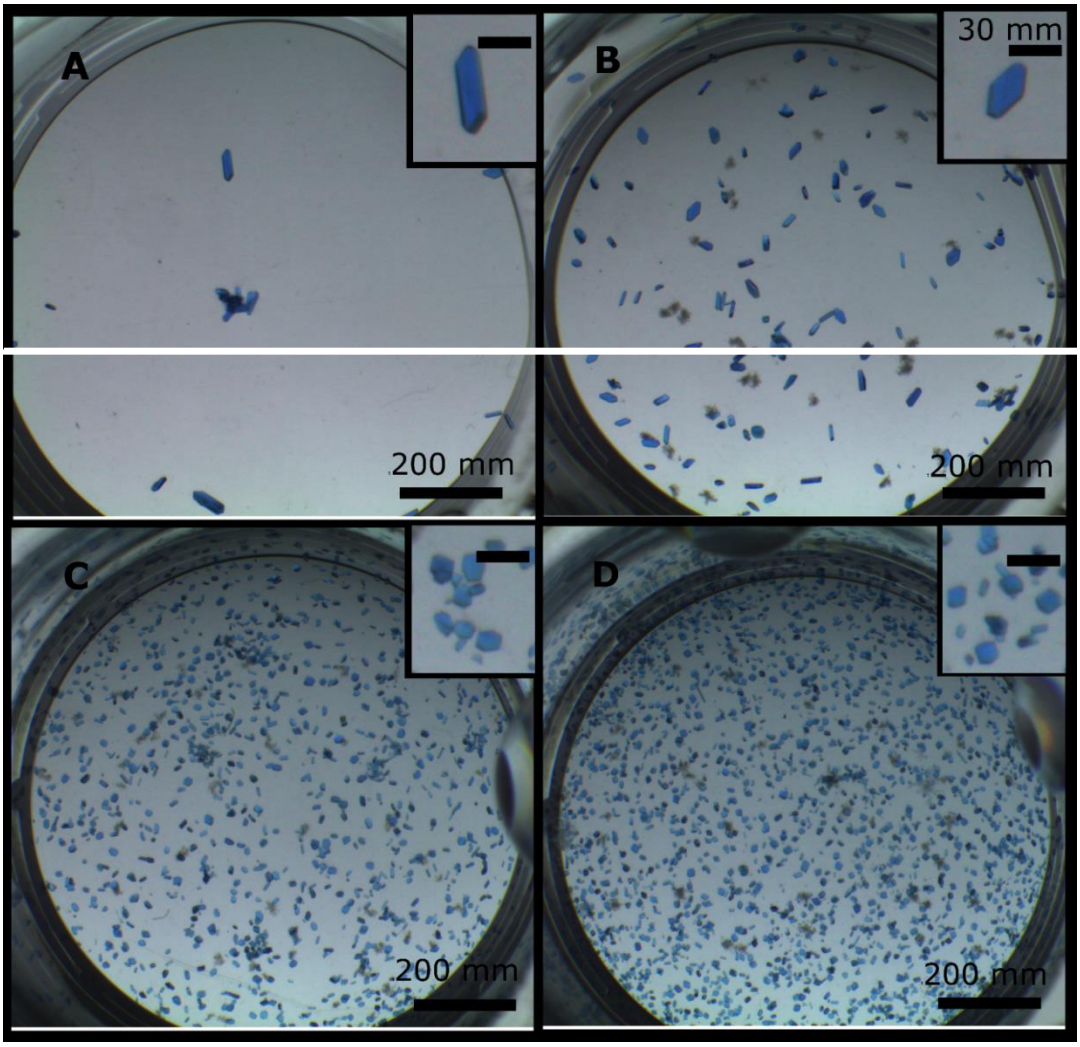

Figure 4.4. Batch crystallization experiment. The reagent ratio was kept constant ([L]/[M]=1), but concentration increase from 10 mM (A) to 30mM (B), 50 mM (C) and 70 mM (D). The insertion is the magnification of a selected area, showing the most characteristic habit.

Crystals formed inside gel media also show both prismatic and platelet morphologies. With the latter becoming the most common. Considering test tubes where the metal solution is poured over the ligand solution, inside gel media there are almost only prisms (Fig.4.5A). Increasing the concentration of the ligand we did not observe modification of the habits (Fig.4.5B). The density of TMOS gel introduces a slightly different behaviour. Inside thicker gel (20% w/v) we observed below the interphase the formation of numerous little crystal, both platelets and prisms, below them few large well-formed prismatic crystals (Fig.4.5C). Pouring the ligand solution over the metal solution the formation of crystals is limited, and their morphology is highly distorted (Fig.4.5D). Prismatic habit is the only observed one if crystals were grown inside a U-shaped tube (Fig.4.5E). We also precipitated crystals from a 50%THF H2O/THF solution, to confirm the little effect induce on morphology by THF solvent (Fig.4.5F), in order to compare gel precipitation with solution precipitation.

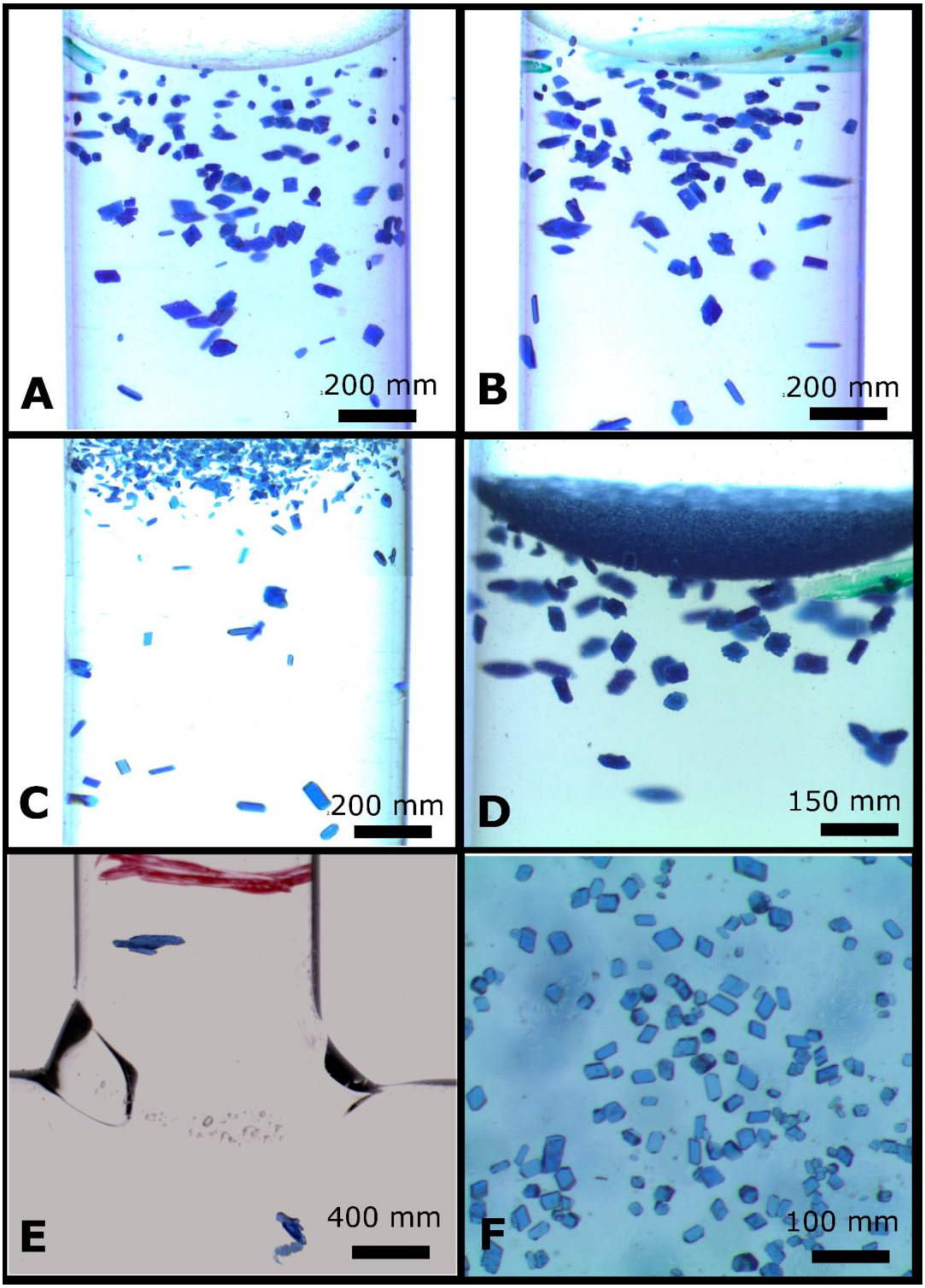

Figure 4.5, Crystallization inside silica gel media. Gel at different concentrations. For any sample is reported experimental set up, agarose density (% w/V), gelified solution and layered solution. The layered solution is always 1:1 THF/H2O. A) test tube, agarose 10%, INA (27.2 mM), CuCl2 50.8 mM. B) test tube, agarose 10%, and INA (27.2 mM), CuCl2 27,7m mM. C)Test tube, agarose 20% (w/v), INA (25.3 mM), CuCl2 50.8 mM. D)Test tube, agarose 10% (w/v), CuCl2 (25.8 mM), INA 51.3 mM. E) U-shaped tube, agarose 15%, branches were filled by CuCl2 (40 mM) solution and INA (40 mM) solution. F) 1:1 THF/H20 solution, CuCl2 (40 mM) and INA (20 mM).

Morphology Simulation

PIXEL analysis

We consider as BU of the crystal the complex copper(II) bis-isonicotinate tetra hydrate $[Cu(INA)_2(H_2O)_4]$. The charge density for the PIXEL calculations was obtained using the Gaussian16 package at MP2/6-31g** level of theory. The experimental molecular geometry, apart from hydrogen atoms whose distances were normalized (1,00 Å for water O-H bonds and 1,08 Å for aromatic C-H), was adopted both for molecular and solid state calculations.

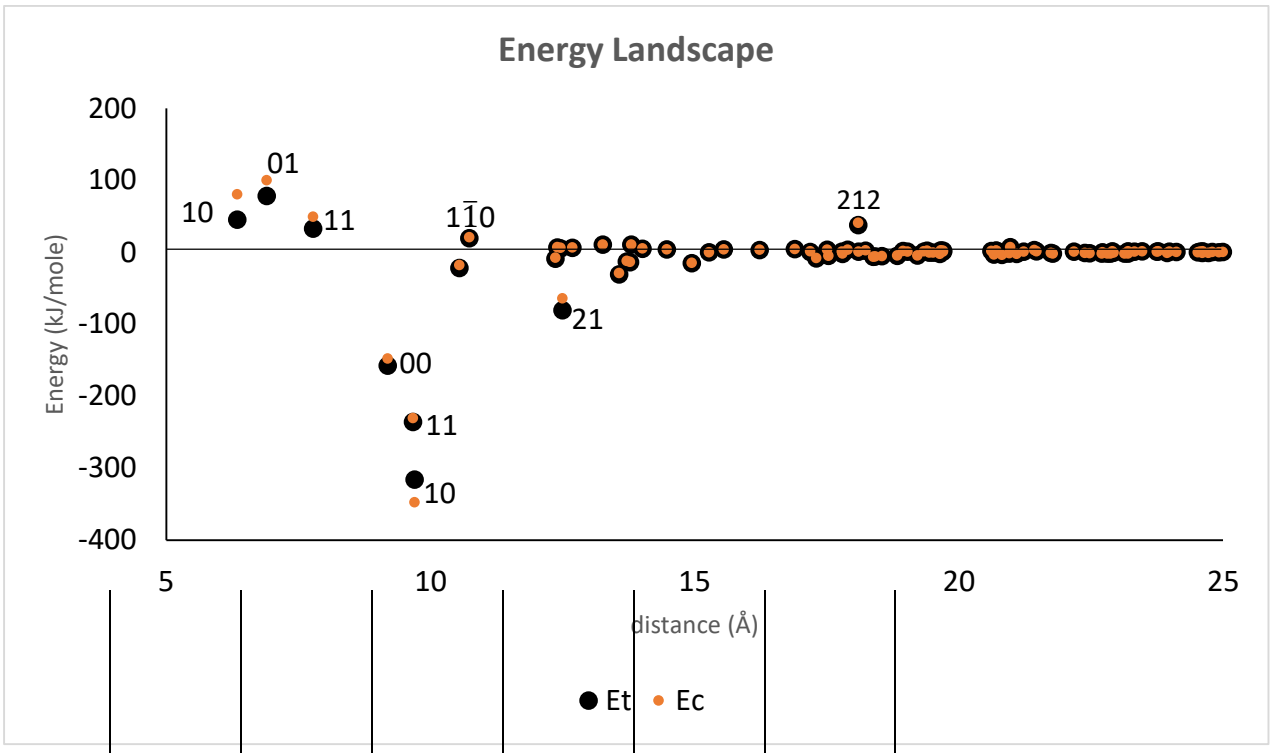

Figure 4.6 Energy landscape. The graph shows the overall interaction potential (black dots) and the coulombic potential (orange dots). The horizontals axis is the distance between centres of dimers, the ordinate is the energy between the corresponding molecular pair, energies for d>20Å are negligible. The five most attractive and repulsive interactions are labelled by the directions [uvw] along which interactions are displayed.

PIXELc calculates both the PE and the potentials of interaction of a BU with all the surrounding units. These latter values were used to form an ‘’Energy Landscape’’ (Fig.4.6), a graph showing the interaction potential of dimers of BU against the distance between centres of mass. The most energetically relevant interactions on the graph, both attractive and repulsive, were labelled by the [uvw] d Ec Ep Ed Er crystallographic direction along which they are displayed.

As previously mentioned, PIXELc calculates the potential of formation of a certain unit-unit dimer as the summation of four kinds of interactions. This decomposition is useful to perform deep inspection of the intermolecular interactions involved. For example, the energy landscape shows the total energy (Et) and its columbic component (Ec). As expected for a systems that, although overall neutral, includes substantial charge separation into formal ions, the latter is very prominent, and at

distances larger than 15 Å, coincident with Et. However, the total energy of interactions came from a summation of all components, and in some cases, they cancel each other.
PIXEL results were checked against dimer complexation energies calculated *ab initio*, with counterpoise correction as encoded by Gaussian16 package, at MP2/6-31g* level of theory. The experimental geometry of complexes and dimers was used. We choose the five most attractive and the five more repulsive dimers. The following table (Tab.4.3) summarize the results obtained. The table shows the difference between PIXELc and *ab initio* and the energy decomposition for the five most attractive and the five most repulsive dimers.

[uvw]	d (Å)	Ec (kJ/mol)	Ep (kJ/mol)	Ed (kJ/mol)	Er (kJ/mol)	Et(PIXEL) (kJ/mol)	Et(MP2) (kJ/mol)	Err%
101	9.697	-347.6	-132.8	-62.4	226.7	-316.2	-351.9	10.16%
111	9.667	-230.8	-82.3	-52.7	129.7	-235.9	-241.3	2.25%
001	9.188	-148	-56.5	-34.3	81.2	-157.7	-157.5	-0.12%
211	12.495	-64.2	-13.4	-11.8	8.8	-80.6	-74.6	-8.03%
201	13.568	-29.2	-1.1	-0.6	0	-30.9	-29.6	-4.42%
$1\bar{1}0$	10.733	20.7	-0.8	-0.4	0	19.5	20.3	3.88%
110	7.773	49.3	-9.2	-8.3	0.9	32.7	36.2	9.56%
212	18.093	40.9	-2.4	-0.7	0	37.8	37.4	-1.20%
100	6.342	80.3	-20.3	-35.9	21	45	/	/
010	6.898	99.9	-14.4	-9	1.5	78	86.5	9.85%

Tab.4.3 Calculated interaction energies for the five most attractive and the five most repulsive dimers. Direction of the interaction (uvw), coulombic (Ec), polarization (Ep), dispersion (Ed) and repulsion (Er) components. Total energy of interaction calculated by PIXEL (Et(PIXEL)) and with ab initio method (Et(MP2). Error of PIXEL calculation respect to "exact" ab initio approach.

As expected from structure inspection, dimers along [101], [111] and [001], which are connected by H-bond (Fig.4.2 A, B, D), show the most stabilizing calculated potential, although with large energy differences. The importance of the coulombic component confirms the charge assisted nature of the H-bonds inside this structure.[21] This component varies considerably within the considered dimers. It decreases by 116.8 kJ/mol from dimer [101] to dimer [111]; by 82.8 kJ/mol from dimer [111] to [001]. To justify these variations, different factors were considered. In the first place, the reciprocal positions of the charged groups: Cu-Cu distances, that are the reported ones in the table, behave in an opposite way respect to Cu – carboxylic oxygen distances. Remarkably, the dimer [101] displays the shortest Cu2+····O- (3.92 Å) and a long (4.36 Å) Cu-Cu distances. While [001] is characterized by the nearest coppers and the longest Cu2+····O- distance (4.87 Å). Dimer [111] displays intermediate values (Cu2+····O- distances: 4.13 Å; 4.49 Å). Then, a minor contribution from the dipole-dipole interactions of the ligands can be expected, and their distance increases for dimers [001] of almost 50% respect to dimers [101] and [111].
The polarization terms considers the polarization induced for every point of charge distribution. In this way, it partly describes the energetic gain related to the crystal-field induced distortion of gas-phase charge distribution.[22] H-bond and dipole-dipole interactions are important for this component, which, in fact, decreases from dimer [101] to [111] by 50.5 kJ/mol, while from [111] to [001] by 25.8 kJ/mol.

The dispersion component (Ed) instead decreases by 9.7 kJ/mol from [101] to [111] and by 18.4 kJ/mol from [111] to [001]. This behaviour is interesting because it might point to the presence of a weak π-π stacking interaction between the pyridine rings of dimers [101] and [111], while dimer [001] shows only H····H (2.53 Å) contacts.

The distance between complexes is the crucial parameter for the Pauli repulsion component. This is large for the nearest complexes, where it almost outweighs the coulombic component. This balance reflects the way by which these interactions are calculated. The *ab initio* calculated charge density belongs to a molecule in its gas phase, so it overlaps with charge densities of its replicas inside the crystal. On one hand it makes possible the calculation of penetration energy, which is the coulombic attraction exerted by nuclei on electrons of a different BU; on the other hand overlap is also responsible for Pauli repulsion. The good performance of the PIXEL approach relies on careful parametrization of each energy component.

Dimers [211], [201] (Fig.4.6) are far weaker respect to the previous ones, but their interaction energies are all but negligible (80 and 30 kJ/mol). Both are stabilized mainly by electrostatic interactions. Coulombic component represents respectively 71.8% and 94.5% of the attractive potentials (Ec+Ep+Ed). Their distance to the reference unit is also similar. However, for dimer [211] significant contributions arise from polarization and dispersion components, which are negligible for dimer [201]. Similarly, the repulsive term is relevant for dimer [211], but gives no contribution to dimer [201]. Inspecting the structure, we observe that molecules forming dimer [211] has a short C-H····O-C distance (2.66 Å), not present in dimer [201].

The dimer [211] is formed by nearest neighbours, and this is reflected in the presence of significant contributions from dispersion interactions. Instead, dimer [201] is formed by ‘’distant’’ units and its stability relies on purely ionic interactions. This behaviour is common to the large majority of the dimers. At R>20Å the building units behave as neutral molecules and attraction energies become negligible.

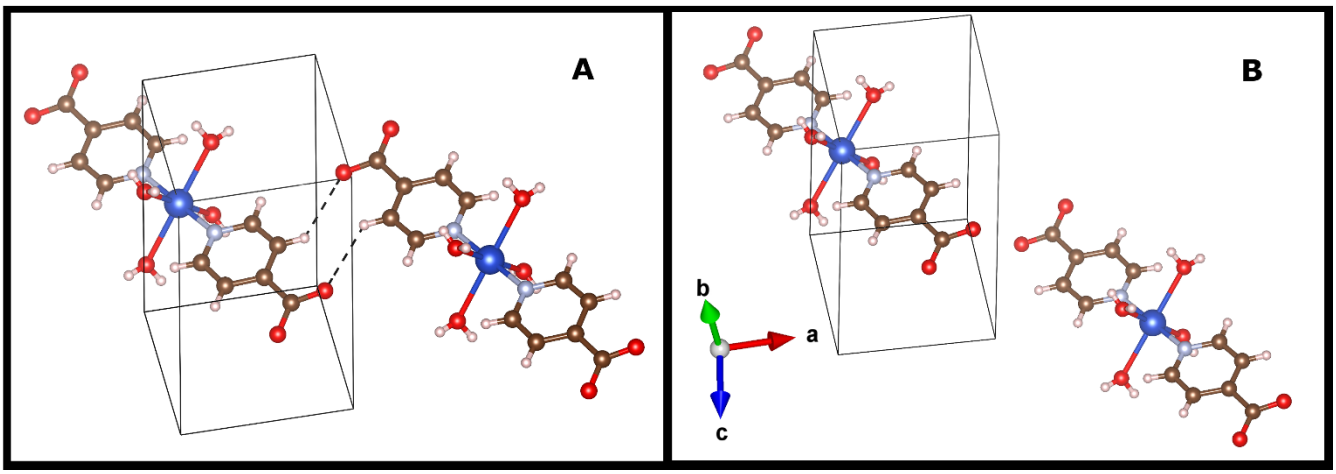

Figure 4.6. Dimers [211] *(A), the short CH-O distance is reported as black dotted lines, and dimer* [201] *(B)*

Repulsive interactions arise mainly from electrostatic repulsion. The orientation of a molecule with respect to the reference one is crucial to determine the effect of the coulombic interactions. Inside plane (001) they are particularly unfavourable because these dimers are related by translations and their groups with same charge face each other. In fact, four of the five most repulsive interactions are

all the nearest neighbour of the BU on this plane (100, 010, 110, $1\bar{1}0$). Similarly, two molecules whose carboxylic groups are facing each other form the repulsive dimer [212].
All the other components steadily decrease with distance, so are less affected by reciprocal orientation and play a very limited role.

PBC

We considered as BU the discrete copper(II) bis-isonicotinate tetra hydrate complex. This choice let us to transfer directly information from PIXEL analysis to HP theory framework. In fact, we have already investigated the intermolecular interactions that bind BU together, that is, the ‘’strong bonds’’. We considered “strong” the interactions whose associated potential has an absolute value bigger than the average thermal energy at room temperature (RT=2.48 kJ/mol). Using this approach we selected the 19 “strong bonds” reported in the following table (Tab.4.4), where each bond is labelled with the crystallographic direction along which is displayed.

	[uvw]	d (Å)	Et (kJ/mol)	Ec (kJ/mol)	Ep (kJ/mol)	Ed (kJ/mol)	Er (kJ/mol)	%Ec
Class 1	**101**	9.697	-316.2	-347.6	-132.8	-62.4	226.7	64.0%
	111	9.667	-235.9	-230.8	-82.3	-52.7	129.7	63.1%
	001	9.188	-157.7	-148	-56.5	-34.3	81.2	62.0%
	211	12.495	-80.6	-64.2	-13.4	-11.8	8.8	71.8%
	201	13.568	-30.9	-29.2	-1.1	-0.6	/	94.5%
Class 2	**011**	10.547	-21.8	-18.1	-2.2	-1.4	/	83.4%
	221	14.945	-15.2	-14.8	-0.3	-0.2	/	96.7%
	$1\bar{1}1$	13.776	-14.2	-13.7	-0.4	-0.2	/	95.8%
	121	13.714	-12.9	-12.4	-0.3	-0.2	/	96.1%
	$01\bar{1}$	12.36	-9	-7.9	-0.7	-0.3	/	88.8%
	311	17.299	-8.6	-8.4	-0.1	-0.1	/	97.7%
	321	18.414	-6	-5.9	-0.1	/	/	98.3%
	012	18.539	-5.7	-5.6	-0.1	/	/	98.2%
	$2\bar{1}1$	17.528	-5.3	-5.2	/	/	/	100.0%
	301	18.831	-4.9	-4.8	/	/	/	100.0%
	122	19.213	-4.8	-4.7	-0.1	/	/	97.9%
	$1\bar{1}2$	20.812	-3.7	-3.7	/	/	/	100.0%
	$0\bar{1}2$	20.659	-3.3	-3.3	/	/	/	100.0%
	102	17.794	-2.6	-2.1	-0.3	-0.1	/	84.0%

Tab.4.4 Strong bonds identified from PIXEL calculation. For any interaction: direction [uvw], centre of mass distance (d), overall interaction potential (Et), coulombic (Ec), polarization (Ep), dispersion (Ed) and repulsion (Er) components, weight of the Ec over the entire attractive potential (%Ec=Ec/(Ec+Ep+Ed))

Their number is quite large due to electrostatic long-range interactions. As can be seen, the coulombic component is responsible for more than half of total attraction potential ($\%E_c = E_c/(E_c+E_p + E_d)$) for all the dimer, and represents more than 90% of the interaction potential for the large majority of them. This situation is the same observed during the comparison of dimers [211] and [201] in the previous paragraph, large coulombic contributions are related with dimers where there are no large interactions apart from the purely ionic one.
We can define two main classes. The first one contains the four strongest bonds. For all these bonds non coulombic interactions are smaller but not negligible respect to the coulombic one. The BU forms these bonds with its nearest neighbours. The second class contains bonds where interactions are based almost exclusively on long distance ionic interactions.

PBC n°	[uvw]	ECE (erg/molecola)
1	101	$-4.1*10^{-12}$
2	111	$-3.2*10^{-12}$
3	001	$-2.3*10^{-12}$
4	211	$-1.2*10^{-12}$
5	201	$-5.1*10^{-13}$
6	011	$-3.9*10^{-13}$
7	221	$-2.6*10^{-13}$
8	$1\bar{1}1$	$-2.5*10^{-13}$
9	121	$-2.3*10^{-13}$
10	$01\bar{1}$	$-1.6*10^{-13}$
11	311	$-1.5*10^{-13}$
12	321	$-1.0*10^{-13}$
13	012	$-9.6*10^{-14}$
14	$2\bar{1}1$	$-9.1*10^{-14}$
15	301	$-8.5*10^{-14}$
16	122	$-8.1*10^{-14}$
17	$1\bar{1}2$	$-6.3*10^{-14}$
18	$0\bar{1}2$	$-5.6*10^{-14}$

Table.4.5 identification of the PBC. For ani PBC are reported direction (uvw) and ECE value.

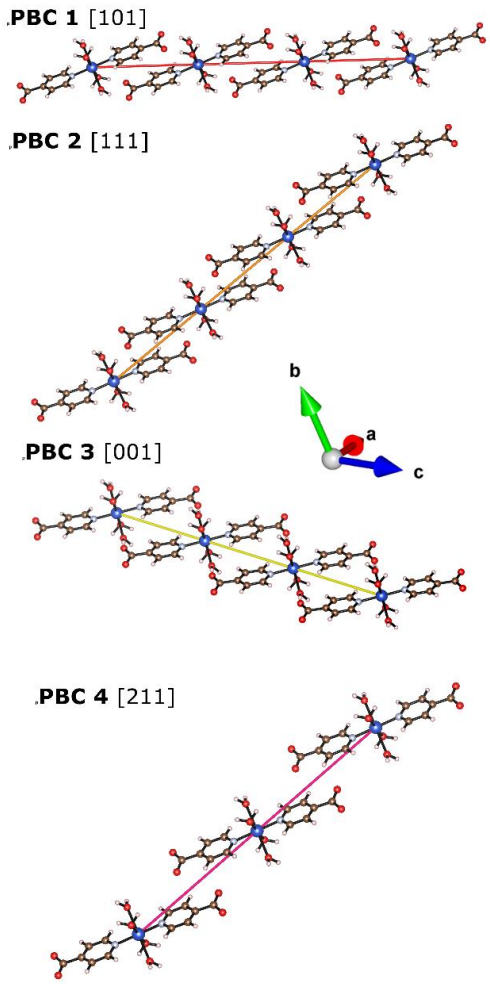

Figure.4.7 Representation of the first four PBC ([101], [111], [001], [211]), which are formed by interaction between nearest neighbour

Starting from the identified strong bonds, we built the PBCs. In our case, the BU coincides with the cell content and the crystal is analogous to an anisotropic Kossel crystal. Due to this, the considered PBCs are formed only by repetition of the already found "strong bonds". The following table (Tab.4.5) reports the calculated ECE values of chain of molecules formed by repetition of these

bonds. We reported the 18 ECE energies bigger than kT (-4.1*10^{-14} erg/molecule). Our PBCs can be similarly divided in two main groups. Complexes that are nearest-neighbours form the first four PBCs (Fig.4.7), while all the others fourteen are based on long-range ionic interactions.
Representing the BUs using only the central copper atom and connecting them with the identified interactions, we draw the graph of the crystal. This is an important graphical tool for the evaluation of the faces character (F, S, and K). Here are reported two partial representations of the graph. The first one shows a single BU (blue dot reperesentig copper atom) and displaying all attractive interactions (Fig.4.8A), the second one is a portion of the crystal (2x2x2 cells) and shows the fabric formed by only the first four PBCs (Fig.5.8B)

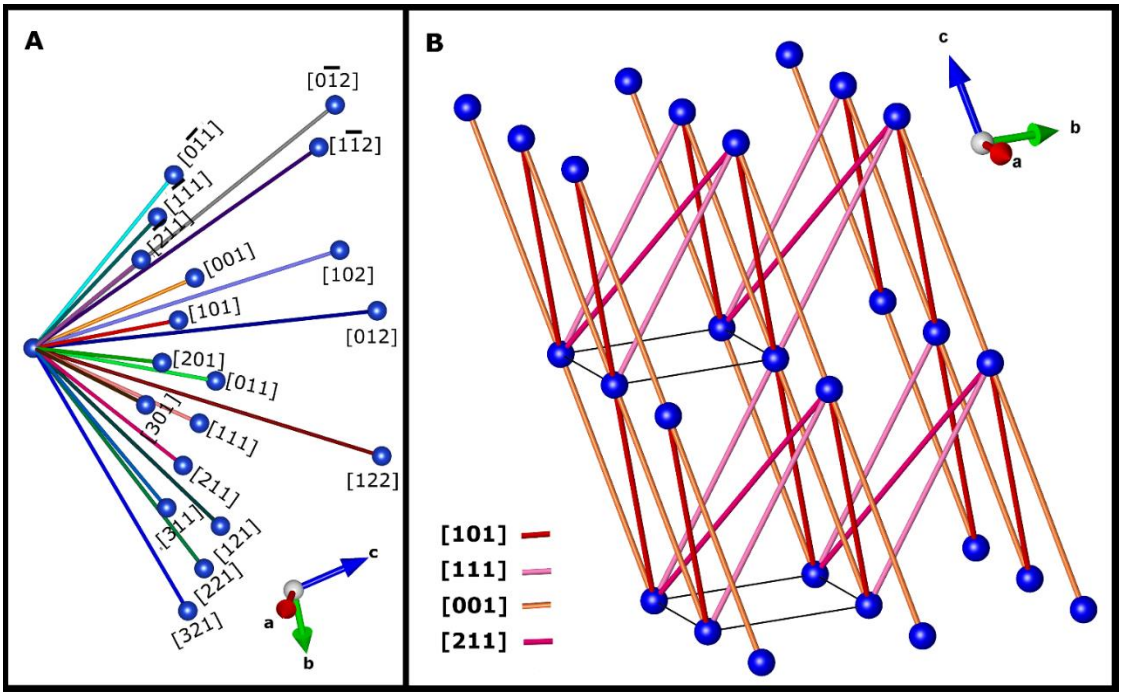

Figure.4.8 Representations of the crystal graph. A single BU and all its interactions (A), a portion of the crystal (2x2x2 unit cells) with the depiction of the first four PBCs ([101], [111], [001], [211]). BUs are represented by copper atom only.

Growth and equilibrium morphology

Using the PBCs we can identify flat faces (F). A face *hkl* of this kind must have a network of at least two PBC running inside a slice of thickness d_{hkl}. Due to presence of the PBCs, this faces more likely add BUs along their edges than over them. The PBC also stabilizes the already formed face. We consider the first four strongest PBC, based on nearest-neighbours interactions.
Let's start with the strongest PBC, the one running along [101]. Projecting the structure along this direction, the projection of any other PBC represents an F form (Fig.4.9). In this way we can see all F faces belonging to the zone [101]. PBC2 [111] (orange) gives with PBC1 [101] a network parallel to plane (10$\bar{1}$), that corresponds to the first F form {10$\bar{1}$}. PBC3 [001] (yellow) with PBC1 defines form {010}, PBC4 [211] (purple) defines form {$\bar{1}$11}. These are the long side forms of the experimental prismatic morphology.

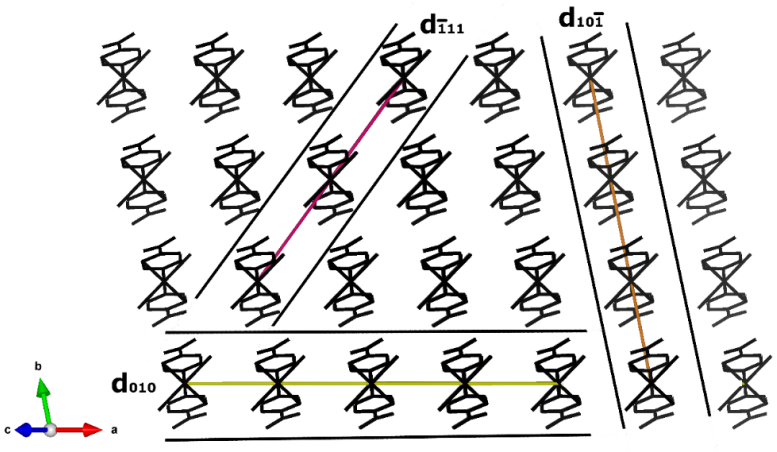

Figure.4.9 Projection of the structure along [101] axis. The figure shows PBCs [111] (orange), [001] (yellow), [211] (purple). The F forms and their thickness are reported.

Using the same approach, we analysed zone [111], projecting the structure along PBC 2 direction (Fig.4.10). Obviously, PBC1 [101] identifies form $\{10\bar{1}\}$. PBC3 and PBC4 in this zone define faces $(\bar{1}10)$ and $(0\bar{1}1)$. These faces cap the prismatic morphology.

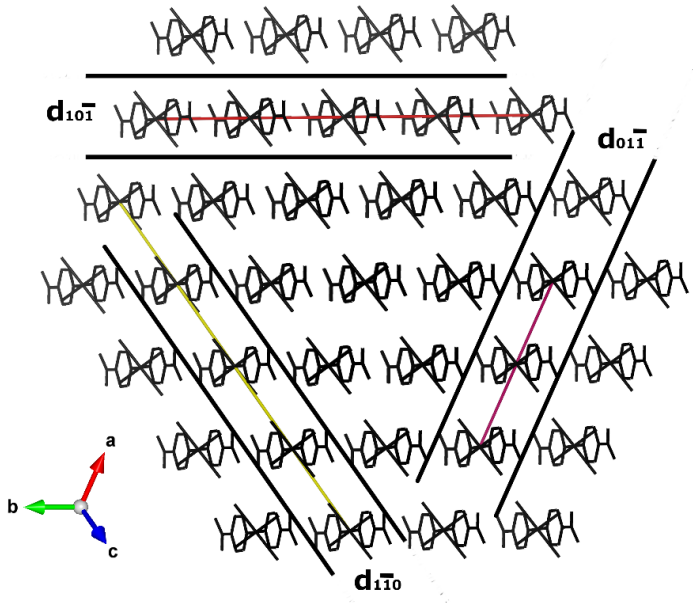

Figure.4.10 Projection of the structure along [111] the direction. The figure shows PBCs [101](red), [001](yellow), [211](purple). The F forms and their thickness are reported.

Projecting the structure along PBC3 [001] (Fig.4.11), we can identify the F form $\{\bar{1}20\}$, that is the last one defined by the first group of PBC. This approach is still qualitative, but we have already identified all the experimentally observed forms using only the first four PBC. The only exception is form (001), that is a K form. Using all the 18 PBC we identified other 84 face F, in this case we calculated the dot product of any PBC couple to identify potential F faces. None of these PBC is parallel to form {001} which results definitively a K face.

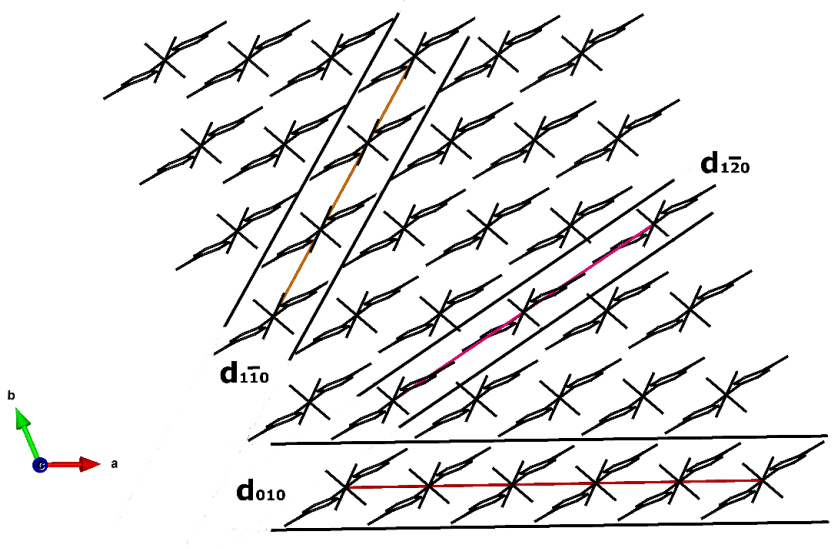

Figure.4.11 Projection of the structure along [211] axis. The figure shows PBCs [101] (red), [111] (orange), [001] (yellow). The F forms and their thickness are reported.

The importance for the morphology of the forms has to be evaluated from an energetic point of view. Firstly, we calculate for each of them their attachment energy value, from which we draw the growth morphology (Fig.4.12), considering the direct relation between attachment energy and grow rate. Secondly, we calculate the surface tension and, applying the Wulff construction, we draw the equilibrium morphology (Fig.4.12A). Both the habits consist of a prism bounded by forms {10$\bar{1}$}, {010}, {$\bar{1}$11} and capped by forms {01$\bar{1}$} and {1$\bar{1}$0}.
The following Table (Tab.4.6) reports the calculated values for the forms that are relevant for both the experimental and simulated habits. We also report the value for faces ($\bar{1}$20), that is the only F face identified using the first four PBC not experimentally observed, and (001), that is the only observed face not predicted by the HP approach.

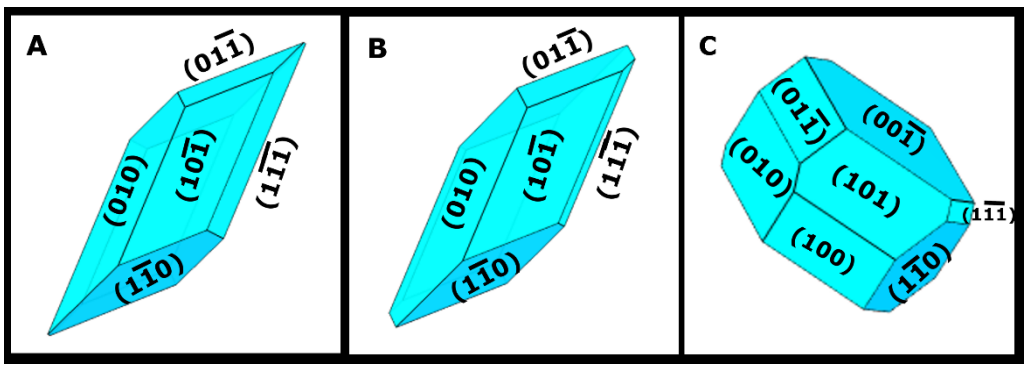

Figure 4.12. Simulated morphologies. Adopting HP approach, we calculated the equilibrium morphology (A) and the growth morphology (B). FBDH habit (C).

Form	Character	A_{mesh}^{hkl} (Å)	z	E_{att}^{hkl} (kJ/mole)	γ_{hkl} (N/m)
$\{010\}$	F	56,225	1	-102,1	0,302
$\{10\bar{1}\}$	F	62,407	1	-118,4	0,315
$\{1\bar{1}0\}$	F	66,638	1	-147,0	0,366
$\{\bar{1}11\}$	F	75,371	1	-152,6	0,336
$\{01\bar{1}\}$	F	60,277	1	-216,0	0,595
$\{\bar{1}20\}$	F	106,28	2	-275,2	0,860
$\{001\}$	K	41,555	1	-781,1	3,115

Table 4.6 The attachment energies and the specific surface energies for experimental or theoretical relevant forms.

Discussion and conclusions

The solubility of the system in water is low. Concentrations around 5mM for both the reagents are already far from the equilibrium, and crystal nucleation and growth occurs. During our experiments, we increased of the same amount the concentrations of both the reagents. Nevertheless, the effect on solubility is different because, following elementary mass law, solubility is very sensible to Iso concentration. The mere number of obtained crystals confirm that we quickly moved from a slow growth of large crystals (Fig.4A) to a sudden precipitation of numerous small individuals (Fig.5.4 C and D). At low concentrations, the most important habit is the prismatic one, but increasing concentrations the most common habits are platelet like. It is important to note that no clear effect on crystals habit was observed modifying the reagent ratio, which means that no large importance should be given to face poisoning from the reagents themselves. The relative importance of all the faces change moving from platelet habit to prismatic habit The more important modifications are: the shrinking of forms $\{10\bar{1}\}$ and $\{01\bar{1}\}$, the disappearance of form $\{001\}$, the appearance of forms $\{\bar{1}11\}$ and $\{1\bar{1}0\}$.

For crystals grown from gel media the importance of face (001) is negligible and the prismatic habits is almost the only observed one. This behaviour may confirm that the crystals growth process occurs in an environment dominated by slow diffusion, where the growing crystal creates around itself a low concentration of the reagents, very near to the conditions where we observed in solution the precipitation of prims. That is what is commonly presumed for this kind of experiments.

Let's compare our simulations with the prismatic habit. From this point of view, our results (Fig.5.12A and B) show a very good proximity with experimental outputs (Fig.5.3A). The result obtained using HP approach is particularly similar if we compare it with results obtained from BFDH method.

BFDH calculated habit is loosely related with any of the experimental outputs. This habit is based on the geometry and the symmetry of the unit cell, and gives large importance to the longest axis [001]. This fact confirms that the presence of strong anisotropy in the interactions, as hydrogen bonds, brings to large deviation from habits calculated exclusively from geometric parameters. This last approach relies on the assumption of little anisotropy in the interaction displayed by a BU with the surrounding ones.

The number of identified PBCs (18) is large (tab.5.4). However, only a reduced amount of four PBCs is necessary to classify the observed faces. The remaining 14 PBC identify a large group of 84 faces that has no relevance for neither experimental output nor the simulated habit. A clear-cut based on the nature of the interactions divides the two groups of PBCs. On one side, the first group is composed by the PBCs showing the strongest ECE (tab.5.4) and each PBC is built using short-range intermolecular interactions as hydrogen bonds. On the other side, the interactions are based exclusively on coulombic interactions and no short contacts can be traced. The large number of interactions and PBC can be attributed to the long range at which electrostatic interaction can still work effectively.

A large amount of morphology predictions adopting HP method were performed on organic molecules. Simulations were performed on a wide range of systems, from aromatic compounds[23,24] to polar amides and carboxylic acids [19]. For all these cases long range contribution from electrostatics were not considered, relying exclusively on short range interaction to define PBCs. Certain amounts of predictions were performed on inorganic ionic salts as minerals[25–27]. Also for these cases the purely coulombic interaction between distant BU was not considered for the building of PBCs, even if it plays a crucial role for the determination of a parameter as attachment energies.

From these considerations, we conclude that is reasonable to avoid the use of PBC based exclusively on coulombic interactions, and consider only the nearest neighbours for PBCs identification.

PIXEL approach for energetic calculation, associated with structure inspection, is a powerful tool to identify the presence of the appropriate interactions.

All the faces observed during experiments were identified as F faces. The only exception is form $\{001\}$. This form is a K form, the most thermodynamically an kinetically unstable kind. However, this is interesting if we consider its sensibility respect to the crystallization environment.

Form $\{\bar{1}11\}$ is exclusively present in the prismatic habit. The calculation of both growth and equilibrium morphology can bring some light on the behaviour of this form.

Attachment energy for form $\{11\bar{1}\}$ is 50% larger than the value for face (010), but considering surface energy the difference is limited (6%), reflecting its absence during growth and sudden appearance. This form is peculiar because form $\{11\bar{1}\}$ is defined by PBC 1 (101) and PBC 4 (211). The energy difference between the two ECE is large (Tab.5.4), so it can be considered as a sort of S faces. Any S faces can be seen as consist of parts of adjacent F-faces[15], in this case forms {010} and $\{10\bar{1}\}$ (Fig.5.9). The S faces can appear if its growth rate is comparable to the growth rate of the two F forms. However, if it is faster or one the two F forms growth rate is slow due to the experimental conditions, its appearance is impossible.

For form $\{01\bar{1}\}$ we can find suggestions of a similar behaviour. Its surface energy is 61% larger than the surface energy of form $\{1\bar{1}0\}$, but its attachment energy is 47% larger. Again, during growth process face $\{01\bar{1}\}$ is expected to show an larger area than in the equilibrium morphology.

For our systems, has to be considered that all the experiments were performed inside water media or silica gel, which are polar environments with large dielectric constants. Inside the crystalline material coulombic interactions remain crucial for the stability, but their ability to attract and bind BU from the solution is limited. On the other side, all calculations were performed *in vacuo*, enhancing the importance of these interactions. Considering this hypothesis, we suggest as an another consequence that the driving force for the addiction of the BU should be the formation of hydrogen bonds between solvated BU and the growing crystals.

Hydrogen bonds inside structure always implies a negatively charged carboxylic group acting as acceptor and a water molecule acting as donor. Apart from form $\{\bar{1}01\}$, all the other faces expose carboxylate groups toward the solution, so the new BUs interact with the negatively charged groups already present over the surface. The most common form of INA inside aqueous solutions is zwitterionic (pKa_1: 1.70, pKa_2: 4.95)[28]. It is reasonable to assume that INA ligand poisoning effect is inhibited by the electrostatic repulsions exerted on it. In this way we can justify the absence of clear effect of face poisoning by the reagents.

Form {001} surface consists of complexes exposing their carboxylic groups (fig.2F). It shows a layer of tightly packed carboxylic groups while copper ions are hidden below them, so on this face the previously described effect should be maximised. This creates a not negligible kinetic barrier respect to the insertion of new BUs. This kinetic effect can be relevant when precipitation is sudden (high concentration wells), but becomes far less important when the faces form slowly (gel media, low concentration).

As previously suggested form $\{\bar{1}01\}$, the most important for non-equilibrium habits, is unique. In fact, it hasn't any carboxylic group exposed towards the solution (fig.8 and 9). BUs add over it through an hydrogen bond with a non-charged water molecule, as reflected by the fact that this face is the only one parallel both to PBC 1 and 2 (fig.6). This means that on this surface there's no kinetic barrier inhibiting poisoning from zwitterionic isonicotinate ligand. Probably the extent of such poisoning is so important to be present in all the samples, so no large modification came from variation of the reagents ratio. Instead, inside silica gel pH value is lower (pH = 5) due to the acidity of the environment. This could move the Iso equilibrium towards the protonated acid, so it can display less tendency to poison this form respect to the others.

Supporting information

Calculated parameter for all the considered forms

character	form	$A_{mesh}^{(hkl)}$	z	$E_{att}^{(hkl)}$	γ_{hkl}
F	{$\bar{1}$00}	62,5	1	-399	1,06
F	{0$\bar{1}$0}	56,2	1	-102,1	0,30
F	{1$\bar{1}$0}	66,6	1	-147	0,37
F	{110}	98,5	1	-333,1	0,56
F	{$\bar{1}$01}	62,4	1	-118,4	0,31
F	{01$\bar{1}$}	60,3	1	-216	0,59
F	{011}	78,4	1	-535,8	1,14
F	{$\bar{1}$11}	75,4	1	-152,6	0,34
F	{$\bar{1}\bar{1}$1}	91,8	1	-182,9	0,33
F	{$\bar{1}$1$\bar{1}$}	81,6	1	-495,2	1,01
F	{120}	147,7	2	-319	0,72
F	{$\bar{1}$20}	106,3	2	-275,2	0,86
F	{$\bar{2}$10}	116,4	2	-314	0,90
F	{10$\bar{2}$}	85,6	2	-429	1,66
F	{20$\bar{1}$}	117,8	2	-541,4	1,53
F	{0$\bar{1}$2}	86,9	2	-522,3	1,99
F	{0$\bar{2}\bar{1}$}	129,9	2	-534,7	1,37
F	{1$\bar{1}\bar{2}$}	101,9	2	-456,7	1,49
F	{11$\bar{2}$}	103,0	2	-231,8	0,75
F	{$\bar{1}$21}	117,4	2	-189,3	0,54
F	{$\bar{1}$2$\bar{1}$}	110,7	2	-246,3	0,74
F	{$\bar{1}\bar{2}$1}	138,9	2	-186,3	0,45
F	{$\bar{1}\bar{2}\bar{1}$}	166,7	2	-461,9	0,92
F	{$\bar{2}$11}	114,2	2	-231,8	0,67
F	{21$\bar{1}$}	145,1	2	-403,9	0,92
F	{$\bar{1}\bar{2}$2}	142,2	2	-417,3	0,97
F	{$\bar{1}$22}	140,5	2	-421,5	1,00
F	{$\bar{1}$2$\bar{2}$}	129,1	2	-437,4	1,13
F	{$\bar{2}$12}	126,4	2	-182,6	0,48
F	{$\bar{2}\bar{1}$2}	146,6	2	-184,1	0,42
F	{$\bar{2}\bar{2}$1}	185,8	2	-452,1	0,81
F	{2$\bar{2}\bar{1}$}	136,1	2	-521,5	1,27
F	{$\bar{2}$2$\bar{1}$}	143,0	2	-496,7	1,15
F	{$\bar{1}$30}	156,4	3	-295,7	0,94
F	{$\bar{1}$03}	119,3	3	-568,5	2,37
F	{$\bar{2}$30}	168,3	3	-291,4	0,86
F	{$\bar{1}$13}	136,1	3	-520,3	1,90
character	form	$A_{mesh}^{(hkl)}$	z	$E_{att}^{(hkl)}$	γ_{hkl}
F	{$\bar{1}\bar{1}$3}	127,5	3	-380,9	1,49
F	{$\bar{1}$3$\bar{1}$}	217,9	3	-460,4	1,05

F	$\{31\bar{1}\}$	203,7	3	-416,5	1,02
F	$\{\bar{3}11\}$	168,0	3	-418,4	1,24
F	$\{12\bar{3}\}$	156,9	3	-237,7	0,75
F	$\{\bar{1}23\}$	170,7	3	-464,5	1,36
F	$\{1\bar{3}\bar{2}\}$	188,2	3	-423,6	1,12
F	$\{21\bar{3}\}$	159,3	3	-234,9	0,73
F	$\{2\bar{1}\bar{3}\}$	149,7	3	-362,3	1,21
F	$\{23\bar{1}\}$	233,1	3	-436,6	0,93
F	$\{3\bar{1}\bar{2}\}$	171,5	3	-233,9	0,68
F	$\{3\bar{2}\bar{1}\}$	176,2	3	-235,7	0,67
F	$\{\bar{3}\bar{2}1\}$	240,0	3	-421,5	0,87
F	$\{3\bar{2}1\}$	191,0	3	-448,5	1,17
F	$\{\bar{3}22\}$	183,1	3	-442,7	1,20
F	$\{2\bar{3}2\}$	186,2	3	-445,4	1,19
F	$\{\bar{1}3\bar{3}\}$	184,2	3	-432,4	1,17
F	$\{13\bar{3}\}$	198,2	3	-404,8	1,02
F	$\{1\bar{3}\bar{3}\}$	214,7	3	-455,5	1,06
F	$\{2\bar{3}\bar{3}\}$	211,4	3	-430,1	1,01
F	$\{11\bar{4}\}$	159,2	4	-471,2	1,97
F	$\{4\bar{1}\bar{1}\}$	226,3	4	-427,3	1,25
F	$\{\bar{2}\bar{1}4\}$	180,9	4	-397	1,46
F	$\{\bar{2}14\}$	179,6	4	-436,9	1,62
F	$\{1\bar{4}\bar{2}\}$	239,6	4	-420,3	1,16
F	$\{1\bar{4}2\}$	210,5	4	-345,7	1,09
F	$\{\bar{1}\bar{4}\bar{2}\}$	292,3	4	-461,6	1,05
F	$\{\bar{1}\bar{4}2\}$	241,7	4	-390,1	1,07
F	$\{42\bar{1}\}$	297,5	4	-439,2	0,98
F	$\{3\bar{1}\bar{4}\}$	205,4	4	-410,7	1,33
F	$\{34\bar{2}\}$	322,1	4	-427,4	0,88
F	$\{\bar{4}\bar{1}3\}$	259,1	4	-415,8	1,07
F	$\{3\bar{4}\bar{2}\}$	246,4	4	-345,2	0,93
F	$\{3\bar{4}2\}$	248,0	4	-438,9	1,18
F	$\{\bar{2}\bar{3}4\}$	241,9	4	-385,7	1,06
F	$\{12\bar{5}\}$	209,1	5	-450,5	1,79
F	$\{2\bar{1}\bar{5}\}$	213,5	5	-472,9	1,84
F	$\{\bar{3}25\}$	248,3	5	-437,1	1,46
F	$\{\bar{4}\bar{3}5\}$	334,8	5	-415,9	1,03
F	$\{31\bar{5}\}$	238,8	5	-423,3	1,47
F	$\{2\bar{5}4\}$	291,3	5	-448,2	1,28
F	$\{1\bar{5}\bar{3}\}$	314,5	5	-456,9	1,21
character	form	$A_{mesh}^{(hkl)}$	z	$E_{att}^{(hkl)}$	γ_{hkl}
F	$\{3\bar{5}\bar{4}\}$	326,5	5	-434,2	1,10
F	$\{\bar{4}52\}$	307,4	5	-418,2	1,13
F	$\{5\bar{1}\bar{3}\}$	284,5	5	-417,5	1,22
F	$\{5\bar{2}\bar{1}\}$	282,1	5	-425	1,25
F	$\{5\bar{3}\bar{4}\}$	307,6	5	-403,4	1,09

F	$\{5\bar{4}\bar{2}\}$	308,6	5	-402,3	1,08
F	$\{21\bar{6}\}$	240,4	6	-455,7	1,89
F	$\{\bar{2}\bar{5}6\}$	353,0	6	-415,1	1,17
F	$\{1\bar{6}3\}$	316,4	6	-412,9	1,30
F	$\{1\bar{6}\bar{3}\}$	367,2	6	-453,2	1,23
F	$\{16\bar{3}\}$	348,2	6	-419,4	1,20
F	$\{5\bar{6}\bar{3}\}$	380,3	6	-415,2	1,09
F	$\{6\bar{2}\bar{1}\}$	340,0	6	-437,3	1,28
F	$\{3\bar{1}\bar{7}\}$	295,4	7	-463	1,82
K	{001}	41,6	1	-781	3,12

Bibliography

1. Thomas, J. & Ramanan, A. Growth of Copper Pyrazole Complex Templated Phosphomolybdates: Supramolecular Interactions Dictate Nucleation of a Crystal. *Cryst. Growth Des.* **8,** 3390–3400 (2008).
2. Moret, M. & Rizzato, S. Crystallization Behavior of Coordination Polymers. 2. Surface Micro-Morphology and Growth Mechanisms of {[}Cu(bpp)(3)Cl-2]center dot 2H(2)O by in Situ Atomic Force Microscopy. *Cryst. Growth Des.* **9,** 5035–5042 (2009).
3. Carlucci, L., Ciani, G., Moret, M., Proserpio, D. M. & Rizzato, S. Monitoring the Crystal Growth and Interconversion of New Coordination Networks in the Self-assembly of MCl 2 Salts (M = Co, Ni, Cu, Cd) and 1,3-Bis(4-pyridyl)propane. *Chem. Mater.* **14,** 12–16 (2002).
4. Carlucci, L. *et al.* Crystallization behavior of coordination polymers. 1. kinetic and thermodynamic features of 1,3-Bis(4-pyridyl)propane/MCl2 Systems. *Cryst. Growth Des.* **9,** 5024–5034 (2009).
5. Semenov, A. *et al.* Controlled Arrangement of Supramolecular Metal Coordination Arrays on Surfaces. *Angew. Chemie Int. Ed.* **38,** 2547–2550 (1999).
6. Surin, M., Samorì, P., Jouaiti, A., Kyritsakas, N. & Hosseini, M. W. Molecular Tectonics on Surfaces: Bottom-Up Fabrication of 1D Coordination Networks That Form 1D and 2D Arrays on Graphite. *Angew. Chemie* **119,** 249–253 (2006).
7. THOMPSON, C. *et al.* Using microscopic techniques to reveal the mechanism of anion exchange in crystalline co-ordination polymers. *J. Microsc.* **214,** 261–271 (2004).
8. Carlucci, L., Ciani, G., Moret, M., Proserpio, D. M. & Rizzato, S. Polymeric Layers Catenated by Ribbons of Rings in a Three-Dimensional Self-Assembled Architecture: A Nanoporous Network with Spongelike Behavior. *Angew. Chemie Int. Ed.* **39,** 1506–1510 (2000).
9. Gavezzotti, A. Non-conventional bonding between organic molecules. The 'halogen bond' in crystalline systems. *Mol. Phys.* **106,** 1473–1485 (2008).
10. Maloney, A. G. P., Wood, P. A. & Parsons, S. Intermolecular interaction energies in transition metal coordination compounds. *CrystEngComm* **17,** 9300–9310 (2015).
11. Maschio, L., Civalleri, B., Ugliengo, P. & Gavezzotti, A. Intermolecular Interaction Energies in Molecular Crystals: Comparison and Agreement of Localized Møller–Plesset 2, Dispersion-Corrected Density Functional, and Classical Empirical Two-Body Calculations. *J. Phys. Chem. A* **115,** 11179–11186 (2011).
12. Donnay, J. D. H. & Harker, D. A New Law of Crystal Morphology Extending the Law of Bravais. *Am. Miner.* **22,** 446 (1937).
13. Hartman. in *Crystalg growth: an introduction* 367–401 (1973).

14. Hartman, P. & Perdok, W. G. On the relations between structure and morphology of crystals. I. *Acta Crystallogr.* **8,** 49–52 (1955).
15. Hartman, P. & Perdok, W. G. On the relations between structure and morphology of crystals. II. *Acta Crystallogr.* **8,** 521–524 (1955).
16. Hartman, P. & Perdok, W. G. On the Relations Between Structure and Morphology of Crystals. III. *Acta Cryst* **8,** 525 (1955).
17. Hartman, P. The attachment energy as a habit controlling factor. I. theoretical considerations. *J. Cryst. Growth* **49,** 145–146 (1980).
18. Grimbergen, R. F. P., Bennema, P. & Meekes, H. On the prediction of crystal morphology. III. Equilibrium and growth behaviour of crystal faces containing multiple connected nets. *Acta Cryst (1999). A55, 84-94 [doi10.1107/S0108767398008897]* **55,** 1–11 (1999).
19. Berkovitch-Yellin, Z. Toward an ab Initio Derivation of Crystal Morphology. *J Am Chem Soc* **107,** 8239–8253 (1985).
20. Gavezzotti, A. CLP-PIXEL theory. http://www.angelogavezzotti.it/Public/main2.htm
21. Gilli, P., Bertolasi, V., Ferretti, V. & Gilli, G. Covalent Nature of the Strong Homonuclear Hydrogen Bond. Study of the O-H⋯O System by Crystal Structure Correlation Methods1. *J. Am. Chem. Soc.* **116,** 909–915 (1994).
22. Dunitz, J. D., Gavezzotti, A. & Rizzato, S. 'coulombic compression', a pervasive force in ionic solids. A study of anion stacking in croconate salts. *Cryst. Growth Des.* **14,** 357–366 (2014).
23. Massaro, F. R., Moret, M., Bruno, M. & Aquilano, D. Equilibrium and growth morphology of oligothiophenes: Periodic bond chain analysis of quaterthiophene and sexithiophene crystals. *Cryst. Growth Des.* **13,** 1334–1341 (2013).
24. Massaro, F. R., Moret, M., Bruno, M. & Aquilano, D. Equilibrium and growth morphology of oligoacenes: Periodic bond chains analysis of naphthalene, anthracene, and pentacene crystals. *Cryst. Growth Des.* **12,** 982–989 (2012).
25. Pastero, L., Massaro, F. R. & Aquilano, D. Experimental and Theoretical Morphology of Single and Twinned Crystals of Li2CO3 (Zabuyelite) Linda. *Cryst. Growth Des.* **7,** 2749–2755 (2007).
26. Hartman, P. The attachment energy as a habit controlling factor II. Application to anthracene, tin tetraiodide and orthorhombic sulphur. *J. Cryst. Growth* **49,** 157–165 (1980).
27. Hartman, P. The attachment energy as a habit controlling factor. III. Application to corundum. *J. Cryst. Growth* **49,** 166–170 (1980).
28. Jellinek, H. H. G. & Urwin, J. R. Ultraviolet absorption spectra and dissociation constants of picolinic, isonicotinic acids and their amides. *J. Phys. Chem.* **58,** 548–550 (1954).

IV-Cholesterol crystallization from model lipid bilayers

This project is the result of a kind and fruitful collaboration with PhD student Neta Varsano, at prof Lia Addadi laboratory, department of structural biology, Weizmann Institute of Science, Rehovot, Israel (IL)

Introduction

Cholesterol and atherosclerosis

Cholesterol molecule is a crucial component of cellular membrane [1–3]. In particular, it strongly influence the stability of the membrane and its mechanical properties. These effects came from the different interactions that cholesterol displays with the other membrane lipids, strongly influencing membrane dynamics[4]. Cholesterol is synthetized inside liver and then delivered towards the tissues by the bloodstream. LDL particles are responsible to carry this highly hydrophobic molecule. These vesicles consist of a phosholipidic-proteic membrane filled with cholesterol or its esters [5].

High cholesterol levels in the bloodstream are caused by modified LDL particles that cannot properly deliver their lipid content. trapped in the artery inner layer, these vesicles trigger an immune-system response and are adsorbed by macrophage cells recruited to the area. The macrophage cells accumulate hydrolysed cholesterol in their membrane, becoming the so-called foam cells. Atherosclerotic plaques are formed by the accumulation of dead foam-cell end their lipid content [6].

Atherosclerotic diseases are one of the major death cause in the western world. The rupture of the atherosclerotic plaques triggers intense inflammatory response, while plaque fragments can cause vascular occlusion. It is known that inside mature plaques can be found cholesterol crystals.

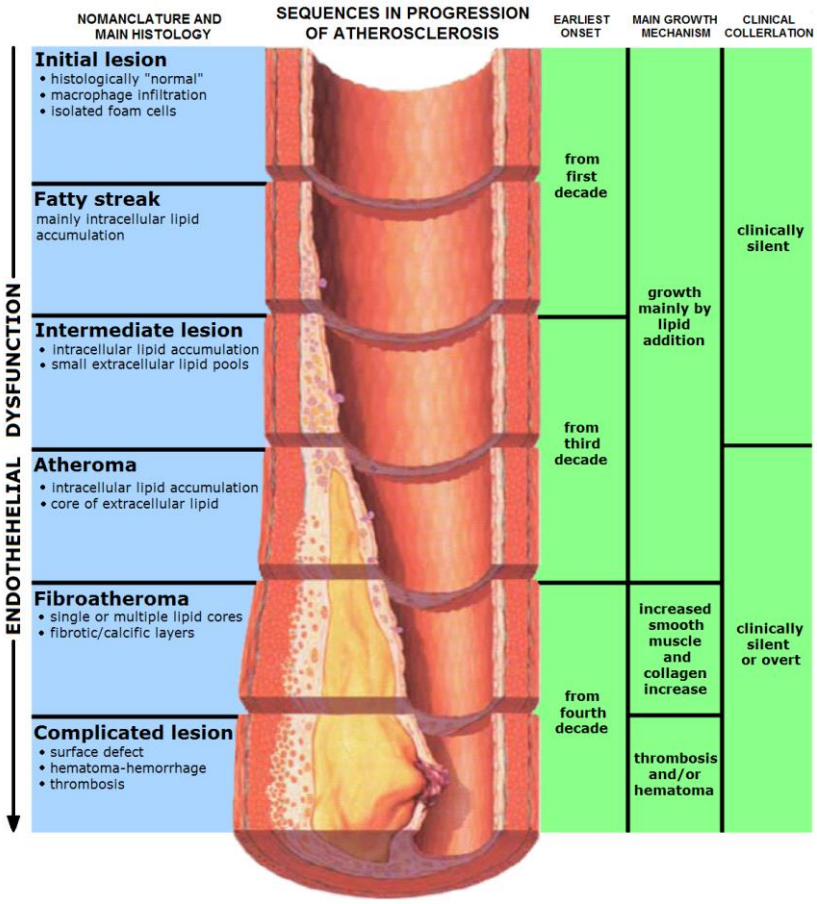

Figure 1. Pathological progression of atheroscheloris

Cholesterol crystallization in lipid bilayer

There is not much information about the process of cholesterol crystal formation and deposition inside plaque, a lipid-rich environment. It is known that inside plaques can be found monohydrate cholesterol forming its triclinic crystals[7]. However, triclinic phase typical morphology is tabular, while inside plaques are often traced fibrous crystals. Analogous fibrous crystal where observed inside bile, in this case cholesterol crystal triggers the formation of the gallbladders. From these studies was observed the ability of cholesterol to form different crystalline materials, from the typical platelet of triclinic monohydrate cholesterol to more unusual material as curved fibres and helices[8].
Lots of observations were performed on the behaviours of cholesterol inside lipid mono and bilayer. A result from this study was the identification of 2D lipid structures called rafts, usually formed by saturated lipids as dipalmitoyl phosphatidylcholine (DPPC) or sphingomyelin (SM), that move inside a liquid 2D phase of unsaturated lipids as palmitoyl oleoyl phosphatidylcholine (POPC) [9].
Rafts are formed by ordered lipid domains. Cholesterol molecules also form ordered lipid domains, sometimes by mixing with other saturated lipids [10]. The formation of mixed cholesterol/lipid domains is related with the miscibility of the cholesterol with the various lipids. For all the cited lipids was identified a concentration threshold above which Cholesterol phase-separates and forms its own raft [11]. Cholesterol rafts are characterized by a rectangular 2D symmetry, not compatible with the already known triclinic structure. Data from GIXD were used to propose a new polymorphic monoclinic stricture for cholesterol monohydrate [11,12]. Recently was discovered a correlation between the presence of such ordered cholesterol domains over the bilayer and the appearance of cholesterol

crystal, asserting that cholesterol 2D ordered domains are actually the nucleation site for 3D cholesterol crystals [13].

The purpose of the project is to study the cholesterol crystallization process over lipid bilayer. In the first place identifying the cholesterol phases that can be obtained, then, adopting super-resolved fluorescence microscopy (STORM method), obtaining more information about nucleation and growth processes. In particular, the role played by the different lipids (POPC, DPPC, SM) in the crystallization process has been investigated.

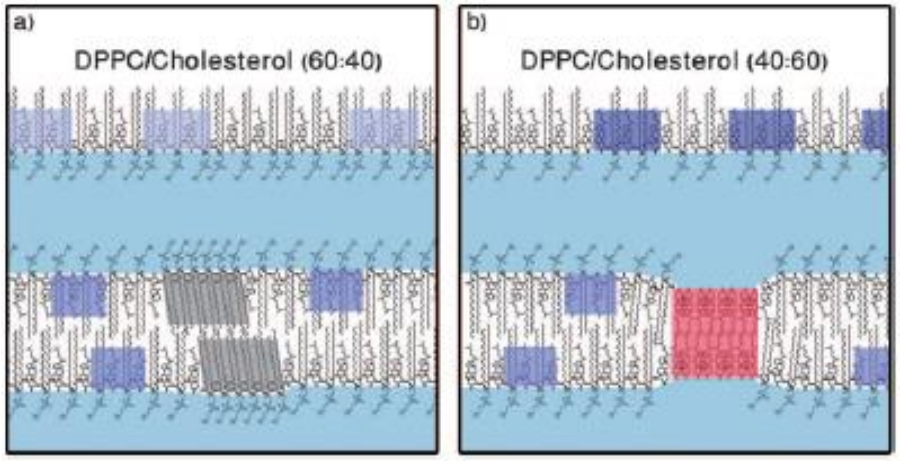

Figure 2. Lipid rafts inside lipid bilayer
Roy Ziblat, Leslie Leiserowitz, and Lia Addadi*
Crystalline Lipid Domains: Characterization by X-Ray diffraction and their Relation to Biology
Angew. Chem. Int. Ed. 2011, **50**, 3620 – 3629

Experimental methods

Bilayer preparation

Lipids bilayer were prepared using vesicles fusion adopting a well-established protocol[13,14]. Vesicles with the desired lipid molar ratios (42:18:40 mol% Chol/DPPC/POPC, 48:12:40 mol% Chol/SM/POPC and 25:75 mol% Chol/POPC) were prepared mixing and drying under nitrogen flux the appropriate amount of chloroform lipids solutions inside a test tube. The resulting lipid film was kept under vacuum at least 15 min and used within 3 days. The day the experiments, we formed a suspension adding 1mL of milliQ-grade water in the tube. To induce the formation of the vesicles, we heated and mixed the suspension three cycles of 3 min each, then we cooled and heated it for five minutes five times. Finally, the suspension was extruded ten times through a polycarbonate membrane with a pore diameter of 0.1 μm (Avanti Polar Lipids). The temperature was higher than lipid transition temperature.

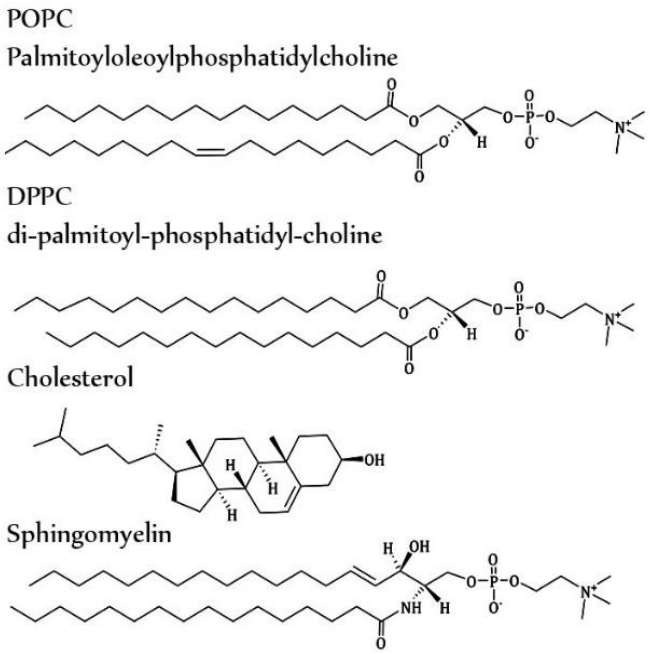

Figure 3. Chemical formulas of the lipids studied

Vesicle suspension (0.14 mg/mL in DDW) was spread on the hydrophilic surface of piranha-cleaned glass slides previously immersed overnight in PEI solution (1000 ppm)[15]. We closed, sealed, and then heated the samples above the lipid transition temperature for 15−20 min, to induce the spontaneous adhesion, rupture and fusion of the vesicles. We wash the samples three times with DDW and we kept them hydrated.

Bilayer feeding

The feeding system consist of two components: a saturated cholesterol chloroform solution (60 μL) placed below a 2.5 mM DDW solution (4mL) of MβCD:cholesterol complex. This complex is a well-known cholesterol carrier[16] that actively brings cholesterol molecules from the chloroform reservoir to the supported lipid bilayer that floats over the solution, placed upside down to keep the bilayer inside the water solution[13].

To prepare MβCD:cholesterol complex solution, in first place we dried under nitrogen flux a chloroform solution containing 0,8 mg of cholesterol inside a 50 mL flask. Then, 33.45 mg of MβCD dissolved in 10 mL of DDW were poured over the cholesterol film. The flask was vortexed for 1 min and then sonicated in a water bath for 1h to dissolve the lipid film. The obtained solutions was incubated overnight in a rotating incubator at 37°. The same day of the experiment, the solution was filtered through a 0.45 Mm syringe filter. Feeding times for the different bilayer are different, and will be later specified. After cholesterol feeding, the coverslip are washed three times with DDW.

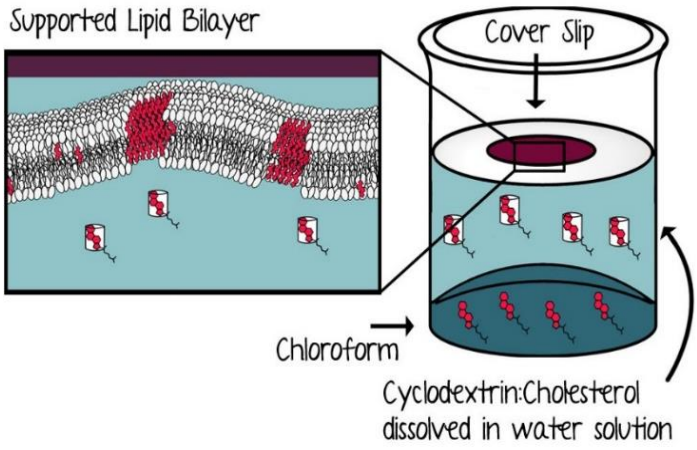

Figure 4. Cholesterol enrichment system. The supported lipid bilayer floats on an aqueous phase containing cholesterol complex. A saturated cholesterol solution in chloroform is placed below the water phase.

Antibody purification

Monoclonal 58B1 antibodies were purified from the supernatant hybridoma fluid by affinity chromatography using an ImmunoPure IgM purification kit according to the manufacturer's instructions. The purified fractions were collected and measured for their UV absorbance at 280 nm. Fractions with optical density higher than 0.2 were collected and dialyzed through Spectra/Por membrane (with cutoff 12000−14000 Da), at 4 °C . The dialysis was performed in 2 L of phosphate-buffered saline (PBS) that was changed three times every 4 hr. The antibodies were used for a maximum of 5 days after purification.

Bilayer labelling

The appearance of cholesterol 2D domains, and subsequently of 3D crystals, was visualized by fluorescently labeled antibody 58B1, using fluorescence microscopy and stochastic optical reconstruction microscopy (STORM). Antibody 58B1

Antibody 58B1 specifically interacts with cholesterol 2D and 3D crystals.[13] The antibody binds to the (0kl) and (h0l) hydrophobic side faces of the cholesterol monohydrate triclinic plates.[13a] STORM, having a lateral resolution of up to 30nm in the xy plane, allows identification of crystal boundaries at the level of single nm-size domains.

Supported lipid bilayers on coverslips were incubated with the antibodies at a concentration of 0.2 µg in 1 mL of DDW containing 5% BSA for 20 min. The samples were washed three times and incubated, for 20 min with fluorescently labeled secondary-antibody. For STORM, Alexa Fluor 647 was used, at a concentration of 0.4 µg/ml. For conventional fluorescence imaging, Rhodamine TRITC was used, at a concentration of 12µg/ml. At the end of the incubation another three washes were perform.

All of the samples in each experimental set were prepared and examined in parallel under the same conditions while keeping the imaging parameters (exposure and signal gain) constant. Each bilayer system was tested at least three times with reproducible results. For each sample, five to seven images were recorded in different areas of the glass, of which average representative images are presented. The samples were then observed by light microscopy (Nikon ECLIPSE E600 POL) or fluorescence microscopy as needed.

TEM microscopy and diffraction

Quantifoil S 7/2 200 mesh gold TEM grids (Quantifoil Micro Tools, Jena, Germany) were glow-discharged for 60 s (EMS glow-discharge apparatus) and then immediately immersed in solutions of 1000 ppm PEI for at least 20 min. Vesicle suspensions were spread on the hydrophilic grid surface to form supported lipid bilayers following the vesicle fusion procedure described above. The grids were then incubated with the cholesterol delivery system. At the end of the incubation, the grids were washed with DDW, blotted, and immediately plunged into liquid ethane (Leica EM-GP plunger, Leica Microsystems). Frozen samples were transferred to a Gatan 626 cryoholder, maintaining the sample temperature below −176 °C inside the microscope. Samples were observed with an FEI Tecnai F-20 transmission electron microscope (FEI Corporation, Hillsboro, OR) operating at 200 kV. Images and diffraction patterns were recorded on a Gatan US4000 CCD camera (Gatan Inc., Pleasanton, CA) using low- dose conditions.

Results and discussion

Labelling of Cholesterol ordered pattern

From previous work we already know that antibody 58B1 recognizes ordered cholesterol patterns, as cholesterol domains inside lipid bilayers.

We purified cholesterol by precipitation of its monohydrate crystals from an oversaturated water/acetone solution. Using this procedure, we can isolate platelets of Cholesterol monohydrate triclinic phase, that can be easily recognized by their interfacial angles (100° and 80°) (Fig.5A). Antibody 58B1 is a monoclonal IgM that specifically binds faces (100) and (010) of the cholesterol crystals. Using the precipitated crystals, we tested its specificity with such cholesterol phase (Fig.5B). The crystals are markedly labelled along their sides. In this way, while we used transmission optical or electron microscopy to identify the cholesterol crystals, we can also use fluorescence microscopy and stochastic optical reconstruction microscopy (STORM) to inspect the formation of cholesterol domains inside the lipid bilayers.

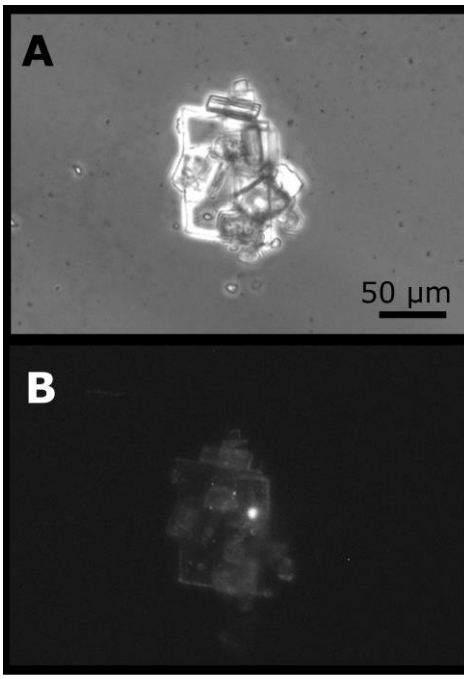

Fig5. Cholesterol monohydrate triclinic crystals. Optical transmission image (A) fluorescenze microscopy after labelling with 58B1 IgM (B)

Cholesterol crystallization over lipid bilayer

We perform crystallization experiments over three different kinds of bilayer: Chol/POPC (25:75 mol%); Chol/DPPC/POPC (42:18:40 mol%) and Chol/SM/POPC (48:12:40 mol%). We always fed bilayer already saturated with cholesterol, that means presence of cholesterol ordered domains phase separated from the other lipids. In a previous work [13] was already demonstrated the importance of such domains as nucleation sites for cholesterol crystals. The composition of the bilayer is related with the low cholesterol solubility in unsaturated lipids as POPC and its growing solubility inside saturate lipids as DPPC and SM. Crystal are obtained over SM-containing bilayers after 2h, while 3-3.5 h are requested by POPC or DPPC – containing bilayers.

The different lipid compositions strongly influenced the crystallization output. The effect of the different lipids wll be later investigated. Briefly, Over POPC and SM containing bilayers we observed the formation on small platelet crystals which habit is typical of the triclinic phase. Some difference is visible in their distribution. Over POPC they are randomly scattered over the surface, while over SM the are more often aggregate along stripes. Instead, over DPPC containing bilayer, we found a various population of crystals. Their morphologies move from the well-know quadrilateral platelets to unprecedently seen pseudo-hexagonal platelet, fibres and curved fibres (Fig.11).

The DPPC bilayers was also prepared over a coated gold grid, fed and inspected using electron microscopy and electron diffraction. The quadrilateral platelets were confirmed to be constituted by the triclinic phase on monohydrate cholesterol, their diffraction reveals the expected triclinic pattern with reticular parameter a and b equal to 12.5 (Fig.6).

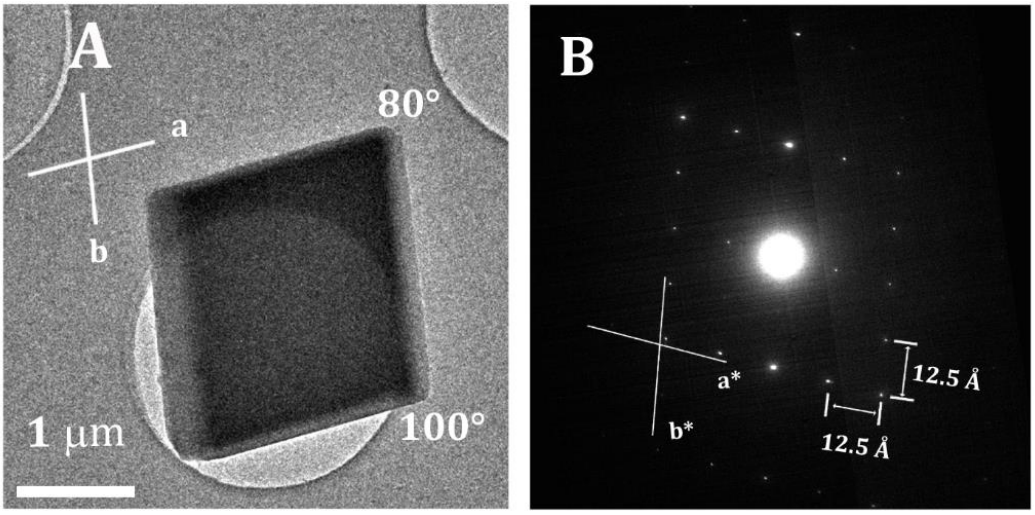

Figure 6. Cryo-TEM image of a cholesterol monohydrate crystal, crystal axis and interfacial angle are reported (A). Cryo-ED pattern of the crystal presented in (A), demonstrating the classic triclinic cholesterol monohydrate diffraction pattern on the [001] zone axis (B).

The hexagonal platelets (Fig.7A) diffraction shows an higher symmetry (rectangular) pattern, incompatible with the triclinic symmetry (Fig.7B). The lattice parameters values are 10 and 5.7 Å. These parameters are the same of the reported monoclinic phase as identified over ceramide/cholesterol bilayer. This means that over DPPC bilayer we can isolate crystals of the monoclinic monohydrate cholesterol phase (Fig.7).

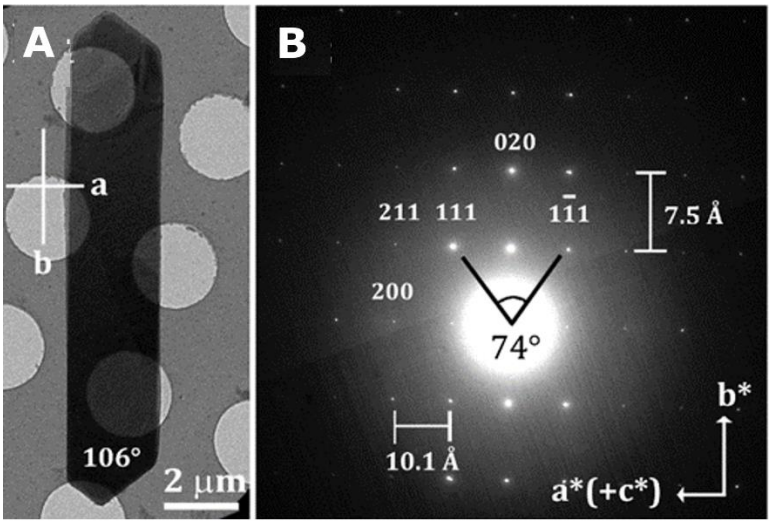

Figure 7. Cryo-TEM image of a cholesterol monohydrate crystal, crystal axis and interfacial angle are reported (A). Cryo-ED pattern of the crystal presented in (A), demonstrating the monoclinic cholesterol monohydrate diffraction pattern on the [001] zone axis (B)

The fibres, inspected using electron microscopy, appear as not homogenous. Their borders show higher contrast than the central part. They also revealed to be flexible, we found them bended or twisted (Fig.8A$_1$). Their diffraction pattern is characterized by the presence of groups of spots sitting on parallel lines. The spacing between the lines is related to a 7.5 Å spacing in the real space (Fig.8A$_2$). This spacing lay over a direction that is parallel to the main axis of the fibers.

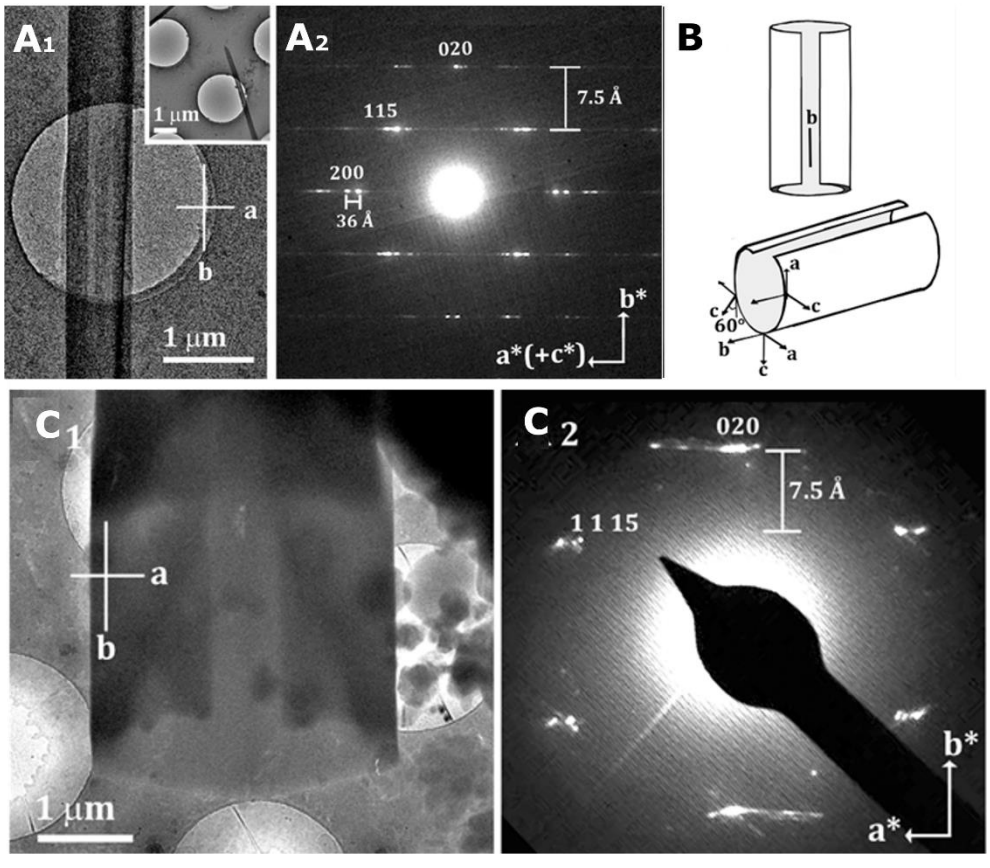

Figure 8. Cryo-TEM transmission image of a cholesterol monohydrate fibrous crystal (A$_1$) (inset in figure A), crystal axis are reported. (A$_2$) Cryo-ED pattern of the crystal presented in (A). (B) Proposed model to justify the image and the diffraction of crystal in figure A. Cryo-TEM image (C$_1$) and diffraction (C$_2$) of a cholesterol crystal grown from a murine cell following incubation with acLDL for 48 h.

We propose that the fibres are crystals of the monoclinic phase of cholesterol monohydrate. Considering the transmission image, we can describe them as platelet wrapped along their b axis (Fig.8B). Due to this peculiar morphology, we cannot observe the regular 10 Å spacing related to the a axis. In fact, in our hypotheses, the orientation of this axis varies continuously respect to the electron beam perpendicular to the bilayer. However, along the walls of the tube, the long c axis of the cell is perpendicular to beam, and we can see a group of spots because in the diffraction space the planes are very narrow along c*.
Interestingly, considering cholesterol crystal grown from murine macrophage cell fed by LDL particles in different project by Varsano et al., we observe the formation of crystals with the same tubular morphology and an analogous diffraction pattern. This result tells us that the crystallization of monoclinic monohydrate cholesterol and the peculiar morphology of its crystals could play a crucial role also in biological environments.

Cholesterol domains in saturated lipid bilayers

In a previous work was shown the strong correlation between the presence of ordered cholesterol domains in the lipid bilayer and the nucleation and growth of cholesterol crystals over it. Cholesterol crystalline domains are tens of nanometers in size, way below the diffraction limit of light. Using mAb 58B1 we were able to detect by conventional fluorescence the relative degree of labelled bilayers containing cholesterol crystalline domains. Many questions remained unanswered regarding the real distribution of cholesterol crystalline domains in the bilayer and their direct association to the formed 3D crystals. We therefore developed a protocol for labelling supported lipid-bilayers with mAb 58B1 coupled with photo-switchable chromophores that allow localization of the domains inside the bilayer using STORM with tens of nanometer resolution. Another potential advantage using STORM is the ability to reconstruct the 3D topology of the bilayer from the super resolution signals in the z direction
For our studies we consider POPC/Chol and POPC/DPPC/Chol bilayers. The use of SM- containing bilayers is problematic because antibody 58B1 has shown some affinity with disordered SM phase.
We always considered as control a bilayer with no cholesterol. For the considered systems this means bilayer compositions 100 mol% POPC, 40:60 mol% POPC:DPPC. In order to avoid any influence of fluorescence decay on the results, all the samples were imaged in parallel under the same conditions, and images were analysed for their average intensity. Some degrees of signal were always collected also from controls. However distinctive differences can be identified.
The fluorescence intensity of bilayers containing cholesterol domains is higher than the intensity arising from unspecific binding of the antibody (Fig. 9I). The parameters of the labelled domains were analysed using the Vutara SRX statistical software (version 6.01.12). The amount of labelled domains in the samples is significantly higher relative to unspecific binding of control samples (Fig.9J). Structural analysis shows that the labelled domains have a collective coverage area ranging between 2.5-16% in the sample, relative to <1% in the control (Fig.9K). Large clusters in the bilayers of Chol/DPPC/POPC and Chol/POPC have sharp edges and a square shape (Fig.9B and F, insets, respectively). The small domains (<100 nm) in the Chol/DPPC/POPC bilayer account for 52% of the overall domain population. The larger domains have a size range of 100-200 nm (Fig.9B, inset). Most of the domains (58%) in Chol/POPC bilayers are detected as individual small spots (<100 nm), while the rest of the domains population are clustered within a wider size range than the aggregates in the Chol/DPPC/POPC bilayer, with size ranges of 100-400 nm (Fig.9F, inset, and K).

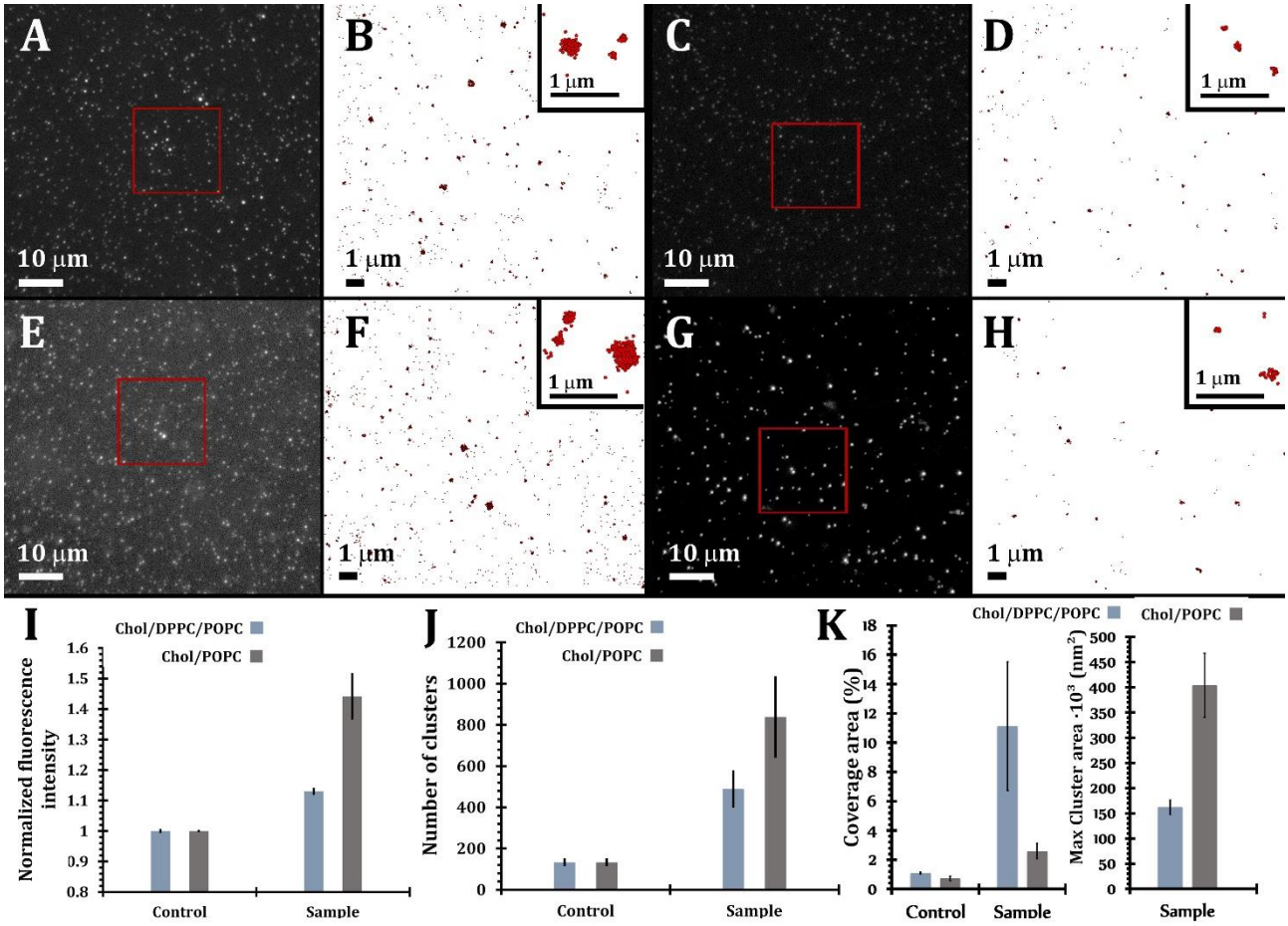

Figure 9. *(A, E): Fluorescence micrographs of 42:18:40 mol% Chol/DPPC/POPC and 25:75 mol% Chol/POPC bilayers, respectively. The bilayer mixtures are above the critical concentration for cholesterol phase separation and are labeled with 58B1 antibody (0.2 μg/mL). (B, F): STORM Localization map of a magnified area (red square) from A and E respectively. (C, G): Fluorescence micrographs of the corresponding control compositions without any cholesterol: (C): DPPC/POPC and (G): POPC. (D, H): STORM Localization map of a magnified area (red square) from C and G respectively. (I): Normalized florescence intensity of the corresponding bilayers. Data were analyzed for the average pixel intensity from the wide field fluorescence images. The fluorescence level for control bilayers was assigned to 1, and the sample measurements were normalized to this level. Data are normalized*

The fluorescent labelling of the considered compositions reveals the presence of structures of tenth of micrometer wide, remarkably different from the more usual scattered foci (Fig.10A and D for DPPC and POPC respectively). Large labelled patches can be found in both the composition and show the presence of region of bilayer composed almost entirely by Cholesterol domains (Fig.10C and E). These patches can be interpreted as the onset of a cholesterol/lipid phase separation. Their presence confirms that in our systems cholesterol concentration is well beyond its solubility limit, justifying the formation of stable cholesterol domains. Their structure tells us the tendency of these domains to cluster together, so they can move inside the bilayer.

Only in the DPPC composition there are aggregations which dimensions range from 5 to 20 μm and that are less dense than the previously discussed patches (Fig.10B). They are formed by aggregation of a limited number of domains. They can be considered as an intermediate step towards the formation of the large patches. Considering them as the nucleation sites of the phase separation. However they are stable at least for hours (the time for the measures) and have never been detected in POPC composition.

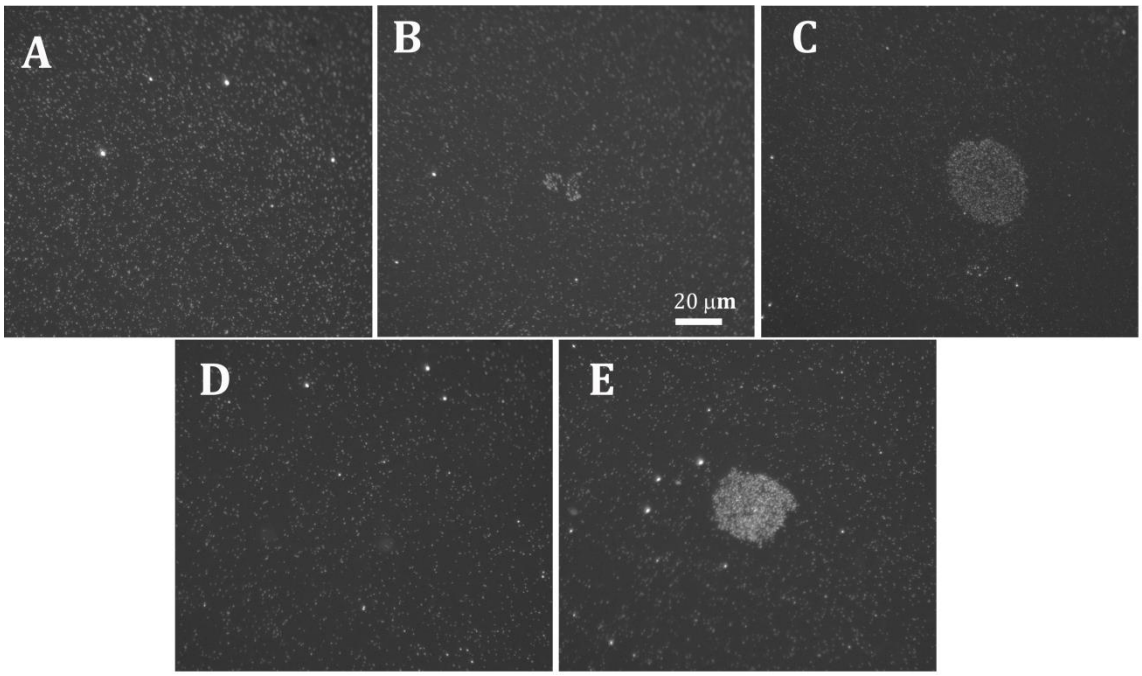

Figure 10. (A,B,C): Fluorescence micrographs of 42:18:40 mol% Chol/DPPC/POPC (70%Chol), labeled with 58B1 antibody (0.2 μg/mL). (D,E) Fluorescence micrographs of 25:75 mol% Chol/ POPC (25%Chol), labeled with 58B1 antibody (0.2 μg/mL).

Cholesterol crystallization over lipid bilayers

The crystallization process was observed over three different bilayers. At first we consider POPC\DPPC\Chol and POPC\Chol composition, in order to compare completely different lipid environments, characterised by the presence of purely unsaturated or saturated lipids. Then we studied how the lipid backbone chemistry can effect crystal growth, by replacing the saturated DPPC with sphingomyelin.

For all bilayers, the cholesterol concentration was above the critical concentration for cholesterol phase separation. These means compositions: 42:18:40 Chol\DPPC\POPC, 27:75 Chol\POPC, 48:12:40 Chol\SM\POPC. The bilayers were kept under water at all times, and fed with cholesterol adopting the previously described system. Bilayers kept inside DDW for the same amount of time were considered as controls, measure were performed the same day to avoid isseus from fluorescence decay.

An increase in the fluorescence intensity was detected for bilayers loaded with cholesterol for 2 hours (Fig.11A_2, B_2, C_2 respectively for DPPC, POPC and SM), compared with control bilayers that were left under DDW (Fig.11A_1, B_1, C_1 respectively for DPPC, POPC and SM) confirming the increase of cholesterol amount inside the bilayers. In all the bilayer we observe formation of cholesterol crystals (Fig.11$A_{3,4}$, $B_{3,4}$, $C_{3,4}$ respectively for DPPC, POPC and SM).

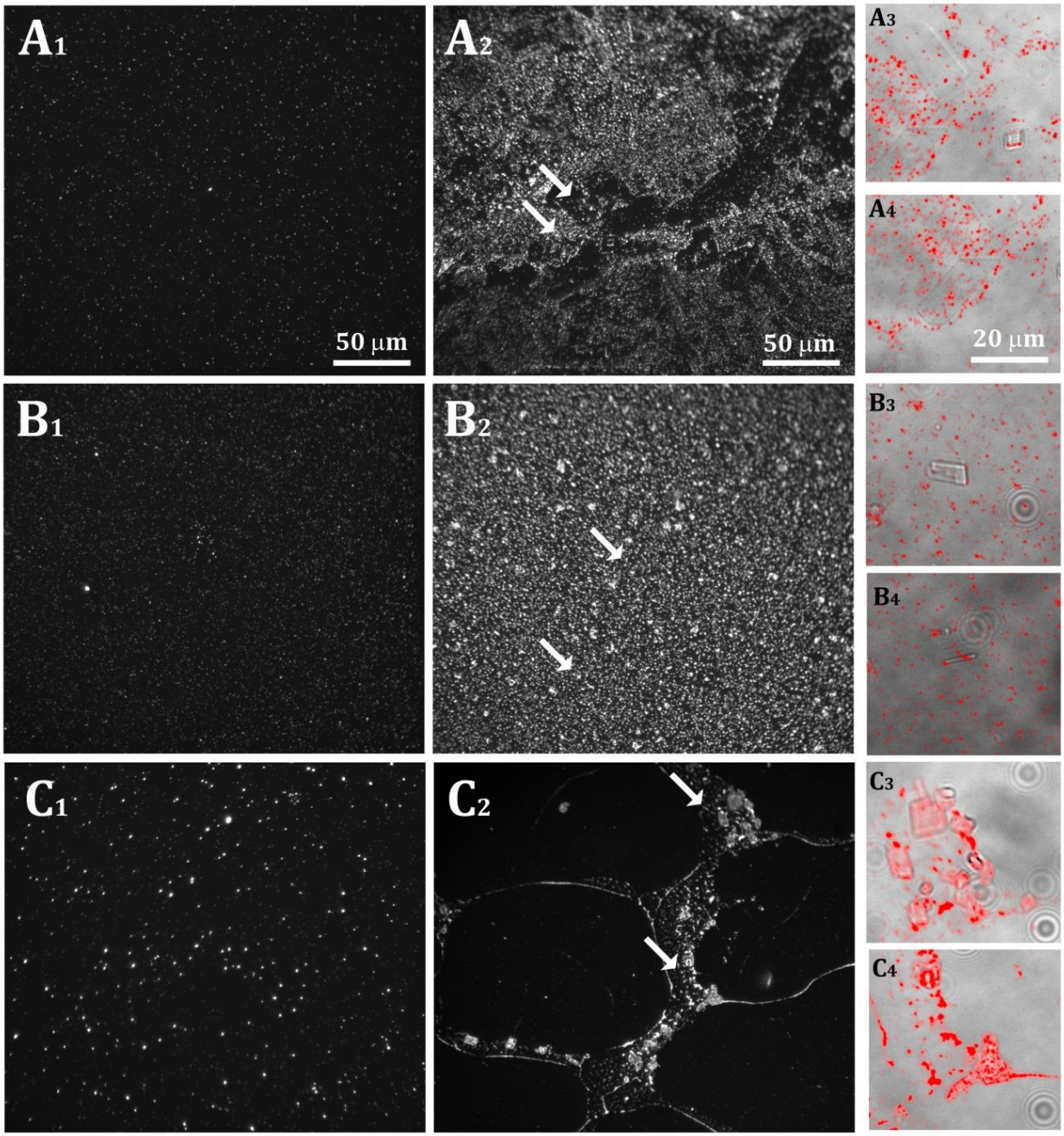

Figure 11. (A) 42:18:40 mol% Chol/DPPC/POPC (70%Chol) after 2h in water (A_1) after 2h incubation with cholesterol (A_2) labelled with 58B1 antibody (0.2 μg/mL). (A_3,A_4) show the bright field image of the areas pointed in image A_2, superimposed with the fluorescence data (red). (B) 25:75 mol% Chol/ POPC (25%Chol) after 2h in water (B_1) after 2h incubation with cholesterol (B_2) labelled with 58B1 antibody (0.2 μg/mL). (B_3,B_4) show the bright field image of the areas pointed in image A_2, superimposed with the fluorescence data. (C) 48:12:40 mol% Chol/SM/POPC after 2h in water (C_1) after 2h incubation with cholesterol (C_2), labelled with 58B1 antibody (0.2 μg/mL). (B_3,B_4) show the bright field image of the areas pointed in image C_2, superimposed with the fluorescence data.

DPPC composition after 2h incubation shows a large increase of the labelling that appear more uniform (Fig.11A_2). However, the intensity of fluorescence shows a little increase. Over the bilayer can be traced large not labelled areas, often related with the presence of triclinic phase platelets that

appears as quadrilateral black holes because labelling is concentrated along the edges (Fi.11A_3). Fibres and platelet of the monoclinic phase instead are less markedly labelled than triclinic phase crystals (Fig.11A_4).
POPC bilayers above cholesterol phase separation threshold displays relatively uniform distribution of sparse labelled domains (Fig.11B_1), while cholesterol enriched bilayers have surfaces covered by densely packed labelling and intense micrometer bright spots (Fig.11B_2, arrows). The bright spots are often indicative of the presence of 3D parallelogram crystals of the triclinic phase (Fig.11$B_{3,4}$) The crystals are labelled mainly along their sides, sometimes some punctuate labelling can be found over their upper surface.
SM bilayer shows intense labelling even if it is not fed with cholesterol, confirming the affinity of the used antibody with disordered SM phase (Fig.11C_1). After feeding, the bilayer shows two different kind of regions. Long filaments and isles intensely labelled side large not labelled pools (Fig11C_2). Exclusively inside the labelled regions, we observed formation of 3D cholesterol crystals with parallelogram plate morphology (Fig.11$C_{3,4}$). The crystals are labelled extensively on their upper surface.
Conventional fluorescence microscopy shows us that domain behaviour is very different and unique for any composition. The application of STORM technique let us see more details. We can identify single fluorophores seeing the structures formed by the ordered domains inside the bilayer and where the crystals are mainly labelled. the positions of the fluorophores along z direction let us see where crystals form and their relation with the lipid bilayer.

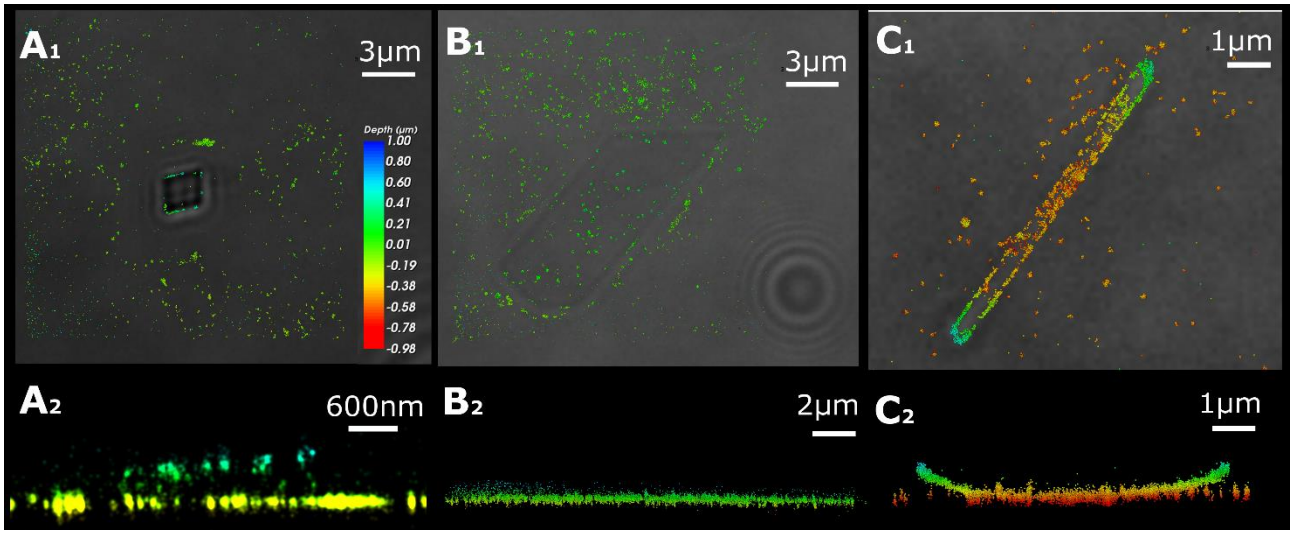

Figure 12. Chol/DPPC/POPC bilayers 42:18:40 mol% after cholesterol enrichment, labeled with 58B1 antibody (0.2 µg/mL). For each crystal is reported the localization map overlayed with the transmission optical image and the projection along z axis of the localization map itself. Triclinic cholesterol platelet (2h feeding) (A); monoclinic cholesterol platelet (2h feeding) (B), monoclinic cholesterol fiber (3.5h feeding) (C)

DPPC bilayer fed with cholesterol shows formation of clustered domains. Cholesterol crystallizes from Chol/DPPC/POPC mixtures forming the triclinic phase platelets (Fig.12A), the monoclinic phase platelets (Fig.12B) and fibres (Fig.12C). The crystals show different labelling. Triclinic phase is scarcely labelled over the upper surface respect to the edges. Often the label over the bilayer forms

straight lines parallels to the crystal edges. The crystals grow mainly over the bilayer (fig12.A_2). Instead, monoclinic platelets are labelled along their edges and over the upper surface, the labelling along the edges is discontinuous. These crystals commonly grow embedded inside the bilayer (Fig.12B_1). After a longer incubation time we observe formation of monoclinic fibres. These fibres are intensely labelled over their upper surface and along their edges (Fig.12C_1). These fibres are bent, and the bended portion come out from the bilayers (fig.12C_2)

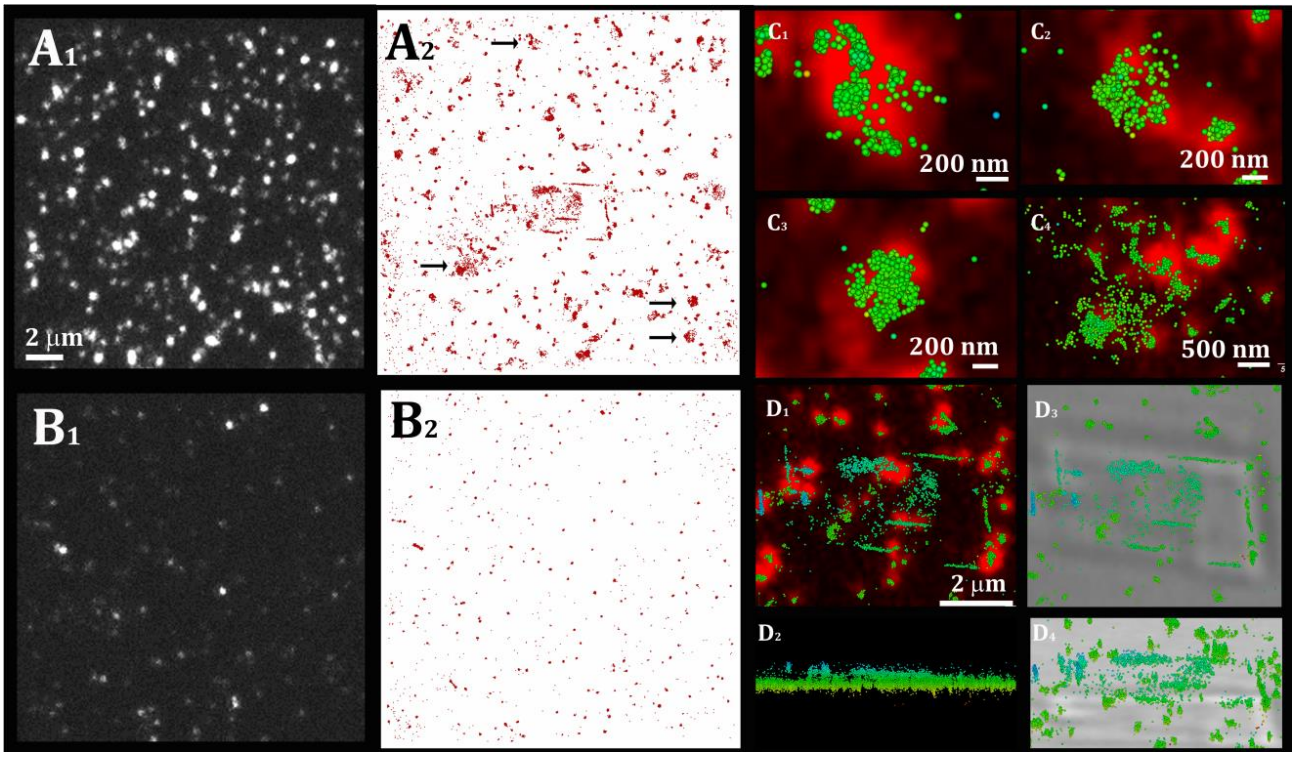

Figure 13. (A): bilayer composition 25:75 mol% Chol/POPC (25%Chol) after 2h incubation with cholesterol, labeled with 58B1 antibody (0.2 μg/mL). (A_1) Fluorescence micrographs, (A_2) Localization map of the resolved super-resolution image of A_1. (B): bilayer composition 25:75 mol% Chol/POPC (25%Chol), labeled with 58B1 antibody (0.2 μg/mL). (B_1) Fluorescence micrographs, (B_2) Localization map of the resolved super-resolution image of B_1 .(C_1,C_2,C_3, C_4) Clusters pointed by arrows in image A_2. (D_1,D_2,D_3, D_4) Localization map of the crystal in image A_2. (D_1) overlayed over fluorescence micrograph (D_2) side wiev (D_3,D_4) overlayed with the bright field image.

Then we studied POPC bilayers. Considering the cholesterol fed bilayer (Fig.13$A_{1,2}$) respect to the bilayer left under DDW (Fig.13$B_{1,2}$), we can see an increase of large domains, resulting from the clustering of little domains. The clustered domains already show sharp edges (Fig.13$C_{2,3}$), resembling the geometry of the triclinic phase crystals, suggesting early formation of ordered triclinic domains. Crystals are labelled along their sides (Fig.13$D_{1,3}$). The projection along z let us see that the crystals are flat and often tilted such that one edge is lifted above the bilayer (Fig.13$D_{2,4}$)

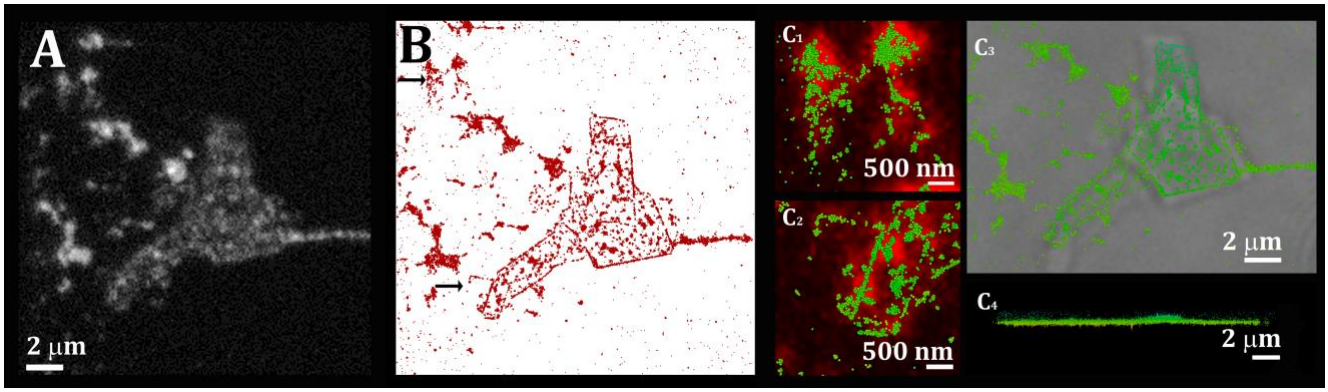

Figure 14. (A): bilayer composition 48:18:75 mol% Chol/SM/POPC after 2h incubation with cholesterol, labeled with 58B1 antibody (0.2 μg/mL). (A) Fluorescence micrographs, (B) Localization map of the resolved super-resolution image of A.(C_1,C_2) overlay of fluorescence micrographs with localization map of pointed areas.(C_3, C_4) Crystals grown inside the bilayer, overlay of optical transmission image and localization map, projection of localization map alog z-axis

Cholesterol crystallizes from Chol/SM/POPC mixtures exclusively inside the highly labelled areas, as large quadrilateral platelet of the triclinic phase. The crystals are intensely labelled over their surface, but localization map (Fig.14B) shows that also in this case the edges uniformly labelled. Crystals are more often embedded inside the bilayer, even if some times they can grow over the bilayer itself (Fig.14C_4). The labelled areas are characterised by the presence of large clusters that often form straight lines, not overlaid with visible 3D crystals, suggesting also in this case, as for POPC composition, an early formation of ordered triclinic domains.

Conclusions

Monoclinic monohydrate cholesterol, an elusive polymorph previously observed in compressed lipid films and in human bile, has been identified over lipid bilayer fed by cholesterol and developed from macrophage cell. Confirming its biological relevance.
Our results on the lipid bilayers show that crystal formation is sensitive to the interaction between cholesterol and the co-lipid POPC, SM or DPPC.
Cholesterol has a very low miscibility (less than 10 mol%) in unsaturated phophatidylcholine, such as POPC. Therefore, almost all the cholesterol content segregates, forming 2D crystalline domains. The STORM localization maps of this composition display a few isolated large domains composed of small spots, surrounded by very small and sparse individual domains.
The two bilayers of Chol/DPPC/POPC and Chol/SM/POPC represent more biologically relevant models as they contain a mixed-ordered phase, where cholesterol can reach high concentrations without segregation.
Indeed, the antibody labelling is higher in Chol/POPC, even though cholesterol concentration is much lower than in Chol/DPPC/POPC bilayers. Since the domains in Chol/POPC reach larger sizes, we can conclude that DPPC-cholesterol interactions stabilize cholesterol domains and inhibit their growth.
The crystals grown from Chol/POPC are intensely labelled, while plate crystals in Chol/DPPC/POPC bilayers were detected as 'black regions'. This observation can indicate that crystals in

Chol/DPPC/POPC tend to grow along the bilayer plane as opposed to crystals in Chol/POPC bilayers that grow out of the bilayer allowing easier access of the antibody to the side faces.
In the presence of DPPC, some of the crystals grow in morphologies that are typical of the monoclinic cholesterol monohydrate polymorph
SM is considered the sphingolipid analog of saturated phosphatidylcholines like DPPC. Nevertheless, in contrast to DPPC mixtures, cholesterol crystallization from Chol/SM/POPC did not induce elongated or fiber crystals, but rather favored the formation of crystal plates at specific labeled regions. These labelled areas often display inner patterns of sharp lines that do not necessarily overlay with visible 3D crystals.
Interpretation of these labelled structures is challenging, due to the non-negligible labelling of SM by mAb 58B1. We believe that the sites of crystal growth colocalize with the SM-rich phases, while the large non-labelled areas are probably composed of POPC disordered pools.
From the collected data, we conclude that cholesterol crystallizes from ordered areas of SM or DPPC. In these regions, cholesterol crystallization is influenced by the tendency of DPPC or SM to segregate out of POPC, and their tendency to mix with cholesterol.
This study reflects the significance of lipid composition over crystal deposition mechanisms and identifies the possible different factors affecting cholesterol dissolution.

Bibliography

1. Alberts, B., Johnson, A., Lewis, J., Raff, M., Roberts, K. and Walter, P. *Molecular biology of the cell. 4th edn. Annals of Botany* **91,** (Oxford University Press, 2003).
2. Simons, K. & Van Meer, G. Lipid sorting in epithelial cells. *Biochemistry* **27,** 6197–6202 (1988).
3. van Meer, G., Voelker, D. R. & Feigenson, G. W. Membrane lipids: where they are and how they behave. *Nat. Rev. Mol. Cell Biol.* **9,** 112 (2008).
4. McMullen, T. P. W., Lewis, R. N. A. H. & McElhaney, R. N. Cholesterol–phospholipid interactions, the liquid-ordered phase and lipid rafts in model and biological membranes. *Curr. Opin. Colloid Interface Sci.* **8,** 459–468 (2004).
5. Crook, M. *Clinical Chemistry and Metabolic Medicine, 8th ed*.
6. Kruth, H. S. Macrophage foam cells and atherosclerosis. *Front. Biosci.* **6,** (2001).
7. Small, D. M.; Bond, M. G.; Waugh, D.; Prack, M. . S. Regression of Atherosclerosis-An Ounce of Prevention. *J Clin Invest* **73,** 1590 (1984).
8. Konikoff, F. M., Chung, D. S., Donovan, J. M., Small, D. M. & Carey, M. C. Filamentous, helical, and tubular microstructures during cholesterol crystallization from bile: Evidence that cholesterol does not nucleate classic monohydrate plates. *J. Clin. Invest.* **90,** 1155–1160 (1992).
9. Ziblat, R., Leiserowitz, L. & Addadi, L. Crystalline lipid domains: Characterization by X-ray diffraction and their relation to biology. *Angew. Chemie - Int. Ed.* **50,** 3620–3629 (2011).
10. Ziblat, R., Kjaer, K., Leiserowitz, L. & Addadi, L. Structure of cholesterol/lipid ordered domains in monolayers and single hydrated bilayers. *Angew. Chem. Int. Ed. Engl.* **48,** 8958–8961 (2009).
11. Ziblat, R., Leiserowitz, L. & Addadi, L. Crystalline Domain Structure and Cholesterol Crystal Nucleation in Single Hydrated DPPC:Cholesterol:POPC Bilayers. *J. Am. Chem. Soc.* **132,** 9920–9927 (2010).
12. Lafont, S. *et al.* Monitoring the nucleation of crystalline films of cholesterol on water and in the presence of phospholipid. *J. Phys. Chem. B* **102,** 761–765 (1998).
13. Varsano, N., Fargion, I., Wolf, S. G., Leiserowitz, L. & Addadi, L. Formation of 3D Cholesterol Crystals from 2D Nucleation Sites in Lipid Bilayer Membranes: Implications for Atherosclerosis. *J. Am. Chem. Soc.* **137,** 1601–1607 (2015).
14. Ziblat, R., Fargion, I., Leiserowitz, L. & Addadi, L. Spontaneous Formation of Two-Dimensional and Three-Dimensional Cholesterol Crystals in Single Hydrated Lipid Bilayers. *Biophys. J.* **103,** 255–264 (2012).
15. Wong, J. Y. *et al.* Polymer-cushioned bilayers. I. A structural study of various preparation methods using neutron reflectometry. *Biophys. J.* **77,** 1445–1457 (1999).
16. Aimee, E. C., Haynes, M. P., Phillips, M. C. & George, H. Use of cy s for cholesterol content. *J. Lipid Res.* **38,** 2264–2272 (1997).